

556046
3172813
TR diss 2009

Stellingen ontbreken

**TR diss
2089**

**Downward extrapolation
of
multi-component seismic data**

**Downward extrapolation
of
multi-component seismic data**

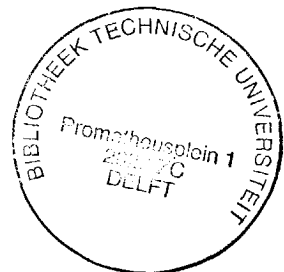
PROEFSCHRIFT

ter verkrijging van de graad van doctor
aan de Technische Universiteit Delft,
op gezag van de Rector Magnificus,
prof. drs. P.A. Schenck,
in het openbaar te verdedigen
ten overstaan van een commissie,
aangewezen door het College van Dekanen
op dinsdag 1 september 1992 te 10.00 uur door

GREGORY CARLO HAIMÉ

geboren te Paramaribo, Suriname

natuurkundig ingenieur



Dit proefschrift is goedgekeurd door de promotor:

prof. dr. ir. A.J. Berkhout

Toegevoegd promotor:

dr. ir. C.P.A. Wapenaar

Copyright ©1992, by Delft University of Technology, Delft, The Netherlands.

All rights reserved. No part of this publication may be reproduced, stored in a retrieval system or transmitted in any form or by any means, electronic, mechanical, photocopying, recording or otherwise, without the prior written permission of the author G.C. Haimé, Delft University of Technology, Faculty of Applied Physics P.O. Box 5046, 2600 GA Delft, The Netherlands.

CIP-GEGEVENS KONINKLIJKE BIBLIOTHEEK, DEN HAAG

Haimé, Gregory Carlo

Downward extrapolation of multi-component seismic data

Gregory Carlo Haimé - [S.l. : s.n.] (Zoetermeer: Gebotekst)

Thesis Technical University Delft. - With ref.

ISBN 90-9005213-5

Subject headings: elastic wave field extrapolation / redatuming / migration.

SUPPORT

The research for this thesis has been financially supported by the DELPHI consortium.

Typesetting and graphing system: Apple Macintosh with FrameMaker® and WaveMetrics Igor

Printed in The Netherlands by: N.K.B. Offset bv, Bleiswijk.

Aan mijn moeder

Aan Indra

Table of contents

Notation and definitions v

1 Introduction 1

2 Elastic processing 5

2.1 Multi-component Elastic data 5

2.2 Seismic inversion in three steps 11

2.2.1 Decomposition of the data and multiple elimination (surface) 14

2.2.2 Macro model estimation followed by redatuming and migration
(overburden) 16

2.2.3 Lithostratigraphic inversion (target) 21

3 Elastic extrapolation operators 23

3.1 Reciprocity 24

3.1.1 Elastic Kirchhoff-Helmholtz integral relations	27
3.1.2 Green's function due to an impulsive P wave source	30
3.1.3 Green's function due to an impulsive S wave source	33
3.1.4 Reciprocity relations for Green's wave fields	34
3.1.5 Modified Kirchhoff-Helmholtz integral	36
3.2 Modified Rayleigh integrals	39
3.2.1 Forward extrapolation operator for P waves	50
3.2.2 Forward extrapolation operator for S waves	51
3.2.3 Extrapolation operators for primary up- and downgoing waves	52
3.2.4 Summary	54
3.3 Backward propagating Green's functions	54
3.3.1 Kirchhoff-Helmholtz integral with backward propagating Green's functions	54
3.3.2 Rayleigh-integrals with backward propagating Green's functions	57
3.3.3 Inverse extrapolation operator for primary P waves	61
3.3.4 Inverse extrapolation operator for primary S waves	62
3.3.5 Summary	62
 4 Amplitude analysis	 65
4.1 Error analysis	66
4.2 Influence of macro model errors	81
4.2.1 Sensitivity	85
4.2.2 Decomposition; before or after extrapolation ?	88
4.3 Concluding remarks	92
 5 Modified Rayleigh operators in redatuming and migration	 95
5.1 Elastic redatuming and migration	95
5.1.1 Principles	95
5.1.2 Imaging condition	113
5.2 Conclusions	116
 Appendix A Elastic Rayleigh integral contributions	 119
 Appendix B Implementation aspects of seismic modeling	 129
B.1 Introduction	129
B.2 Theory	130
B.3 P and SV buried sources	137

B.4 Stress-sources at a free surface	145
B.5 Absorbing boundaries; Clayton and Engquist (1977)	147
B.6 Staggered grid	148
B.7 Absorbing boundary conditions; Randall (1988,1989)	150
B.8 Conclusions	153

References	157
------------	-----

Summary	163
---------	-----

Samenvatting	165
--------------	-----

Chapter Table of contents

Notation and definitions

Throughout this thesis scalar quantities will be denoted by italic symbols (e.g. α , c_p). Vectors will be bold face (e.g. \mathbf{u} , Ψ). Matrices (and tensors) will be bold face with a tilde \sim underneath (e.g. $\underline{\mathbf{s}}$, $\underline{\mathbf{W}}$). Time-space domain quantities will always be presented in lower-case, while frequency-space domain quantities will be presented in upper-case. Frequency-wavenumber domain quantities are presented by uppercase symbols with a tilde \sim above (e.g. $\tilde{\Phi}$, $\tilde{\Psi}$).

In this thesis use will be made of the Einstein's summation convention for repeated indices. Repeated indices imply a summation from 1 to 3. Thus, for

$$\tau_{ij} - \sum_{k=1}^3 \sum_{l=1}^3 c_{ijkl} \partial_l u_k = 0 \quad (0.1)$$

the following is written

$$\tau_{ij} - c_{ijkl} \partial_l u_k = 0 \quad (0.2)$$

where i (or j, k, l) = 1, 2, 3 stand for x, y, z , respectively. The summation convention does not apply to repeated indices x, y or z .

The temporal Fourier transformation used in this thesis is defined as

$$H(x, y, z, \omega) = \int_{-\infty}^{+\infty} h(x, y, z, t) e^{-i\omega t} dt \quad (0.3)$$

and the inverse as

$$h(x, y, z, t) = \frac{1}{2\pi} \int_{-\infty}^{+\infty} H(x, y, z, \omega) e^{+i\omega t} d\omega. \quad (0.4)$$

Throughout this thesis it is assumed that $h(x, y, z, t)$ is a real function, so that

$$H(x, y, z, -\omega) = H^*(x, y, z, \omega), \quad (0.5)$$

where the asterisks $*$ denotes complex conjugation. With this assumption the inverse Fourier transform may also be written as

$$h(x, y, z, t) = \frac{1}{\pi} \operatorname{Re} \left[\int_0^{+\infty} H(x, y, z, \omega) e^{+i\omega t} d\omega \right]. \quad (0.6)$$

Hence, in this thesis only positive ω will be considered. The double spatial Fourier transform of $H(x, y, z, \omega)$ is defined as

$$\tilde{H}(k_x, k_y, z, \omega) = \int_{-\infty}^{+\infty} \int H(x, y, z, \omega) e^{+i(k_x x + k_y y)} dx dy \quad (0.7)$$

and the inverse as

$$H(x, y, z, \omega) = \frac{1}{4\pi^2} \int_{-\infty}^{+\infty} \int \tilde{H}(k_x, k_y, z, \omega) e^{-i(k_x x + k_y y)} dk_x dk_y. \quad (0.8)$$

Introduction

One of the simplifying assumptions in the industrial approach to seismic processing is that the wave fields contain only compressional waves and the presence of shear waves is regarded as noise. The last few years an increasing amount of effort is spent on the problem how to treat seismic wave fields in an *elastic* way. Thus, shear waves are no longer seen as noisy components but as events that contain relevant information about the subsurface. In addition, amplitude effects such as transmission losses are treated more satisfactory. The amplitude behavior of seismic data contains essential information on the elastic parameters of the subsurface layers.

Going from seismic measurements to elastic parameters is generally referred to as *inversion*. Tarantola (1987) argues that, if there was no limitation on computer power, seismic inversion should be carried out by means of a global non-linear inversion algorithm, where all elastic parameters are estimated simultaneously. At the other end, Berkhout (1982,1989) and Berkhout and

Wapenaar (1990) argue that the parameters should be divided into three groups: surface parameters, overburden parameters (macro) and target parameters (detail). By stepwise inversion the parameters of each group can be estimated in a controlled way, irrespective to the available computer power. The nucleus in stepwise inversion is *seismic migration*.

Migration techniques depend largely on the quality of the wave field extrapolation operators involved. In most migration schemes these operators are based on the acoustic assumption. Economic acoustic operators are acceptable if the only concern is to obtain structural information. To go beyond structural information, i.e. toward elastic parameters and rock characterization, it is necessary to make use of elastic extrapolation operators. Even for the processing of marine data it is necessary to use *elastic* operators in order to take into account the full elastic propagation properties of the medium below the seabed. Kuo and Dai (1984) use the elastic Kirchhoff-Helmholtz integral in terms of stresses and displacements as the starting point for elastic wave migration. As a consequence, P and S waves are handled simultaneously in their scheme. In this thesis we follow a different approach, based on decomposition of the elastic wave field into up- and downgoing P and S components, prior to migration. Decomposition has been studied for *modeling* purposes by many authors: Aki and Richards (1980), Kennett (1983), van der Hijden (1987), de Hoop (1992). For an extensive overview on this subject the reader is referred to Ursin (1983). Decomposition of multi-component measurements into up- and downgoing P - and S -components for *inversion* purposes has obtained much less attention; Devaney and Oristaglio (1986) and Dankbaar (1987) for VSP measurements; Dankbaar (1985), Wapenaar et al. (1990), Berkhout and Wapenaar (1990) and Herrmann (1992) for seismic surface measurements. Wapenaar and Haimé (1990) derived elastic extrapolation operators for decomposed surface measurements. By decomposing the elastic Green's function as well, the decomposed P and S data can be extrapolated separately, making the extrapolation process insensitive for inconsistencies between P and S macro velocity models.

The main objective of this thesis is to present an evaluation of the problems involved in *elastic* seismic migration. Elastic wave field extrapolation operators

are presented that are applicable to a general 3D elastic and anisotropic medium. Although the elastic operators derived in this thesis are stand alone elements and can be used in any migration scheme, they are developed to take part in the stepwise elastic inversion scheme proposed by Berkhout and Wapenaar (1990).

In Chapter 2 the advantages of multi-component seismic acquisition are discussed. In the first part the necessity of multi-component data in elastic processing is demonstrated by an example. In the second part a global description of all modules in the stepwise elastic inversion scheme is given. In Chapter 3 elastic P and S extrapolation operators are derived starting from the full elastic Kirchhoff-Helmholtz integral. Chapter 3 forms the heart of this thesis. An analysis of the contribution of the different elastic terms in the extrapolation process is presented. Also, it will be made clear in this chapter that there are many different ways to *generate* extrapolation operators for a so called macro model. (Such a macro model represents a global description of the subsurface in terms of velocities and densities and must be estimated before the actual extrapolation step can be carried out.) In Chapter 4 a quantitative error analysis of the extrapolation operators proposed in Chapter 3 is carried out. Also, the influence of macro model errors on the amplitudes of the extrapolated P and S wave fields is examined. The final chapter deals with the use of the elastic P and S extrapolation operators in redatuming and migration schemes.

Elastic processing

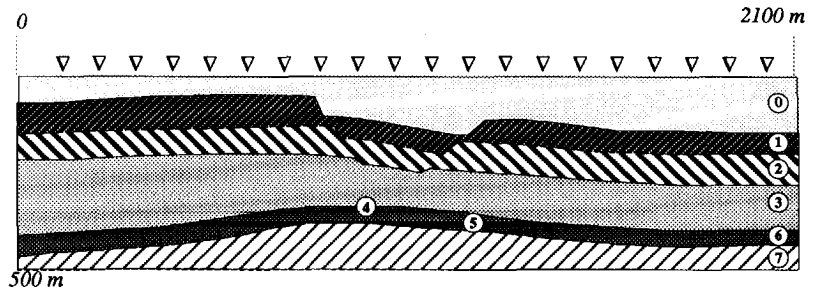
To obtain maximum information out of seismic reflection measurements it is necessary to do multi-component acquisition. Most often in seismic practice only one-component data is recorded. This imposes an important constraint to the main objective of seismic exploration which is to create an accurate and detailed image of the subsurface. Therefore it is not surprising that in the last few years there is a tendency to do more multi-component seismic acquisition on land. In the next section it will be illustrated by an example what can ultimately be accomplished by elastic processing of full multi-component data.

2.1 Multi-component Elastic data

Consider the following seismic experiment where an elastic 2D subsurface model is situated in the x - z plane (Fig. 2.1), where the horizontal x -axis points to the right and the vertical z -axis points downward. For practical reasons all the examples in this thesis will be 2D examples, but the theory throughout the

thesis applies to general 3D situations. The model consists of a three layered Graben-structure overlying a reservoir. A vertical stress-source (τ_{zz}) is placed on top of the free surface (note that the source is actually a line source perpendicular to the paper and the model is just a cross section). A receiver array is positioned on top of the free surface ranging from $x=24$ m to $x=2064$ m as illustrated in Fig. 2.1 by the triangles. The distance between two receivers is 8 m. The receiver line carries in total 256 receivers. The number of sources amounts to 81, ranging from $x=472$ m to $x=1752$ m with a separation distance of 16 m. Fig. 2.2 shows three snapshots of the horizontal and vertical displacement of the wave field due to a τ_{zz} source positioned at $(x,z)=(1112,0)$ (source#41). In the snapshots several phenomena can be observed. The wave field emitted by the τ_{zz} source contains both P and S waves. A head wave connects the emitted S

Fig. 2.1
Graben-structure
(overburden; layers
0,1,2 and 3) overlying
a hydrocarbon
reservoir (target;
layers 4,5 and 6)



layer	c_p	c_s	ρ
0	2200	1400	2000
1	2800	1600	2100
2	3300	1800	2400
3	3100	1700	2300
4	2300	1400	2150
5	2550	1350	2300
6	2750	1400	2350
7	3600	2100	2450

wave with the horizontally propagating P wave. A Rayleigh wave can be observed as the strong surface event moving to the left and right away from the source. The emitted wave field is scattered by the reflectors in the subsurface. The scattered wave field is detected by the receiver array and constitutes the elastic reflection response of the source in that medium. The data recorded by the receiver array are shown in Fig. 2.3. The two data sets correspond to the horizontal and vertical displacement respectively. In both these data sets P and S events are mixed. The first event \textcircled{D} corresponds to the direct wave field emitted by the source and travels with the compressional wave velocity along the receiver line. The strongly dipping event \textcircled{R} is the Rayleigh wave, often referred to as “ground roll”. This low velocity surface event may be removed from the data by applying a velocity filter in the wavenumber domain. In practice, however, this is not easily done and one has to use other tools to get rid of the Rayleigh wave. The way to remove the Rayleigh wave in the data will not

Fig. 2.2
Three successive snapshots in terms of the horizontal and vertical displacement (at times 50 ms, 200 ms and 400 ms) of the wave field travelling through the elastic medium due to a τ_{zz} source at the free surface.

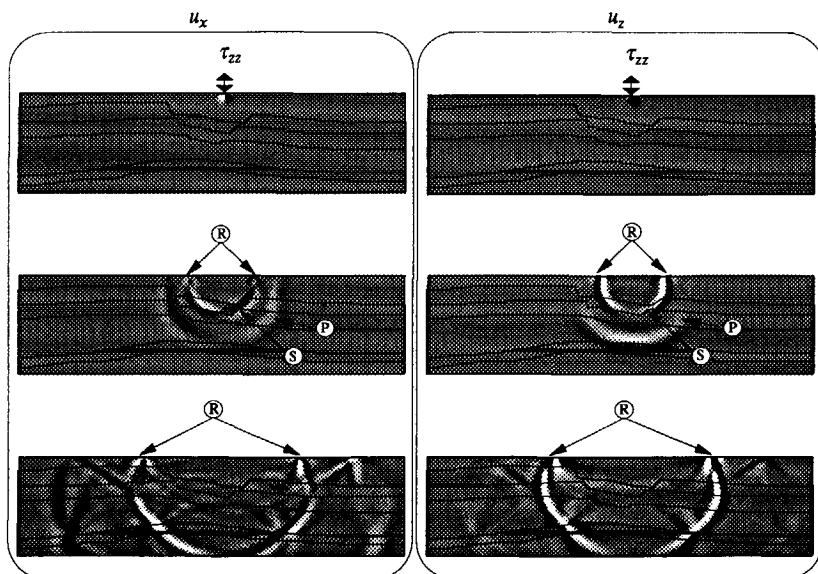
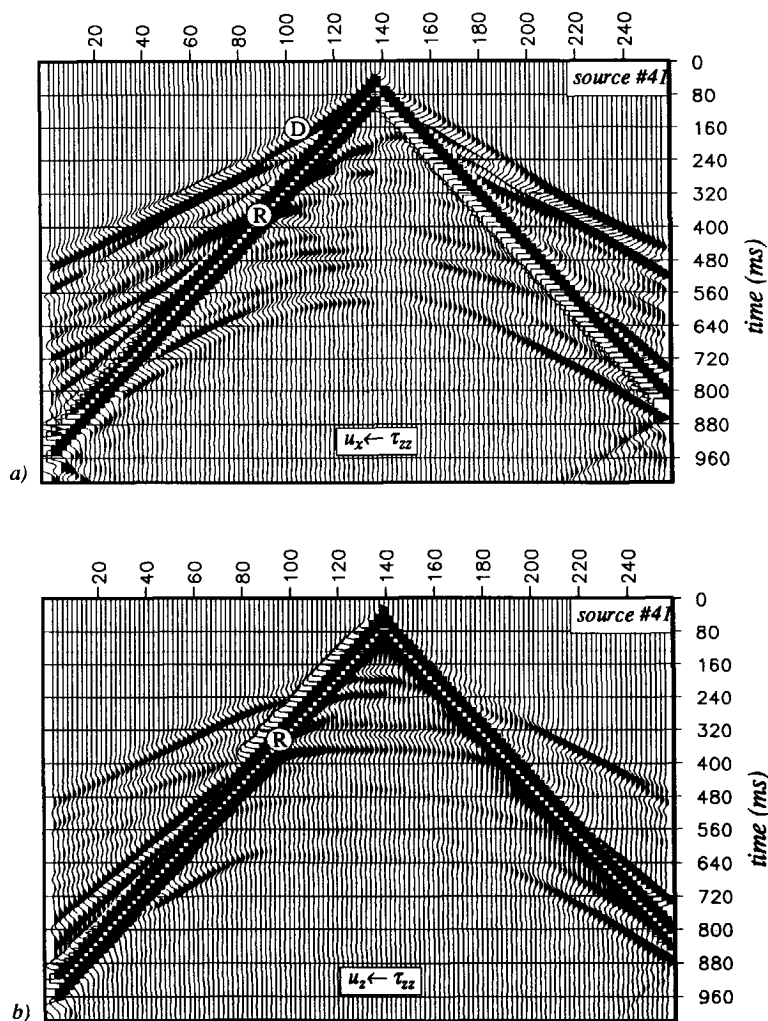


Fig. 2.3

a) and b) Recorded elastic data in terms of the horizontal and vertical displacement due to a τ_{zz} source. (D) and (R) indicate the direct wave and the Rayleigh wave respectively.



be considered anymore in this thesis. The reader is referred to Saatcilar, R., and Canitez, N., 1988; Beresford-Smith, G., and Rango, R., 1989; Morse, P. F., and Hildebrandt, G. F., 1989; McMechan and Sun, 1991. In seismic practise when collecting land data with a vibroseis technique it is common to use a τ_{zz} source and record only the vertical component.

The data in Fig. 2.3 represent the recordings of the *total* wave field at the free surface (up- and downgoing P and S waves). The upgoing waves in these data are the primary responses of the reflectors followed by multiples. The upgoing wave field is scattered downward when it hits the free surface. This scattered wave field constitutes the downgoing part in the data.

To decompose the data at the source side uniquely into downgoing P and S waves a second multi-component data set is necessary and that is data due to a

Fig. 2.4
Three successive snapshots (at times 50 ms, 200 ms and 400 ms) of the propagating wave field due to a τ_{zz} source at the free surface.

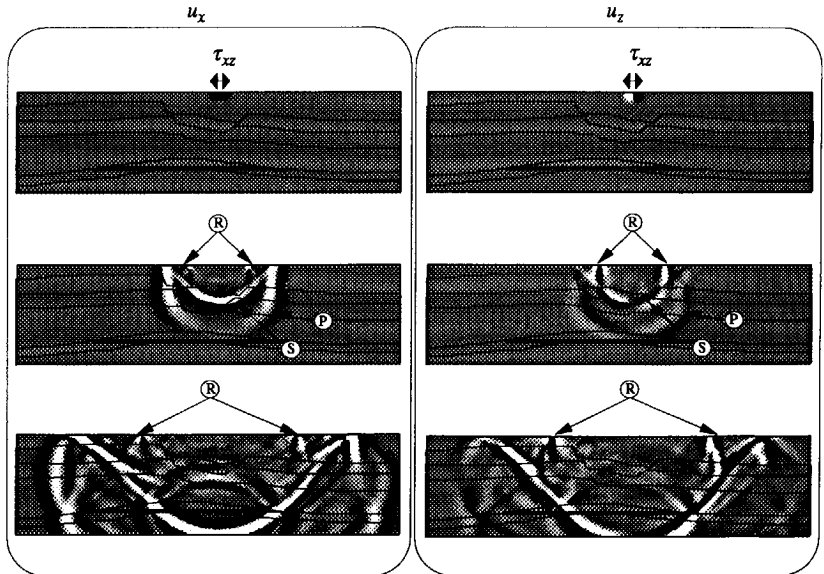
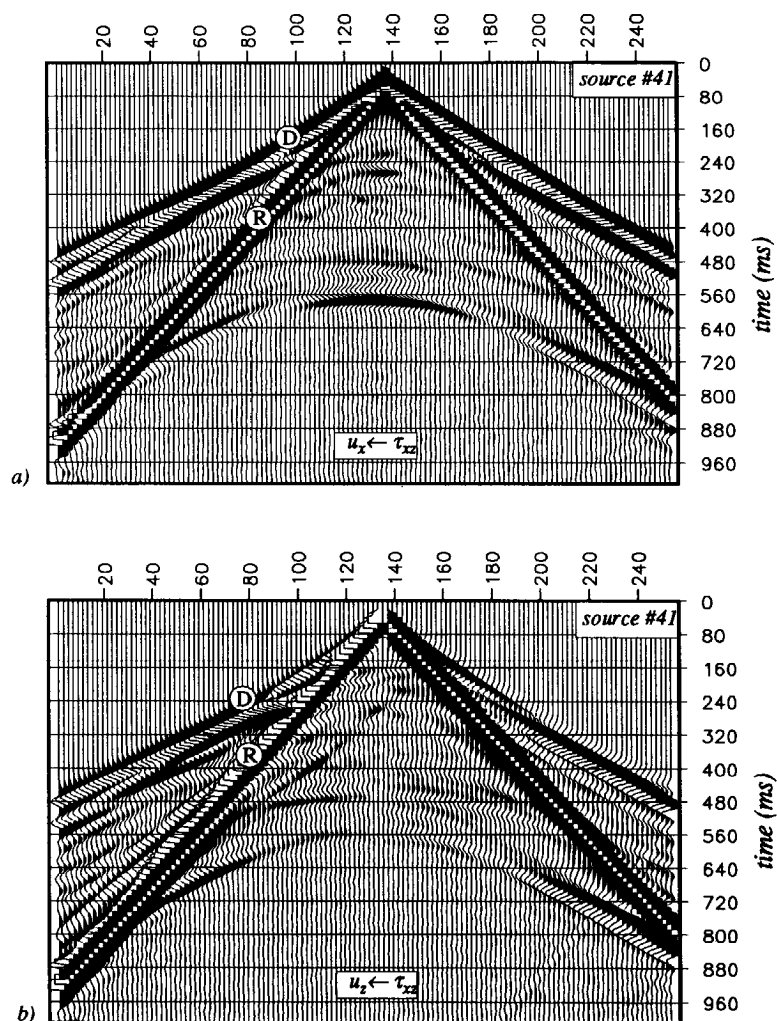


Fig. 2.5

a) and b) Elastic reflection data in terms of the horizontal and vertical displacement respectively due to a τ_{xz} source.

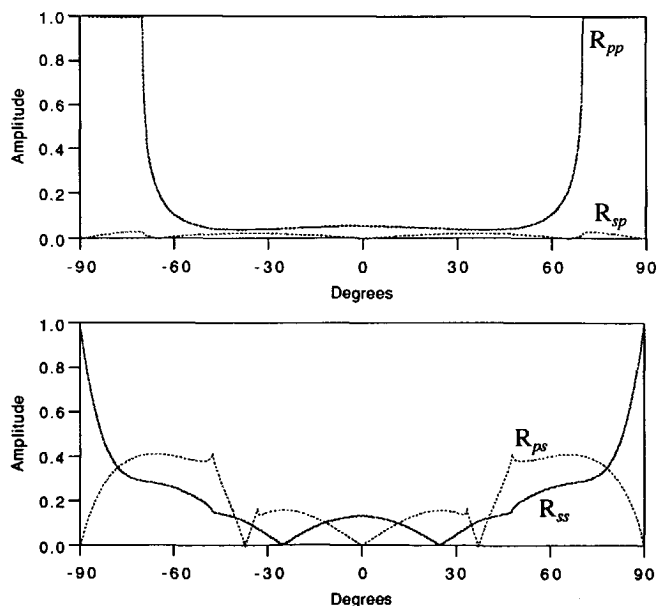


τ_{xz} source. Snapshots of the wave field due to a τ_{xz} source at $(x,z)=(1112,0)$ are shown in Fig. 2.4. The data in terms of the horizontal and vertical displacement are shown in Fig. 2.5. In the next section it will be illustrated step by step how the multi-component elastic data (Fig. 2.3 and Fig. 2.5) are processed according to an elastic processing scheme proposed by Berkhout and Wapenaar, 1988. The objective is to extract the maximum on information from the elastic data, thereby utilizing traveltime as well as amplitude information and taking into account all the elastic characteristics in the data. Angle dependent reflection behavior is expressed in the seismic amplitudes and therefore one has to be careful not to destroy this information when inverse extrapolating the recorded events toward the reflectors. Typical angle dependent reflection functions PP , SP , SS and PS are shown in Fig. 2.6.

Fig. 2.6

Typical elastic angle dependent reflection functions.

(These curves are derived for a horizontal reflector between two homogeneous half spaces with the parameters of layers 4 and 5 in the Graben model of Fig. 2.1.)



To go any deeper into the Earth a macro model is needed describing the propagation properties of the subsurface, irrespective the kind of extrapolation technique one uses. Macro model estimation is a crucial step when it comes to true amplitude redatuming and migration. The significance of highly sophisticated wave field extrapolators can only be appreciated when a “good” macro model is used as a basis. Treating the data in an elastic way means that a P macro model and an S macro model have to be estimated. In practise these two macro models will generally not be fully consistent. Later on in the thesis a careful analysis will show that, as a consequence of this inconsistency, it is better to extrapolate the P and S data by two separate procedures, meaning that one should do the decomposition into P and S waves *before* extrapolation.

2.2 Seismic inversion in three steps

Forward model of seismic data

The physics of a seismic reflection experiment can be described as follows:

source excitation →
downward propagation of the source wave field →
→ reflection at interfaces →
upward propagation of the reflected wave fields →
detection by receivers →
reflection by the free surface →
downward propagation of the reflected wave field

Dividing the seismic inversion into three main steps is probably the most natural way to go (Berkhout, 1989, Berkhout and Wapenaar, 1990). These steps are (see also Fig. 2.7)

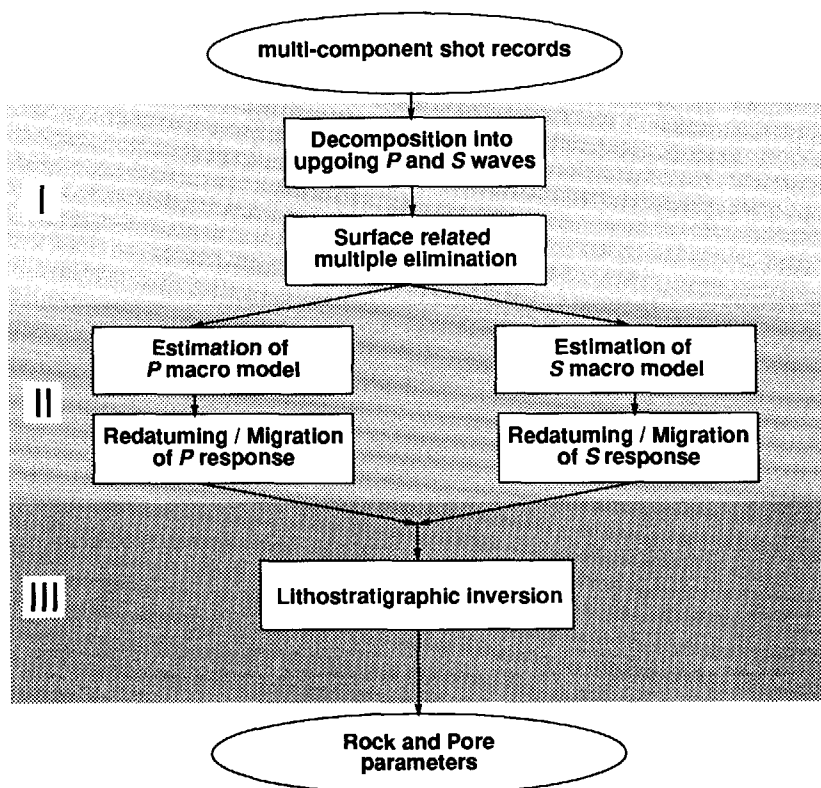
- 1) surface related preprocessing (surface),
- 2) wave field extrapolation (overburden),

3) lithostratigraphic inversion (target).

The main idea behind the first step is to unravel the elastic data at the surface as far as possible without any loss of information before going any deeper. The second step takes care of the effects of propagation on the incident wave field and the reflected wave fields due to propagation through the overburden. From the corrected incident and reflected wave fields at the target the angle depen-

Fig. 2.7

Elastic processing scheme divided into three major categories.
 I. surface related pre-processing
 II. wave field extrapolation
 III. lithostratigraphic inversion.



dent reflection functions can be retrieved by generalized imaging. These functions contain crucial information about the elastic and lithologic parameters of the system, which are retrieved in the third step.

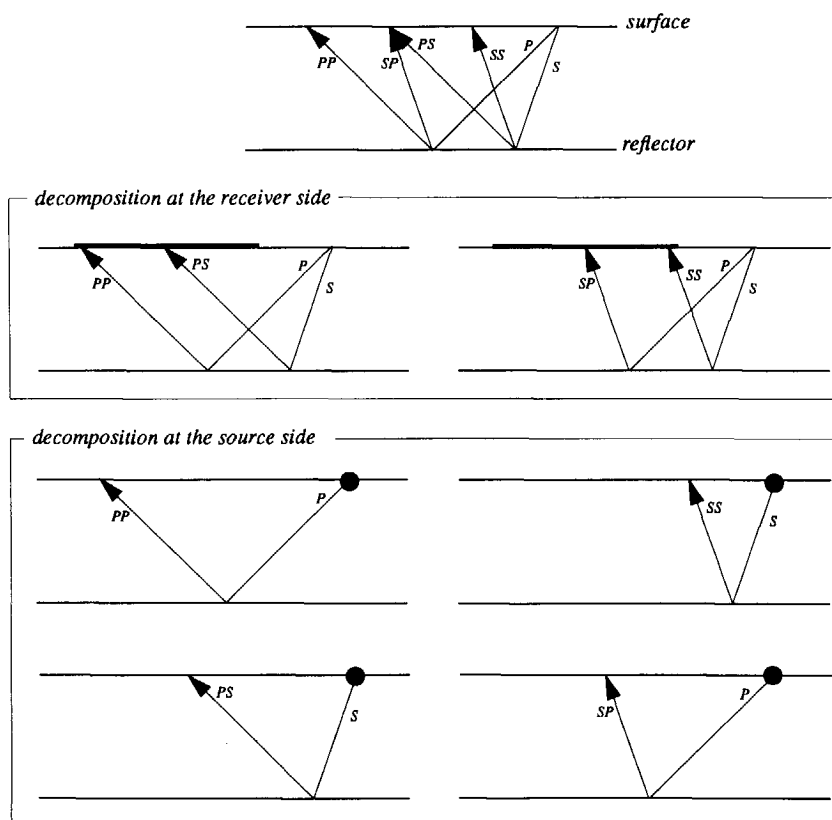
The material discussed in Chapter 3 is a part of the second step. It is assumed that the first preprocessing step has been carried out already. In the following sections a global overview is given of the different steps in the elastic processing scheme. From this it will be clear where the extrapolation operators discussed in Chapter 3 fit into this scheme.

2.2.1 Decomposition of the data and multiple elimination (surface)

When a multi-component seismic survey is carried out a total decomposition of the recorded data can be achieved. This means decomposition of the recorded data into upgoing P and S wave fields at the *receiver side* and decomposition of the source wave field into downgoing P and S waves at the *source side* (see Fig. 2.8). (It would go beyond the scope of this thesis to go any deeper into the process of the wave field decomposition. The reader is referred to Dankbaar, 1985; Wapenaar et al., 1990; Herrmann, 1992. The following is confined to a global overview of the way decomposition can be performed.) At the end of the two decomposition steps four data sets are left, namely $P \leftarrow P$, $S \leftarrow P$, $P \leftarrow S$ and $S \leftarrow S$. It should be emphasized that the decomposition process is merely a reordering of the original data, hence, no information is lost during the process. The four data sets still constitute the full *elastic* response of the subsurface organized in a different but more convenient way. Notice that in Fig. 2.8 multiples are not pictured but they are fully included in the decomposition process. Obviously, multiples may interfere destructively with primary responses from interfaces situated deeper in the subsurface. Therefore, it is recommendable, when strong surface related multiples are present to apply a surface multiple elimination procedure, thus leaving only the *primary* responses (and internal multiples) of the different reflectors in the subsurface in the decomposed data. The multiple elimination procedure is a prestack wave equation based procedure (Kennett, 1979; Berkhout, 1982; Verschuur, 1991). Therefore one only needs to know the reflecting properties of the free surface where the acquisition is done and a

Fig. 2.8

Total decomposition of multi-component data in two steps; first separation into P and S waves at the receiver side followed by a separation at the source side.



source wavelet. No knowledge of the subsurface is needed. In fact, the data itself is used as an operator to predict the multiples. This is in contrast to other multiple elimination procedures (Berntsen and Sonneland, 1983; Berryhill and Kim, 1986) where accurate knowledge about the subsurface in the form of a macro model is necessary (at least for the first layers) to eliminate the multiples. The source wavelet needed for the first procedure is estimated during the

elimination procedure itself (adaptive multiple elimination). The theory is valid for acoustic as well as elastic data. In the elastic case, when taking into account the elastic reflection properties of the free surface, even the converted multiples can be eliminated.

After the decomposition and the surface related multiple elimination procedure there are four data sets left, namely $P \leftarrow P$, $S \leftarrow P$, $P \leftarrow S$ and $S \leftarrow S$. In these data sets mainly the *upgoing primary* responses of the reflectors in the subsurface are left due to either a P or an S source (there are still some internal multiple reflections present that are often very weak compared to the primary responses). The four decomposed data sets that correspond to the example from the previous section are displayed in Fig. 2.9.

2.2.2 Macro model estimation followed by redatuming and migration (overburden)

It is mainly from the $P \leftarrow P$ data and the $S \leftarrow S$ data from which a P macro model and an S macro model are estimated. The macro model estimation procedure is based on the coherency analysis of Common Depth Point gathers obtained by shot record redatuming (for more details on this subject see Cox, 1991).

Once the P and S macro models are estimated the P and S extrapolation operators can be calculated for use in redatuming and migration algorithms (Chapter 3). Errors in the macro models will affect the quality of these extrapolation operators and consequently also affect the migrated result. In Chapter 4 the influence of macro model errors on amplitudes is studied in more detail. The redatuming process brings the sources and the receivers to a level just above the area of interest (target area) in a non-recursive step. The (simulated) result for the Graben model is shown in Fig. 2.10 for the same lateral source position as the one in Fig. 2.9 but now at level $z=300$ m. Using the incident and reflected wave field as input, angle dependent reflection curves can be obtained by generalized imaging.

It should be emphasised that the results shown in Fig. 2.10 were simulated by forward modeling to show what can be ultimately obtained from multi-

Fig. 2.9
Decomposition of the elastic data into upgoing $P \leftarrow P$ (a), $S \leftarrow P$ (b), $S \leftarrow S$ (c) and $P \leftarrow S$ (d) data. P_o and P_t are the P wave responses from the overburden and the target respectively. S_o and S_t are the S wave responses from the overburden and the target respectively.

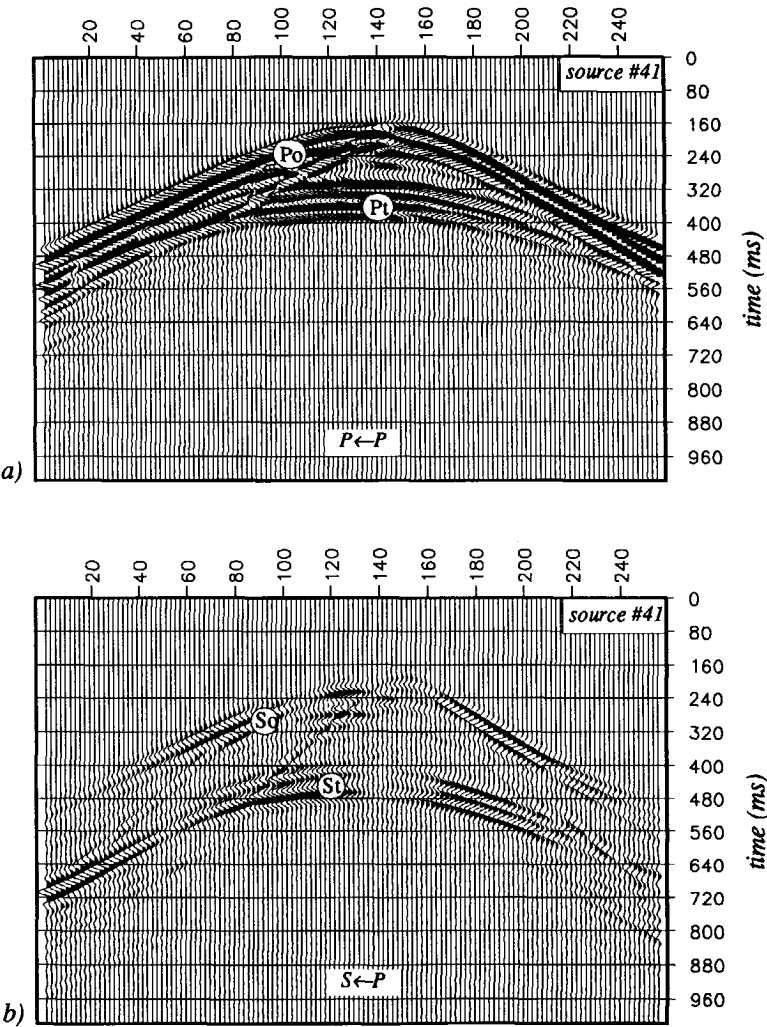


Fig. 2.9
(continued).

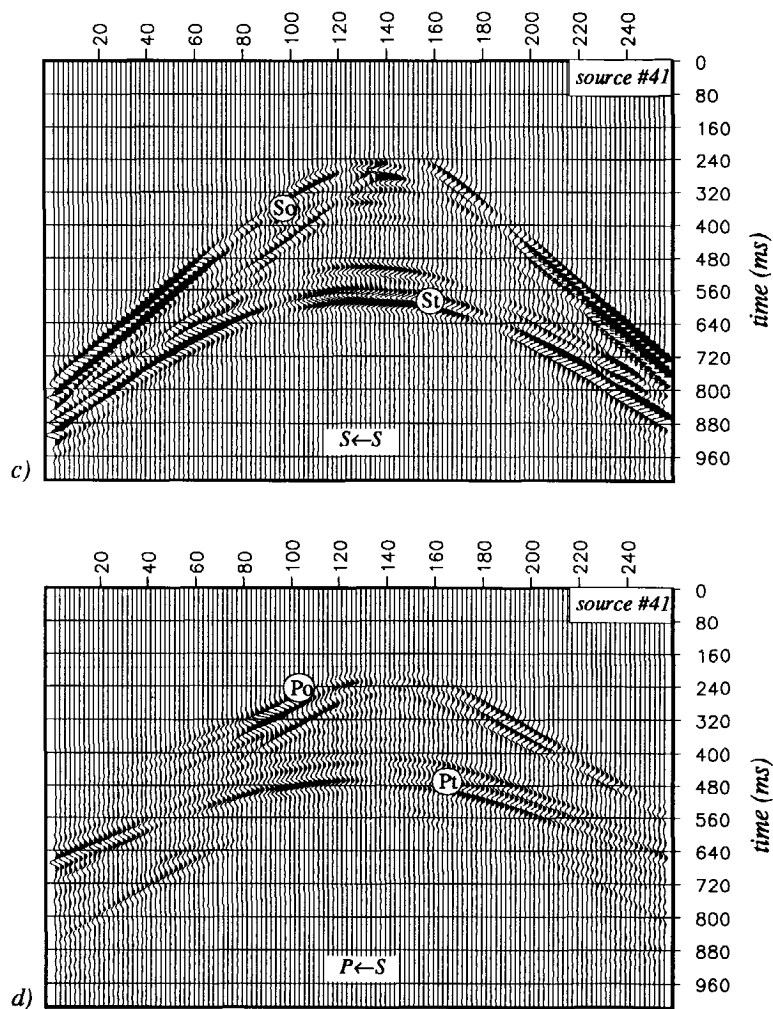


Fig. 2.10

a) - d) Simulated decomposed data. Source and receivers at $z=300$ m (redatuming level. The lateral source position corresponds to surface source #41).

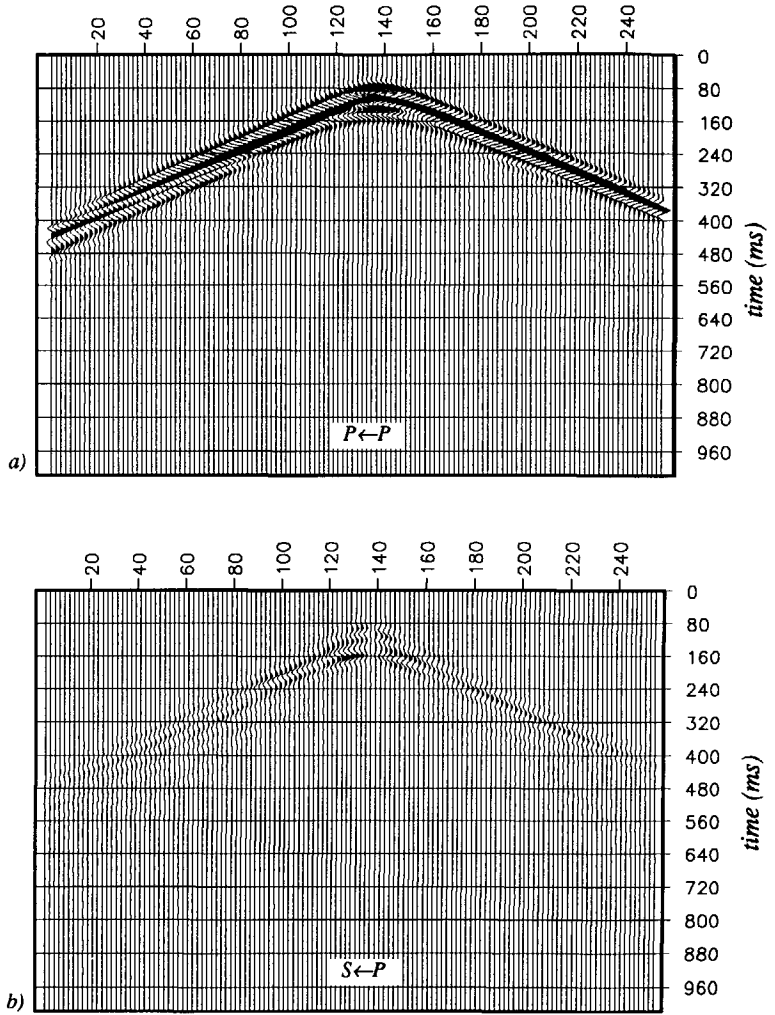
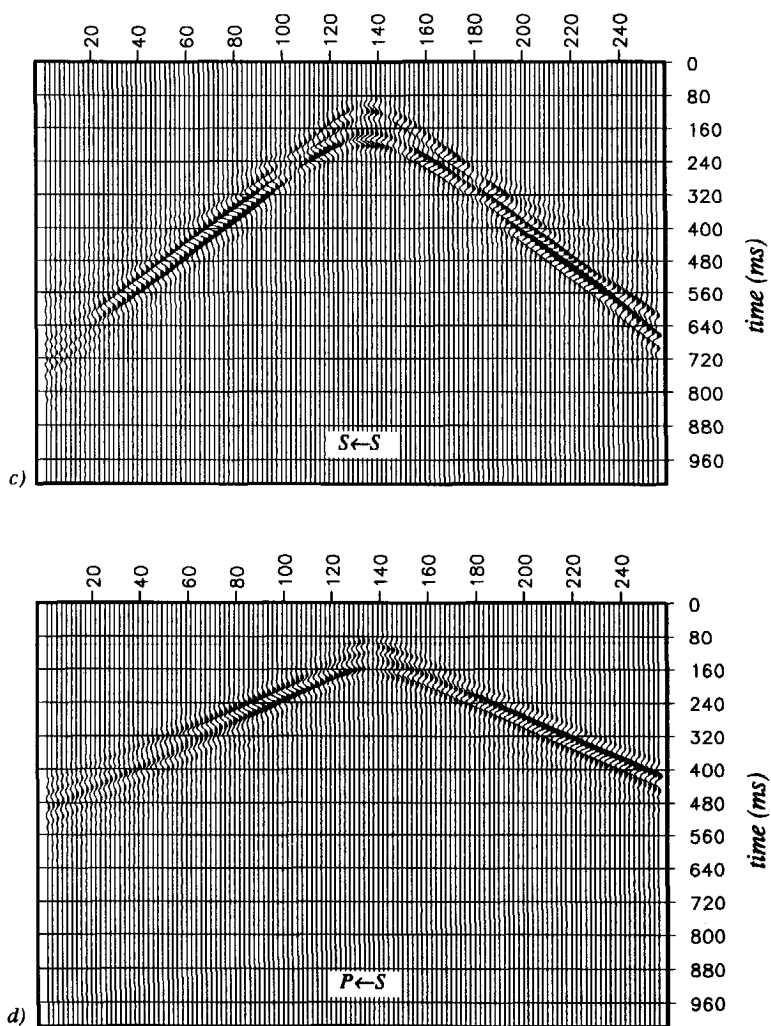


Fig. 2.10
(continued)



component seismic data. The data are shown for the full aperture ($x=24-2064$ m) at the redatuming level ($z=300$ m). In Chapter 5 the actual processing results will be shown and they will be compared with the results in Fig. 2.10.

2.2.3 Lithostratigraphic inversion (target)

As mentioned before the aim of the prestack migration process is to retrieve angle dependent reflection information for each point (depth point) on all the different reflectors in the target area. The angle dependent reflection information can then be used in a parametric inversion algorithm to produce more detailed estimates of the P and S wave velocities and the densities (de Haas, 1992) and/or the lithostratigraphic properties (Lörtzer, 1990; de Bruin, 1992).

Elastic extrapolation operators

The migration process can be described as the process that brings back a diffracted wave field recorded at the surface to the location that caused this diffraction. The mathematical tool that is used in this process is called the extrapolation operator. In a complicated medium as the earth advanced extrapolation operators are needed in order to back propagate the recorded wave field, thereby incorporating the inhomogeneous elastic effects of the overburden. In this Chapter elastic extrapolation operators are developed for separate forward and inverse extrapolation of primary P and S waves. The Kirchhoff-Helmholtz integral is modified such that it expresses either the P or S wave potential in a point in the medium in terms of a closed surface integral. From thereon Rayleigh-type integrals are derived that express the P and S potential in a point in the medium in terms of the P and S wave fields at a plane surface.

3.1 Reciprocity

In this section Betti's reciprocity theorem (Aki and Richards, 1980; de Hoop, 1990) is presented in the space-frequency domain. From this theorem elastic Kirchhoff-Helmholtz integrals will be derived which form the basis of high quality elastic extrapolation operators as will be discussed in sections 3.2 and 3.3.

We consider an inhomogeneous anisotropic lossless solid medium. Outside some sphere of finite radius the medium is assumed to be homogeneous and isotropic. Let $\mathbf{u}^A(\mathbf{r}, t)$ and $\boldsymbol{\tau}^A(\mathbf{r}, t)$ be the displacements and stresses associated to an elastic wave field due to an external force density $\mathbf{f}^A(\mathbf{r}, t)$. Then, the components of displacement vector $\mathbf{u}^A(\mathbf{r}, t)$ and stress-tensor $\boldsymbol{\tau}^A(\mathbf{r}, t)$ satisfy the following set of equations

$$\partial_j \tau_{ij}^A - \rho^A \partial_t^2 u_i^A = -f_i^A \quad (3.1)$$

and

$$\tau_{ij}^A - c_{ijkl}^A \partial_l u_k^A = 0 \quad (3.2)$$

where c_{ijkl}^A are the components of a fourth-order stiffness tensor $\boldsymbol{\zeta}^A(\mathbf{r})$ and $\rho^A(\mathbf{r})$ is the mass density. This situation shall be referred to as state A .

Let $\mathbf{u}^B(\mathbf{r}, t)$ and $\boldsymbol{\tau}^B(\mathbf{r}, t)$ be another independent elastic wave field due to $\mathbf{f}^B(\mathbf{r}, t)$. The components of displacement vector $\mathbf{u}^B(\mathbf{r}, t)$ and stress-tensor $\boldsymbol{\tau}^B(\mathbf{r}, t)$ satisfy

$$\partial_j \tau_{ij}^B - \rho^B \partial_t^2 u_i^B = -f_i^B \quad (3.3)$$

and

$$\tau_{ij}^B - c_{ijkl}^B \partial_l u_k^B = 0 \quad (3.4)$$

where c_{ijkl}^B are the components of a fourth-order stiffness tensor $\underline{c}^B(\mathbf{r})$ and $\rho^B(\mathbf{r})$ is the mass density. This situation shall be referred to as state B .

Across interfaces between different kinds of solids (which are assumed to be in rigid contact), u_i and $\tau_{ij} n_j$ are continuous in both states (n_j denotes the components of the normal vector at such an interface).

Applying a temporal Fourier transform to the two sets of the above equations yields

$$\partial_j T_{ij}^A + \rho^A \omega^2 U_i^A = -F_i^A \quad (3.5)$$

and

$$T_{ij}^A - c_{ijkl}^A \partial_l U_k^A = 0 \quad (3.6)$$

for state A and

$$\partial_j T_{ij}^B + \rho^B \omega^2 U_i^B = -F_i^B \quad (3.7)$$

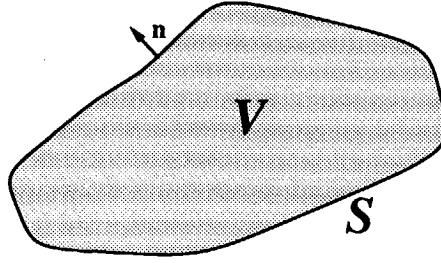
and

$$T_{ij}^B - c_{ijkl}^B \partial_l U_k^B = 0 \quad (3.8)$$

for state B , where U_i , T_{ij} and F_i (i.e., the components of \mathbf{U} , \mathbf{T} and \mathbf{F}) are the space-frequency domain representations of the space-time functions u_i , τ_{ij} and f_i respectively.

Fig. 3.1

Volume V with surface S and outward pointing normal vector \mathbf{n} .



We derive the reciprocity theorem that relates state A and B in some volume V in the solid medium. This volume is enclosed by surface S with outward pointing normal vector \mathbf{n} (components n_j), see Figure 3.1. In V , an interaction quantity Q_j may be defined according to

$$Q_j = T_{ij}^A U_i^B - T_{ij}^B U_i^A. \quad (3.9)$$

Applying the theorem of Gauss to (3.9) and using equations (3.5)-(3.8) yields the well known reciprocity theorem that is due to Betti,

$$\begin{aligned} \oint_S (T_{ij}^A U_i^B - T_{ij}^B U_i^A) n_j dS = \\ \iiint_V \left[(F_i^B U_i^A - F_i^A U_i^B) + (c_{klj}^A - c_{ijl}^B) \partial_l U_k^B \partial_j U_i^A \right. \\ \left. - \omega^2 (\rho^A - \rho^B) U_i^A U_i^B \right] dV \end{aligned} \quad (3.10)$$

where the contributions from interfaces have canceled in view of the above mentioned boundary conditions. Assuming that $c_{ijkl} = c_{klij}$ (meaning that the medium is 'reciprocal') (3.10) becomes

$$\begin{aligned} \iint_S (T_{ij}^A U_i^B - T_{ij}^B U_i^A) n_j dS = \\ \iiint_V \left[(F_i^B U_i^A - F_i^A U_i^B) + (c_{ijkl}^A - c_{ijkl}^B) \partial_l U_k^B \partial_j U_i^A \right. \\ \left. - \omega^2 (\rho^A - \rho^B) U_i^A U_i^B \right] dV. \end{aligned} \quad (3.11)$$

From here on it is assumed that in both states the medium parameters are identical, thus

$$c_{ijkl}^A = c_{ijkl}^B = c_{ijkl} \quad (3.12)$$

and

$$\rho^A = \rho^B = \rho, \quad (3.13)$$

hence, for this situation the last two terms in volume integral (3.11) are equal to zero, i.e.

$$\iint_S (T_{ij}^A U_i^B - T_{ij}^B U_i^A) n_j dS = \iiint_V (F_i^B U_i^A - F_i^A U_i^B) dV. \quad (3.14)$$

3.1.1 Elastic Kirchhoff-Helmholtz integral relations

A special form of the reciprocity theorem (3.14) can be obtained when for one wave field a Green's function is chosen and for the other the physical wave

field. A Green's function represents the impulse response of the medium. State A will be chosen to be the wave field related to a Green's function. Then, according to (3.5) and (3.6) the Green's displacement field and stress field satisfy

$$\partial_j \Theta_{ij,m} + \rho \omega^2 G_{i,m} = -\delta_{im} \delta(\mathbf{r} - \mathbf{r}_A) \quad (3.15)$$

and

$$\Theta_{ij,m} - c_{ijkl} \partial_l G_{k,m} = 0, \quad (3.16)$$

where the components of $\mathbf{T}^A(\mathbf{r}, \omega)$ and $\mathbf{U}^A(\mathbf{r}, \omega)$ have been replaced by the components of $\underline{\Theta}_m(\mathbf{r}, \mathbf{r}_A, \omega)$ and $\mathbf{G}_m(\mathbf{r}, \mathbf{r}_A, \omega)$ respectively. The extra parameter \mathbf{r}_A indicates the position of the Green's source and m denotes that this source is a force acting in the m -direction. In the time domain the Green's function will be denoted by $\underline{\Theta}_m(\mathbf{r}, \mathbf{r}_A, t)$ for the stress field and $\mathbf{g}_m(\mathbf{r}, \mathbf{r}_A, t)$ for the displacement field. The causality conditions for $\underline{\Theta}_m(\mathbf{r}, \mathbf{r}_A, t)$ and $\mathbf{g}_m(\mathbf{r}, \mathbf{r}_A, t)$ read

$$\underline{\Theta}_m(\mathbf{r}, \mathbf{r}_A, t) = \mathbf{0} \text{ for } t < 0 \quad (3.17)$$

and

$$\mathbf{g}_m(\mathbf{r}, \mathbf{r}_A, t) = \mathbf{0} \text{ for } t < 0. \quad (3.18)$$

Furthermore assume for state B that no external forces are present *inside* V , i.e.

$$F_i^B(\mathbf{r}, \omega) = 0 \quad (3.19)$$

inside V .

Superscript B used to indicate state B , related to the physical wave field, may now be dropped, i.e. in the following $\underline{\mathbf{T}}(\mathbf{r}, \omega)$ and $\mathbf{U}(\mathbf{r}, \omega)$ will be written instead of $\underline{\mathbf{T}}^B(\mathbf{r}, \omega)$ and $\mathbf{U}^B(\mathbf{r}, \omega)$. Using the symmetry property of the stress tensor, i.e.

$$T_{ij} = T_{ji} \quad (3.20)$$

and

$$\Theta_{ij,m} = \Theta_{ji,m} \quad (3.21)$$

then (3.9) can also be written as

$$\mathbf{Q}_m = \Theta_m \mathbf{U} - \underline{\mathbf{T}} \mathbf{G}_m. \quad (3.22)$$

With regard to these new notations and with (3.19) and (3.22) equation (3.14) becomes

$$U_m(\mathbf{r}_A, \omega) = - \oint_S \left(\Theta_m(\mathbf{r}, \mathbf{r}_A, \omega) \mathbf{U}(\mathbf{r}, \omega) - \underline{\mathbf{T}}(\mathbf{r}, \omega) \mathbf{G}_m(\mathbf{r}, \mathbf{r}_A, \omega) \right) \mathbf{n} dS. \quad (3.23)$$

This representation theorem states that the elastic wave field in any point inside a closed surface S can be represented in terms of a surface integral involving known quantities \mathbf{U} and $\underline{\mathbf{T}}$ on S (de Hoop, 1958; Burridge and Knopoff, 1964; Aki and Richards, 1980). Notice that in the derivation of (3.23) it is assumed that the medium parameters for both wave fields are identical ((3.12) and (3.13)). In practice, however, the medium in which the Green's function is

obtained, the so called reference medium, may differ from the true medium i.e. the physical medium. In that case the terms involving the medium parameters in the volume integral on the right hand side of (3.11) do not vanish. At this point it is important to realize that the physical medium can be thought as a superposition of a slowly varying (background) medium, describing mainly the propagation properties, and a rapidly varying (contrast) medium describing mainly the reflectivity properties of the physical medium. In the following (3.23) will be used as the basis for deriving extrapolation operators. Extrapolation operators are operators that aim to incorporate *propagation* effects during extrapolation. Therefore only a description of the background medium is necessary. Hence, if one is only interested in the *propagation* properties of the medium one can suffice by providing a reference medium that describes these propagation properties (later on in this thesis such a description of the background medium will be referred to as a 'macro model'). Hence, for the derivation of wave field extrapolation operators it is justified to say that if the reference medium does not differ too much from the physical medium, i.e. $c_{ijkl}^A - c_{ijkl}^B = \Delta c_{ijkl} \approx 0$ and $\rho^A - \rho^B = \Delta \rho \approx 0$, it is allowed to neglect these terms.

3.1.2 Green's function due to an impulsive P wave source

The wave field emitted by a unit impulsive force in an elastic medium will consist of P and S waves. In the following modified elastic Green's functions will be derived due to either an impulsive P wave source or an impulsive S wave source.

From equations (3.15) and (3.16) $\Theta_{ij,m}$ may be eliminated leaving

$$\partial_j (c_{ijkl} \partial_l G_{k,m}) + \rho \omega^2 G_{i,m} = -\delta_{im} \delta(\mathbf{r} - \mathbf{r}_A). \quad (3.24)$$

Assume that the medium is locally isotropic at \mathbf{r}_A . Multiplying the left hand side and the right hand side of equation (3.24) by the operator

$$-K_c(\mathbf{r}_A)\partial_{m_A}, \quad (3.25)$$

where ∂_{m_A} for $m=1,2,3$ denotes spatial differentiation with respect to the Green's *source* point coordinates x_A, y_A, z_A , respectively, and where

$$K_c(\mathbf{r}_A) = \lambda(\mathbf{r}_A) + 2\mu(\mathbf{r}_A), \quad (3.26)$$

yields

$$\begin{aligned} \partial_j(c_{ijkl}\partial_l(-K_c(\mathbf{r}_A)\partial_{m_A}G_{k,m})) + \rho\omega^2(-K_c(\mathbf{r}_A)\partial_{m_A}G_{i,m}) = \\ K_c(\mathbf{r}_A)\delta_{im}\partial_{m_A}\delta(\mathbf{r}-\mathbf{r}_A) \end{aligned} \quad (3.27)$$

or, with $\partial_{m_A}\delta(\mathbf{r}-\mathbf{r}_A) = -\partial_m\delta(\mathbf{r}-\mathbf{r}_A)$,

$$\partial_j(c_{ijkl}\partial_lG_{k,\phi}) + \rho\omega^2G_{i,\phi} = -K_c(\mathbf{r}_A)\delta_{im}\partial_m\delta(\mathbf{r}-\mathbf{r}_A) \quad (3.28)$$

or, with $\delta_{im}\partial_m = \partial_i$,

$$\partial_j(c_{ijkl}\partial_lG_{k,\phi}) + \rho\omega^2G_{i,\phi} = -K_c(\mathbf{r}_A)\partial_i\delta(\mathbf{r}-\mathbf{r}_A), \quad (3.29)$$

where

$$G_{i,\phi}(\mathbf{r}, \mathbf{r}_A, \omega) = -K_c(\mathbf{r}_A)\partial_{m_A}G_{i,m}(\mathbf{r}, \mathbf{r}_A, \omega). \quad (3.30)$$

The Lamé coefficients λ and μ that appear in equation (3.26) are related to the stiffness coefficients, according to

$$c_{ijkl}(\mathbf{r}) = \lambda(\mathbf{r})\delta_{ij}\delta_{kl} + \mu(\mathbf{r})(\delta_{ik}\delta_{jl} + \delta_{il}\delta_{jk}). \quad (3.31)$$

The source term on the right hand side of (3.29) represents a P wave source at \mathbf{r}_A , if the medium is assumed to be isotropic and the gradient of the medium parameters is assumed to be zero at \mathbf{r}_A (Wapenaar and Haimé, 1990). The Green's displacement field $G_{i,\phi}(\mathbf{r}, \mathbf{r}_A, \omega)$ for $i=1,2,3$ are the three components of the Green's displacement vector $\mathbf{G}_\phi(\mathbf{r}, \mathbf{r}_A, \omega)$. The subscript ϕ stands for the Green's impulsive P wave source at \mathbf{r}_A . Note that the emitted P wave field may encounter all kinds of inhomogeneities on its way from source point \mathbf{r}_A to observation point \mathbf{r} . Therefore, the Green's wave field at observation point \mathbf{r} , $\mathbf{G}_\phi(\mathbf{r}, \mathbf{r}_A, \omega)$, may consist of both (*quasi-*) P and (*quasi-*) S waves.

Assuming in observation point \mathbf{r} as well that the medium is isotropic and that the gradient equals zero, a Green's P wave scalar potential in \mathbf{r} may be defined according to

$$\Gamma_{\phi,\phi}(\mathbf{r}, \mathbf{r}_A, \omega) = -K_c(\mathbf{r})\nabla \cdot \mathbf{G}_\phi(\mathbf{r}, \mathbf{r}_A, \omega) \quad (3.32)$$

or

$$\Gamma_{\phi,\phi}(\mathbf{r}, \mathbf{r}_A, \omega) = -K_c(\mathbf{r})\partial_i G_{i,\phi}(\mathbf{r}, \mathbf{r}_A, \omega), \quad (3.33)$$

and a Green's S wave vector potential by

$$\Gamma_{\psi,\phi}(\mathbf{r}, \mathbf{r}_A, \omega) = \mu(\mathbf{r})\nabla \times \mathbf{G}_\phi(\mathbf{r}, \mathbf{r}_A, \omega) \quad (3.34)$$

or

$$\Gamma_{\psi_k,\phi}(\mathbf{r}, \mathbf{r}_A, \omega) = -\mu(\mathbf{r})\epsilon_{kij}\partial_j G_{i,\phi}(\mathbf{r}, \mathbf{r}_A, \omega) \quad (3.35)$$

where the subscript ψ corresponds to the S wave character of the wave field and ε_{kij} represents the alternating tensor:

$\varepsilon_{kij} = 0$ if any of k, i, j are equal, otherwise

$$\varepsilon_{123} = \varepsilon_{312} = \varepsilon_{231} = -\varepsilon_{213} = -\varepsilon_{321} = -\varepsilon_{132} = 1.$$

$\Gamma_{\psi_k, \phi}$ for $k=1,2,3$ are the three components of the Green's S potential vector $\Gamma_{\psi, \phi}$ as defined in (3.34). The Greek symbol Γ denotes a Green's wave field potential. The first subscript corresponds to the wave type (ϕ for P or ψ for S) at observation point \mathbf{r} . The second subscript corresponds to the type of the Green's source (ϕ for P) at \mathbf{r}_A . Hence, Green's potentials with two different subscripts always correspond to converted wave fields.

3.1.3 Green's function due to an impulsive S wave source

Applying operator $-K_c(\mathbf{r}_A)\partial_{m_A}$ to wave equation (3.24) transformed the character of the Green's source from an impulsive force to an impulsive P wave source. Under the same assumptions, applying

$$-\mu(\mathbf{r}_A)\varepsilon_{hmn}\partial_{n_A} \quad (3.36)$$

to (3.24) transforms that same impulsive force to an impulsive S wave source. Hence,

$$\partial_j(c_{ijkl}\partial_l G_{k, \psi_h}) + \rho\omega^2 G_{i, \psi_h} = -\mu(\mathbf{r}_A)\varepsilon_{hin}\partial_n \delta(\mathbf{r} - \mathbf{r}_A), \quad (3.37)$$

where

$$G_{i, \psi_A}(\mathbf{r}, \mathbf{r}_A, \omega) = -\mu(\mathbf{r}_A)\varepsilon_{hmn}\partial_{n_A} G_{i, m}(\mathbf{r}, \mathbf{r}_A, \omega). \quad (3.38)$$

The right hand side of equation (3.37) now corresponds to a Green's S wave source polarized in the plane perpendicular to the h -axis, where $h=1,2,3$ stands for x, y or z respectively (Wapenaar and Haimé, 1990). $G_{i, \psi_h}(\mathbf{r}, \mathbf{r}_A, \omega)$ with

$i=1,2,3$ are the three components of the Green's displacement vector $\mathbf{G}_{\psi_h}(\mathbf{r}, \mathbf{r}_A, \omega)$. The subscript ψ_h refers to the S_h -wave character of the Green's source at \mathbf{r}_A . Again assuming the medium isotropic and with zero gradient in observation point \mathbf{r} a Green's P potential may be defined by

$$\Gamma_{\phi, \psi_h}(\mathbf{r}, \mathbf{r}_A, \omega) = -K_c(\mathbf{r}) \nabla \cdot \mathbf{G}_{\psi_h}(\mathbf{r}, \mathbf{r}_A, \omega) \quad (3.39)$$

or

$$\Gamma_{\phi, \psi_h}(\mathbf{r}, \mathbf{r}_A, \omega) = -K_c(\mathbf{r}) \partial_i G_{i, \psi_h}(\mathbf{r}, \mathbf{r}_A, \omega) , \quad (3.40)$$

and a Green's S wave vector potential by

$$\Gamma_{\psi, \psi_h}(\mathbf{r}, \mathbf{r}_A, \omega) = \mu(\mathbf{r}) \nabla \times \mathbf{G}_{\psi_h}(\mathbf{r}, \mathbf{r}_A, \omega) \quad (3.41)$$

or

$$\Gamma_{\psi_k, \psi_h}(\mathbf{r}, \mathbf{r}_A, \omega) = -\mu(\mathbf{r}) \varepsilon_{kij} \partial_j G_{i, \psi_h}(\mathbf{r}, \mathbf{r}_A, \omega) \quad (3.42)$$

where Γ_{ψ_k, ψ_h} represents the k th-component of Green's displacement vector $\mathbf{G}_{\psi, \psi_h}$ as defined in (3.34).

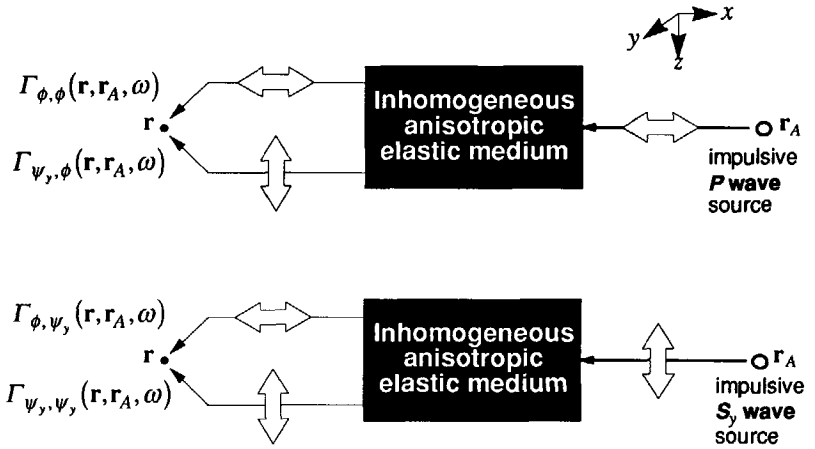
Fig. 3.2 gives an overview of the Green's potential functions due to an impulsive P wave source and due to an impulsive S_y wave source ($h=2$).

3.1.4 Reciprocity relations for Green's wave fields

Applying (3.14) to the Green's function, taking surface S at infinity yields

Fig. 3.2

Schematic overview
of elastic Green's
potential functions



$$G_{i,m}(\mathbf{r}, \mathbf{r}_A, \omega) = G_{m,i}(\mathbf{r}_A, \mathbf{r}, \omega). \quad (3.43)$$

From (3.30), (3.33), (3.35), (3.38), (3.40) and (3.42) together with this reciprocity relation the following reciprocity relations for the Green's potential functions can be derived

$$\Gamma_{\phi,\phi}(\mathbf{r}, \mathbf{r}_A, \omega) = \Gamma_{\phi,\phi}(\mathbf{r}_A, \mathbf{r}, \omega), \quad (3.44)$$

$$\Gamma_{\psi_k,\psi_k}(\mathbf{r}, \mathbf{r}_A, \omega) = \Gamma_{\psi_k,\psi_k}(\mathbf{r}_A, \mathbf{r}, \omega) \quad (3.45)$$

and

$$\Gamma_{\psi_k,\phi}(\mathbf{r}, \mathbf{r}_A, \omega) = \Gamma_{\phi,\psi_k}(\mathbf{r}_A, \mathbf{r}, \omega). \quad (3.46)$$

3.1.5 Modified Kirchhoff-Helmholtz integral

Kirchhoff-Helmholtz integral (3.23) states that the elastic wave field in terms of displacements $U_m(\mathbf{r}_A, \omega)$ can be calculated in any point inside an elastic medium V by integrating the interaction of the Green's function with the physical wave field over surface S . In this section the physical wave field in the Kirchhoff-Helmholtz integral (3.23), that is still in terms of stresses and displacements, will be transformed to a wave field that is entirely in terms of P and S potentials.

The P potential in \mathbf{r}_A according to (3.32) may be defined by

$$\Phi(\mathbf{r}_A, \omega) = -K_c(\mathbf{r}_A) \nabla_A \cdot \mathbf{U}(\mathbf{r}_A, \omega) \quad (3.47)$$

or

$$\Phi(\mathbf{r}_A, \omega) = -K_c(\mathbf{r}_A) \partial_{m_A} U_m(\mathbf{r}_A, \omega) \quad (3.48)$$

where ∇_A and ∂_{m_A} denote differentiation with respect to coordinates x_A, y_A, z_A , respectively. Substituting Kirchhoff-Helmholtz integral (3.23) in (3.48) and changing the order of integration (along $S(\mathbf{r})$) and differentiation at \mathbf{r}_A yields

$$\begin{aligned} \Phi(\mathbf{r}_A, \omega) = - \oint_S \left[\left(-K_c(\mathbf{r}_A) \partial_{m_A} \Theta_m(\mathbf{r}, \mathbf{r}_A, \omega) \right) \mathbf{U}(\mathbf{r}, \omega) \right. \\ \left. - \mathbf{T}(\mathbf{r}, \omega) \left(-K_c(\mathbf{r}_A) \partial_{m_A} \mathbf{G}_m(\mathbf{r}, \mathbf{r}_A, \omega) \right) \right] \cdot \mathbf{n} dS \end{aligned} \quad (3.49)$$

or

$$\Phi(\mathbf{r}_A, \omega) = \oint_S \left[\mathbf{T}(\mathbf{r}, \omega) \mathbf{G}_\phi(\mathbf{r}, \mathbf{r}_A, \omega) - \mathbf{\Theta}_\phi(\mathbf{r}, \mathbf{r}_A, \omega) \mathbf{U}(\mathbf{r}, \omega) \right] \cdot \mathbf{n} dS \quad (3.50)$$

with

$$\mathbf{G}_\phi(\mathbf{r}, \mathbf{r}_A, \omega) = -K_c(\mathbf{r}_A) \partial_{m_A} \mathbf{G}_m(\mathbf{r}, \mathbf{r}_A, \omega) \quad (3.51)$$

and

$$\mathbf{\Theta}_\phi(\mathbf{r}, \mathbf{r}_A, \omega) = -K_c(\mathbf{r}_A) \partial_{m_A} \mathbf{\Theta}_m(\mathbf{r}, \mathbf{r}_A, \omega). \quad (3.52)$$

Equation (3.50) states that the P wave potential at \mathbf{r}_A can be expressed in terms of a surface integral over S where a Green's function is used that is due to an impulsive P wave source at \mathbf{r}_A .

Similarly, the S potential at \mathbf{r}_A may according to (3.34) be defined by

$$\mathbf{\Psi}(\mathbf{r}_A, \omega) = \mu(\mathbf{r}_A) \nabla_A \times \mathbf{U}(\mathbf{r}_A, \omega) \quad (3.53)$$

or

$$\Psi_h(\mathbf{r}_A, \omega) = -\mu(\mathbf{r}_A) \epsilon_{hmn} \partial_{n_A} U_m(\mathbf{r}_A, \omega) \quad (3.54)$$

where Ψ_h for $h=1,2,3$ are the three components of $\mathbf{\Psi}$. Substituting Kirchhoff-Helmholtz integral (3.23) in (3.54) and changing the order of integration (along $S(\mathbf{r})$) and differentiation at \mathbf{r}_A yields

$$\Psi_h(\mathbf{r}_A, \omega) = \oint_S \left[\mathbf{T}(\mathbf{r}, \omega) \mathbf{G}_{\Psi_h}(\mathbf{r}, \mathbf{r}_A, \omega) - \mathbf{\Theta}_{\Psi_h}(\mathbf{r}, \mathbf{r}_A, \omega) \mathbf{U}(\mathbf{r}, \omega) \right] \cdot \mathbf{n} dS \quad (3.55)$$

with

$$\mathbf{G}_{\Psi_h}(\mathbf{r}, \mathbf{r}_A, \omega) = -\mu(\mathbf{r}_A) \varepsilon_{hmn} \partial_{n_A} \mathbf{G}_m(\mathbf{r}, \mathbf{r}_A, \omega) \quad (3.56)$$

and

$$\mathbf{\Theta}_{\Psi_h}(\mathbf{r}, \mathbf{r}_A, \omega) = -\mu(\mathbf{r}_A) \varepsilon_{hmn} \partial_{n_A} \mathbf{\Theta}_m(\mathbf{r}, \mathbf{r}_A, \omega). \quad (3.57)$$

Equation (3.55) states that the S_h wave potential at \mathbf{r}_A can be expressed in terms of a surface integral over S where a Green's function is used that is due to an impulsive S_h wave source at \mathbf{r}_A .

Summary. What has been achieved in this section is that aside from the traditional form of the Kirchhoff-Helmholtz integral (3.23), which expresses the *displacement* field in some point \mathbf{r}_A inside an elastic medium in terms of a surface integral, two other Kirchhoff-Helmholtz integrals have been derived expressing either the P potential (3.50) or the S potential (3.55) in \mathbf{r}_A in terms of a surface integral. The Green's sources used in (3.50) and (3.55) are impulsive P and S sources respectively, whereas in (3.23) an impulsive *force* is to be used. In this respect one may say that the Green's function is *decomposed* at the source side into P and S components.

Kirchhoff-Helmholtz integrals (3.23), (3.50) and (3.55) can be captured in a somewhat more general notation given by

$$\Omega(\mathbf{r}_A, \omega) = \oint_S \left[\mathbf{T}(\mathbf{r}, \omega) \mathbf{G}_{\Omega}(\mathbf{r}, \mathbf{r}_A, \omega) - \mathbf{\Theta}_{\Omega}(\mathbf{r}, \mathbf{r}_A, \omega) \mathbf{U}(\mathbf{r}, \omega) \right] \cdot \mathbf{n} dS \quad (3.58)$$

with Ω , G_Ω and Θ_Ω given in Table 3-1.

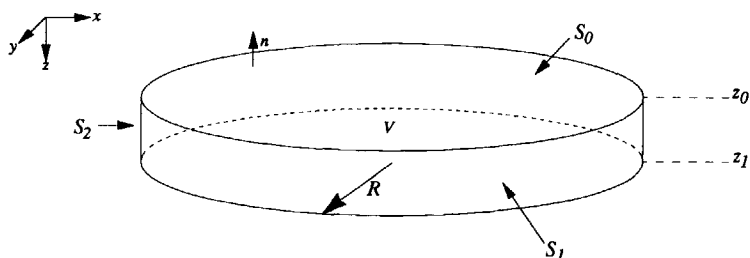
Table 3-1

Ω :	U_m	or	Φ	or	Ψ_h
G_Ω :	G_m	or	G_ϕ	or	G_{Ψ_h}
Θ_Ω :	Θ_m	or	Θ_ϕ	or	Θ_{Ψ_h}

3.2 Modified Rayleigh integrals

We shall now consider the special situation where the closed surface S enclosing volume V is shaped as a pill box (see Fig. 3.3). Surface S can be divided into three connected surfaces; a flat surface on top of the disc S_0 (at level z_0), a flat surface closing the disc at the bottom S_1 (at level z_1) and a cylindrically shaped surface S_2 with radius R . Assuming that all physical sources are above S_0 it is allowed to choose surfaces S_1 and S_2 in infinity, i.e. letting $z_1 \rightarrow \infty$ and $R \rightarrow \infty$. In that case the contribution of the surface integrals over S_1 and S_2 vanishes (Bleistein, 1984; Wapenaar and Berkhout, 1989) and (3.58) can now be written as

Fig. 3.3
Elastic medium V
with surface S and
outward pointing
normal vector \mathbf{n} .



$$\Omega(\mathbf{r}_A, \omega) = \iint_{S_0} [\mathbf{T}(\mathbf{r}_0, \omega) \mathbf{G}_\Omega(\mathbf{r}_0, \mathbf{r}_A, \omega) - \Theta_\Omega(\mathbf{r}_0, \mathbf{r}_A, \omega) \mathbf{U}(\mathbf{r}_0, \omega)] \cdot \mathbf{n} dx dy \quad (3.59)$$

or, using the fact that \mathbf{n} points in the negative z -direction at z_0 ,

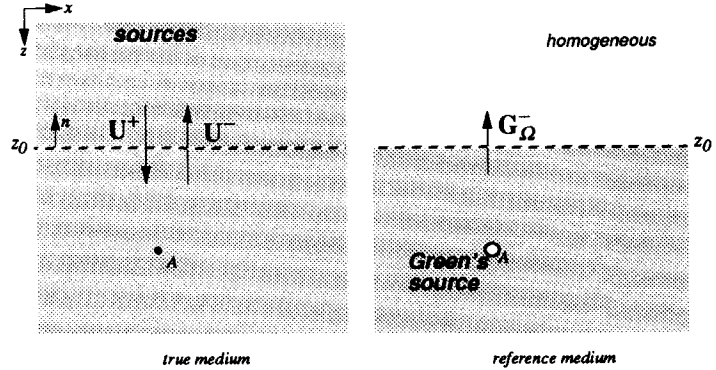
$$\Omega(\mathbf{r}_A, \omega) = \iint_{S_0} [\Theta_{z,\Omega}(\mathbf{r}_0, \mathbf{r}_A, \omega) \cdot \mathbf{U}(\mathbf{r}_0, \omega) - \mathbf{G}_\Omega(\mathbf{r}_0, \mathbf{r}_A, \omega) \cdot \mathbf{T}_z(\mathbf{r}_0, \omega)] dx dy \quad (3.60)$$

where $\mathbf{r}_0 = (x, y, z_0)$, $\Theta_{z,\Omega} (= -\Theta_\Omega \mathbf{n} = \Theta_\Omega \mathbf{i}_z)$ represents the third column of Green's tensor Θ_Ω and $\mathbf{T}_z (= -\mathbf{T} \mathbf{n} = \mathbf{T} \mathbf{i}_z)$ represents the third column of wave field tensor \mathbf{T} and use has been made of the symmetry properties of \mathbf{T} and Θ_Ω .

For the following analysis it is assumed that at z_0 the medium is isotropic and that the gradient of the medium parameters is equal to zero. At z_0 the wave field can be thought of to consist of *up*- and *downgoing* wave fields (see Fig. 3.4). Thus, for the displacement at z_0 the following can be written

Fig. 3.4

Cross section of elastic medium V with the up- and downgoing physical wave field and the Green's function through S_0 at level z_0 . Surfaces S_1 and S_2 are chosen in infinity.



$$\mathbf{U} = \mathbf{U}^- + \mathbf{U}^+ \quad (3.61)$$

and for the traction at z_0

$$\mathbf{T}_z = \mathbf{T}_z^- + \mathbf{T}_z^+, \quad (3.62)$$

where the superscripts $-$ and $+$ denote up- and downgoing wave fields respectively. Similarly, for the Green's function the following holds for the displacement at z_0

$$\mathbf{G}_\Omega = \mathbf{G}_\Omega^- + \mathbf{G}_\Omega^+ \quad (3.63)$$

and for the traction at z_0

$$\boldsymbol{\Theta}_{z,\Omega} = \boldsymbol{\Theta}_{z,\Omega}^- + \boldsymbol{\Theta}_{z,\Omega}^+. \quad (3.64)$$

With (3.61), (3.62), (3.63) and (3.64) Kirchhoff-Helmholtz integral (3.60) becomes

$$\Omega(\mathbf{r}_A, \omega) = \iint_{S_0} \left[\left(\boldsymbol{\Theta}_{z,\Omega}^- + \boldsymbol{\Theta}_{z,\Omega}^+ \right) \cdot \left(\mathbf{U}^- + \mathbf{U}^+ \right) - \left(\mathbf{G}_\Omega^- + \mathbf{G}_\Omega^+ \right) \cdot \left(\mathbf{T}_z^- + \mathbf{T}_z^+ \right) \right] dx dy. \quad (3.65)$$

Without loss of generality it is allowed to choose the reference medium for the Green's function above z_0 (including z_0) homogeneous. Since the Green's source is positioned below z_0 , it means that there is only an upgoing Green's wave field through surface z_0 (see Fig. 3.4). Hence, at z_0 the Green's function (3.63) reduces to

$$\mathbf{G}_{\Omega} = \mathbf{G}_{\Omega}^{-} \quad (3.66)$$

and (3.64) to

$$\boldsymbol{\Theta}_{z,\Omega} = \boldsymbol{\Theta}_{z,\Omega}^{-}, \quad (3.67)$$

and with this choice (3.65) becomes

$$\Omega(\mathbf{r}_A, \omega) = \iint_{S_0} \left[\boldsymbol{\Theta}_{z,\Omega}^{-} \cdot (\mathbf{U}^{-} + \mathbf{U}^{+}) - \mathbf{G}_{\Omega}^{-} \cdot (\mathbf{T}_z^{-} + \mathbf{T}_z^{+}) \right] dx dy. \quad (3.68)$$

Applying Parseval's theorem (Dudgeon and Mersereau, 1984) to Kirchhoff-Helmholtz integral (3.68) yields

$$\Omega(\mathbf{r}_A, \omega) = \left(\frac{1}{2\pi} \right)^2 \iint_{-\infty}^{+\infty} \left[\tilde{\boldsymbol{\Theta}}_{z,\Omega}^{\prime-} \cdot (\tilde{\mathbf{U}}^{-} + \tilde{\mathbf{U}}^{+}) - \tilde{\mathbf{G}}_{\Omega}^{\prime-} \cdot (\tilde{\mathbf{T}}_z^{-} + \tilde{\mathbf{T}}_z^{+}) \right]_{z_0} dk_x dk_y. \quad (3.69)$$

The prime accompanying the Green's function indicates that k_x and k_y are replaced by $-k_x$ and $-k_y$ respectively; i.e. $\tilde{\mathbf{G}}_{\Omega}^{\prime-} = \tilde{\mathbf{G}}_{\Omega}^{-}(-k_x, -k_y, z_0; x_A, y_A, z_A; \omega)$ and $\tilde{\boldsymbol{\Theta}}_{z,\Omega}^{\prime-} = \tilde{\boldsymbol{\Theta}}_{z,\Omega}^{-}(-k_x, -k_y, z_0; x_A, y_A, z_A; \omega)$. After collecting terms of up- and downgoing wave fields this equation can also be written as

$$\begin{aligned} \Omega(\mathbf{r}_A, \omega) = & \left(\frac{1}{2\pi} \right)^2 \iint_{-\infty}^{+\infty} \left[(\tilde{\boldsymbol{\Theta}}_{z,\Omega}^{\prime-} \cdot \tilde{\mathbf{U}}^{-} - \tilde{\mathbf{G}}_{\Omega}^{\prime-} \cdot \tilde{\mathbf{T}}_z^{-}) + (\tilde{\boldsymbol{\Theta}}_{z,\Omega}^{\prime-} \cdot \tilde{\mathbf{U}}^{+} - \tilde{\mathbf{G}}_{\Omega}^{\prime-} \cdot \tilde{\mathbf{T}}_z^{+}) \right]_{z_0} dk_x dk_y \\ & (3.70) \end{aligned}$$

The first term in the integral between parentheses corresponds to the interaction between the Green's function, which is only upgoing, and the upgoing part of the wave field at z_0 . Obviously, this wave field must be a scattered wave field since the sources are assumed above z_0 . The second term between parentheses corresponds to the interaction of the Green's function and the downgoing part of the wave field at z_0 . It is shown below that the first term between parentheses vanishes and that the second term can be rewritten in terms of P and S wave potentials.

We may define P and S potentials for the physical wave field at z_0 as follows

$$U(r_0, \omega) = \frac{1}{\rho\omega^2} (\nabla\Phi + \nabla \times \Psi) ; \nabla \cdot \Psi = 0 \quad (3.71)$$

or, equivalently with (3.61),

$$U^\pm(r_0, \omega) = \frac{1}{\rho\omega^2} (\nabla\Phi^\pm + \nabla \times \Psi^\pm) ; \nabla \cdot \Psi^\pm = 0 \quad (3.72)$$

and for the Green's function

$$G_\Omega(r_0, r_A, \omega) = \frac{1}{\rho\omega^2} (\nabla\Gamma_{\phi, \Omega} + \nabla \times \Gamma_{\psi, \Omega}) ; \nabla \cdot \Gamma_{\psi, \Omega} = 0 \quad (3.73)$$

or, with (3.66),

$$G_\Omega^-(r_0, r_A, \omega) = \frac{1}{\rho\omega^2} (\nabla\Gamma_{\phi, \Omega}^- + \nabla \times \Gamma_{\psi, \Omega}^-) ; \nabla \cdot \Gamma_{\psi, \Omega}^- = 0. \quad (3.74)$$

In the wavenumber-frequency domain the two-way wave equations for P and S waves read

$$\frac{\partial^2 \tilde{\Phi}}{\partial z^2} = -k_{z,p}^2 \tilde{\Phi} \quad (3.75)$$

and

$$\frac{\partial^2 \tilde{\Psi}}{\partial z^2} = -k_{z,s}^2 \tilde{\Psi} \quad (3.76)$$

respectively, where the tilde \sim denotes the wavenumber domain and where

$$k_{z,p}^2 = \frac{\omega^2}{c_p^2} - k_x^2 - k_y^2 \quad (3.77)$$

and

$$k_{z,s}^2 = \frac{\omega^2}{c_s^2} - k_x^2 - k_y^2, \quad (3.78)$$

where c_p and c_s stand for the compressional and shear wave velocity respectively. The relation between these velocities and the Lamé parameters is given by

$$c_p = \sqrt{\frac{\lambda + 2\mu}{\rho}} \quad (3.79)$$

and

$$c_s = \sqrt{\frac{\mu}{\rho}}. \quad (3.80)$$

From (3.75) and (3.76) the *one-way wave equations* follow immediately,

$$\frac{\partial \tilde{\Phi}^\pm}{\partial z} = \mp i k_{z,p} \tilde{\Phi}^\pm \quad (3.81)$$

and

$$\frac{\partial \tilde{\Psi}^\pm}{\partial z} = \mp i k_{z,s} \tilde{\Psi}^\pm \quad (3.82)$$

where

$$k_{z,p} = +\sqrt{k_p^2 - k_x^2 - k_y^2} \quad \text{for } k_p^2 \geq k_x^2 + k_y^2; \quad k_p = \frac{\omega}{c_p}, \quad (3.83)$$

$$k_{z,p} = -i\sqrt{k_x^2 + k_y^2 - k_p^2} \quad \text{for } k_p^2 < k_x^2 + k_y^2, \quad (3.84)$$

$$k_{z,s} = +\sqrt{k_s^2 - k_x^2 - k_y^2} \quad \text{for } k_s^2 \geq k_x^2 + k_y^2; \quad k_s = \frac{\omega}{c_s} \quad (3.85)$$

and

$$k_{z,s} = -i\sqrt{k_x^2 + k_y^2 - k_s^2} \quad \text{for } k_s^2 < k_x^2 + k_y^2. \quad (3.86)$$

In the wavenumber-frequency domain equation (3.72) together with (3.81) and (3.82) may be written as

$$\tilde{\mathbf{U}}^{\pm} = \tilde{\mathbf{D}}_p^{\pm} \tilde{\Phi}^{\pm} + \tilde{\mathbf{D}}_s^{\pm} \tilde{\Psi}^{\pm} ; \tilde{\mathbf{D}}_s^{\pm} \cdot \tilde{\Psi}^{\pm} = 0 \quad (3.87)$$

where

$$\tilde{\mathbf{D}}_p^{\pm} = \frac{1}{\rho\omega^2} \begin{pmatrix} -ik_x \\ -ik_y \\ \mp ik_{z,p} \end{pmatrix} ; \tilde{\mathbf{D}}_s^{\pm} = \frac{1}{\rho\omega^2} \begin{pmatrix} -ik_x \\ -ik_y \\ \mp ik_{z,s} \end{pmatrix} \quad (3.88)$$

and

$$\tilde{\mathbf{D}}_s^{\pm} = \frac{1}{\rho\omega^2} \begin{pmatrix} 0 & \pm ik_{z,s} & -ik_y \\ \mp ik_{z,s} & 0 & ik_x \\ ik_y & -ik_x & 0 \end{pmatrix}. \quad (3.89)$$

The traction is related to the displacements by equation (3.6). Using this relation and relation (3.31), that expresses the relation between the stiffness coefficients and the Lamé parameters for the isotropic situation, the relation between the traction and the P and S potentials is given by

$$\tilde{\mathbf{T}}_z^{\pm} = \tilde{\mathbf{E}}_p^{\pm} \tilde{\Phi}^{\pm} + \tilde{\mathbf{E}}_s^{\pm} \tilde{\Psi}^{\pm}, \quad (3.90)$$

where the operators $\tilde{\mathbf{E}}_p^{\pm}$ and $\tilde{\mathbf{E}}_s^{\pm}$ are related to operators $\tilde{\mathbf{D}}_p^{\pm}$ and $\tilde{\mathbf{D}}_s^{\pm}$ as follows

$$\tilde{\mathbf{E}}_p^\pm = \tilde{\mathbf{K}}_p^\pm \tilde{\mathbf{D}}_p^\pm \quad (3.91)$$

and

$$\tilde{\mathbf{E}}_s^\pm = \tilde{\mathbf{K}}_s^\pm \tilde{\mathbf{D}}_s^\pm, \quad (3.92)$$

where

$$\tilde{\mathbf{K}}_p^\pm = \begin{pmatrix} \mp \mu i k_{z,p} & 0 & -\mu i k_x \\ 0 & \mp \mu i k_{z,p} & -\mu i k_y \\ -\lambda i k_x & -\lambda i k_y & \mp (\lambda + 2\mu) i k_{z,p} \end{pmatrix} \quad (3.93)$$

and

$$\tilde{\mathbf{K}}_s^\pm = \begin{pmatrix} \mp \mu i k_{z,s} & 0 & -\mu i k_x \\ 0 & \mp \mu i k_{z,s} & -\mu i k_y \\ -\lambda i k_x & -\lambda i k_y & \mp (\lambda + 2\mu) i k_{z,s} \end{pmatrix}. \quad (3.94)$$

Expressions (3.87) and (3.90) relate the displacement and the stress to the P and S potential for the physical wave field respectively.

Similarly, the relation between the Green's displacement and the Green's potentials, analogous to (3.87), is given by

$$\tilde{\mathbf{G}}_{\Omega}^{\prime-} = \tilde{\mathbf{D}}_p^{\prime-} \tilde{\Gamma}_{\phi,\Omega}^{\prime-} + \tilde{\mathbf{D}}_s^{\prime-} \tilde{\Gamma}_{\psi,\Omega}^{\prime-}; \quad \tilde{\mathbf{D}}_s^{\prime-} \cdot \tilde{\Gamma}_{\psi,\Omega}^{\prime-} = 0 \quad (3.95)$$

and between the Green's stress and the Green's potentials, analogous to (3.90), by

$$\tilde{\Theta}_{z,\Omega}^{'-} = \tilde{\mathbf{E}}_p^{'-} \tilde{\Gamma}_{\phi,\Omega}^{'-} + \tilde{\mathbf{E}}_s^{'-} \tilde{\Gamma}_{\psi,\Omega}^{'-} \quad (3.96)$$

or using the following relations $\tilde{\mathbf{D}}_p^{'\pm} = -\tilde{\mathbf{D}}_p^{\mp}$; $\tilde{\mathbf{D}}_s^{'\pm} = -\tilde{\mathbf{D}}_s^{\mp}$; $\tilde{\mathbf{D}}_s^{'\pm} = -\tilde{\mathbf{D}}_s^{\mp}$ and $\tilde{\mathbf{E}}_p^{'\pm} = -\tilde{\mathbf{E}}_p^{\mp}$; $\tilde{\mathbf{E}}_s^{'\pm} = -\tilde{\mathbf{E}}_s^{\mp}$ (3.95) and (3.96) can also be written as

$$\tilde{\mathbf{G}}_{\Omega}^{'-} = -\tilde{\mathbf{D}}_p^+ \tilde{\Gamma}_{\phi,\Omega}^{'-} - \tilde{\mathbf{D}}_s^+ \tilde{\Gamma}_{\psi,\Omega}^{'-} ; \tilde{\mathbf{D}}_s^+ \cdot \tilde{\Gamma}_{\psi,\Omega}^{'-} = 0 \quad (3.97)$$

and

$$\tilde{\Theta}_{z,\Omega}^{'-} = -\tilde{\mathbf{E}}_p^+ \tilde{\Gamma}_{\phi,\Omega}^{'-} - \tilde{\mathbf{E}}_s^+ \tilde{\Gamma}_{\psi,\Omega}^{'-} \quad (3.98)$$

Substituting (3.87), (3.90), (3.97) and (3.98) yields after some calculus for the first term between parentheses in (3.70)

$$(\tilde{\Theta}_{z,\Omega}^{'-} \cdot \tilde{\mathbf{U}}^- - \tilde{\mathbf{G}}_{\Omega}^{'-} \cdot \tilde{\mathbf{T}}_z^-) = 0 \quad (3.99)$$

and for the second term

$$(\tilde{\Theta}_{z,\Omega}^{'-} \cdot \tilde{\mathbf{U}}^+ - \tilde{\mathbf{G}}_{\Omega}^{'-} \cdot \tilde{\mathbf{T}}_z^+) = [ik_{z,p} \tilde{\Gamma}_{\phi,\Omega}^{'-} \Phi^+ + ik_{z,s} \tilde{\Gamma}_{\psi,\Omega}^{'-} \cdot \tilde{\Psi}^+] \quad (3.100)$$

leaving

$$\Omega(\mathbf{r}_A, \omega) = \frac{2}{\rho\omega^2} \left(\frac{1}{2\pi} \right)^2 \int_{-\infty}^{+\infty} \int [ik_{z,p} \tilde{\Gamma}_{\phi,\Omega}^- \Phi^+ + ik_{z,s} \tilde{\Gamma}_{\psi,\Omega}^- \cdot \tilde{\Psi}^+]_{z_0} dk_x dk_y. \quad (3.101)$$

Substituting one-way wave equations (3.81) and (3.82) and applying Parseval's theorem again yields

$$\Omega(\mathbf{r}_A, \omega) = -2 \int \int_{S_0} \frac{1}{\rho\omega^2} \left[\Gamma_{\phi,\Omega}^- (\partial_z \Phi^+) + \Gamma_{\psi,\Omega}^- \cdot (\partial_z \Psi^+) \right] dx dy \quad (3.102)$$

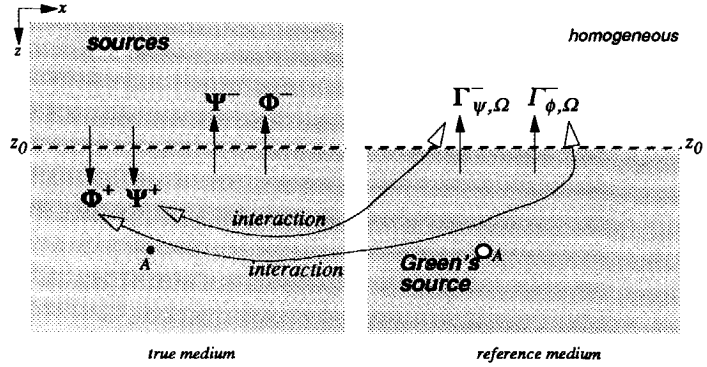
or, equivalently,

$$\Omega(\mathbf{r}_A, \omega) = 2 \int \int_{S_0} \frac{1}{\rho\omega^2} \left[(\partial_z \Gamma_{\phi,\Omega}^-) \Phi^+ + (\partial_z \Gamma_{\psi,\Omega}^-) \cdot \Psi^+ \right] dx dy. \quad (3.103)$$

These relations represent the one-way elastic Rayleigh I and the one-way elastic Rayleigh II integral respectively. These equations are exact under the assumption that the medium is locally homogeneous and isotropic at z_0 . From these integrals it can be seen that the terms that occur within the brackets involve the *upgoing* Green's function and the *downgoing* part of the wave field at z_0 (see Fig. 3.5). The interaction between the upgoing Green's function and the upgoing part of the wave field (i.e. the first term between parentheses in (3.70)) is equal to zero. Thus, in general there is no interaction between the Green's function and the wave field if they travel in *equal* directions. Also, there is no mixed interaction between P and S components at z_0 . There is only constructive interaction between P components if the Green's function and the physical wave field travel in *opposite* directions and similarly between S components that travel in opposite directions. Notice that in (3.102) and (3.103) $\Omega(\mathbf{r}_A, \omega)$ represents either the displacement U_m (with $m=1,2,3$) or the P potential Φ or the S_h potential Ψ_h at \mathbf{r}_A .

Fig. 3.5

Cross section of elastic medium V with the up- and downgoing potentials of the physical wave field and the upgoing Green's potentials through S_0 at level z_0 . Surfaces S_1 and S_2 are chosen in infinity.



3.2.1 Forward extrapolation operator for P waves

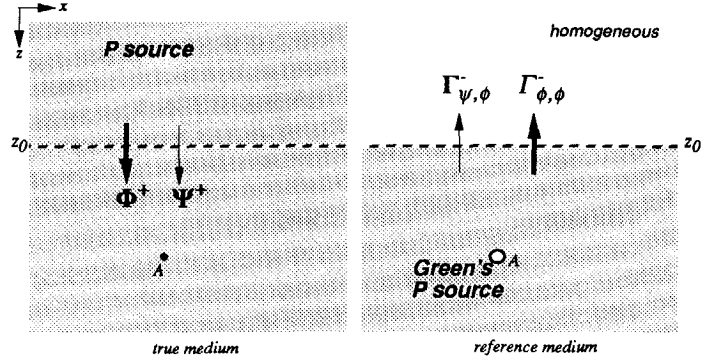
In the case that Ω represents the P potential a Green's impulsive P wave source must be used and then, for instance, Rayleigh II integral (3.103) becomes

$$\Phi(\mathbf{r}_A, \omega) = 2 \iint_{S_0} \frac{1}{\rho \omega^2} \left[(\partial_z \Gamma_{\phi, \phi}^-) \Phi^+ + (\partial_z \Gamma_{\psi, \phi}^-) \cdot \Psi^+ \right] dx dy. \quad (3.104)$$

The downgoing wave field at z_0 (Φ^+ and Ψ^+) consists of a primary part (directly from the source) and a multiply scattered part. If the source emits P waves only then the S waves (Ψ^+) will consist of converted waves only (see Fig. 3.6). Also, the Green's wave field at z_0 is due to an impulsive P wave source at \mathbf{r}_A and therefore the Green's S potential at z_0 ($\Gamma_{\psi, \phi}^-$) will consist of converted waves only. Hence, the magnitude of the second term between brackets in (3.104) ($(\partial_z \Gamma_{\psi, \phi}^-) \cdot \Psi^+$) is proportional to multiply converted waves and is two orders lower than the first term ($(\partial_z \Gamma_{\phi, \phi}^-) \Phi^+$). Thus, for this situation, (3.104) may be approximated by

Fig. 3.6

If the sources above S_0 are P wave sources and the Green's source is also a P wave source then the interaction of the S components on S_0 will be of second order compared to the interaction of the P components.



$$\Phi(r_A, \omega) \approx 2 \iint_{S_0} \frac{I}{\rho \omega^2} \left[(\partial_z \Gamma_{\phi, \phi}^-) \Phi^+ \right] dx dy. \quad (3.105)$$

This result states that the P wave field in A can be reconstructed from the interaction of the decomposed downgoing P wave field and the decomposed upgoing P Green's function at z_0 . Amplitude errors are of second order only. In case of a homogeneous medium (3.105) is exact.

3.2.2 Forward extrapolation operator for S waves

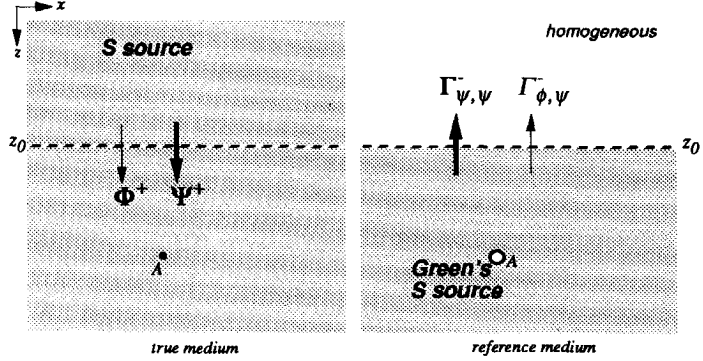
In the case that Ω represents the S_h potential a Green's S_h -wave source must be used and the Rayleigh II integral then becomes

$$\Psi_h(r_A, \omega) = 2 \iint_{S_0} \frac{I}{\rho \omega^2} \left[(\partial_z \Gamma_{\phi, \psi_h}^-) \Phi^+ + (\partial_z \Gamma_{\psi, \psi_h}^-) \cdot \Psi^+ \right] dx dy. \quad (3.106)$$

Assuming S wave sources only above z_0 , then with similar arguments as given above (but now the first term is two orders lower than the second term), (3.106) may be approximated by

Fig. 3.7

If the sources above S_0 are S wave sources and the Green's source is also a S wave source then the interaction of the P components on S_0 will be two orders lower compared to the interaction of the S components.



$$\Psi_h(\mathbf{r}_A, \omega) = 2 \iint_{S_0} \frac{1}{\rho \omega^2} \left[\left(\partial_z \Gamma_{\psi, \psi}^- \right) \cdot \Psi^+ \right] dx dy. \quad (3.107)$$

Thus the S wave field in A can be reconstructed from the interaction of the decomposed downgoing S wave field and the decomposed upgoing S Green's function at z_0 . Amplitude errors are of second order only. In case of a homogeneous medium (3.107) is exact.

3.2.3 Extrapolation operators for primary up- and downgoing waves

Equations (3.104) and (3.106) express either the total P or total S wave potential in a point A in the subsurface and are exact in the situation where the (inhomogeneous, anisotropic) reference medium *exactly* matches the true medium from z_0 to infinity. Considering primary wave fields only in the macro model ($\Gamma \rightarrow \bar{\Gamma}$) then the primary downgoing P wave field in A may be written as

$$\Phi^+(\mathbf{r}_A, \omega) \approx 2 \iint_{S_0} \frac{1}{\rho \omega^2} \left[\left(\partial_z \bar{\Gamma}_{\phi, \phi}^- \right) \Phi^+ \right] dx dy \quad (3.108)$$

and for the primary downgoing S wave field in A

$$\Psi_h^+(\mathbf{r}_A, \omega) \approx 2 \iint_{S_0} \frac{1}{\rho \omega^2} \left[\left(\partial_z \bar{\Gamma}_{\psi, \psi_h}^- \right) \cdot \Psi^+ \right] dx dy. \quad (3.109)$$

In a similar way the primary upgoing waves at \mathbf{r}_A can be expressed in terms of integrals at S_I below \mathbf{r}_A . The primary upgoing P wave field in A reads

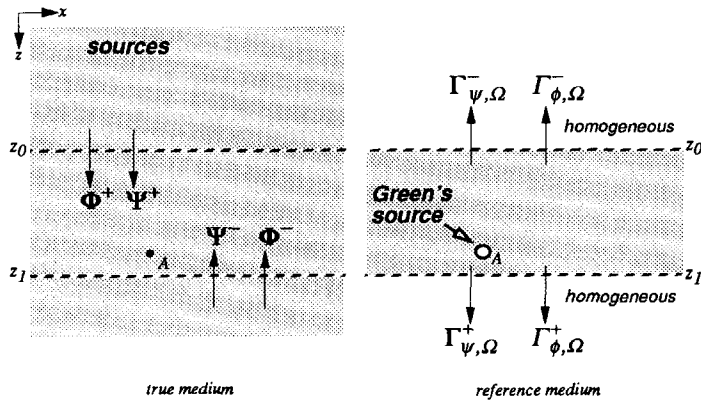
$$\Phi_h^-(\mathbf{r}_A, \omega) \approx -2 \iint_{S_I} \frac{1}{\rho \omega^2} \left[\left(\partial_z \bar{\Gamma}_{\phi, \phi}^+ \right) \Phi^- \right] dx dy \quad (3.110)$$

and the primary upgoing S wave field in A reads

$$\Psi_h^-(\mathbf{r}_A, \omega) \approx -2 \iint_{S_I} \frac{1}{\rho \omega^2} \left[\left(\partial_z \bar{\Gamma}_{\psi, \psi_h}^+ \right) \cdot \Psi^- \right] dx dy. \quad (3.111)$$

Fig. 3.8

Cross section of elastic medium V with the up- and downgoing potentials of the physical wave field and the upgoing Green's potentials through S_0 at level z_0 . Surface S_2 is chosen in infinity.



3.2.4 Summary

The primary downgoing wave field (the incident wave field) in subsurface point A can be reconstructed from the downgoing wave field at z_0 (see Fig. 3.9 *a*) with *forward* operators (3.108) and (3.109), whereas the primary upgoing wave field in A can be reconstructed from the upgoing wave field at z_1 (see Fig. 3.9 *b*) with *forward* operators (3.110) and (3.111). Since in seismic practice there is no data available from z_1 , *inverse* extrapolation operators are needed that act upon the upgoing reflected data at z_0 in order to reconstruct the upgoing wave field in A . These inverse extrapolation operators use backward propagating Green's functions (see Fig. 3.9 *c* and *d*). The theory of the backward propagating Green's functions will be discussed in the next section.

3.3 Backward propagating Green's functions

In this section backward propagating Green's functions will be used for inverse wave field extrapolation.

3.3.1 Kirchhoff-Helmholtz integral with backward propagating Green's functions

Let Q_m be a new vector function defined by (compare with (3.22))

$$Q_m = \Theta_m^* U - \underline{T} G_m^*, \quad (3.112)$$

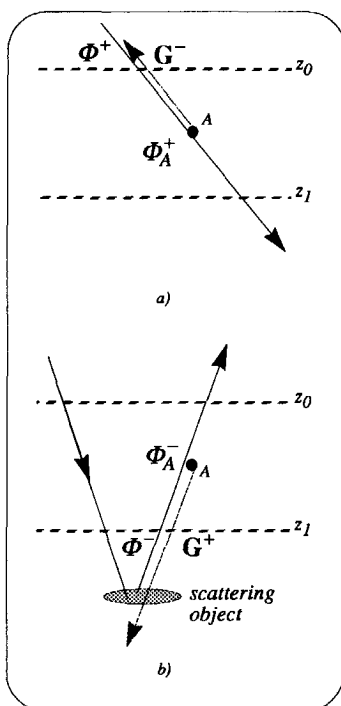
where $*$ denotes complex conjugation (by taking the complex conjugate the causal Green's function transforms to an anti-causal function). Applying the theorem of Gauss to (3.112) yields in analogy with eq. (3.23)

$$U_m(r_A, \omega) = -\oint_S \left(\Theta_m^*(r, r_A, \omega) U(r, \omega) - \underline{T}(r, \omega) G_m^*(r, r_A, \omega) \right) n dS \quad (3.113)$$

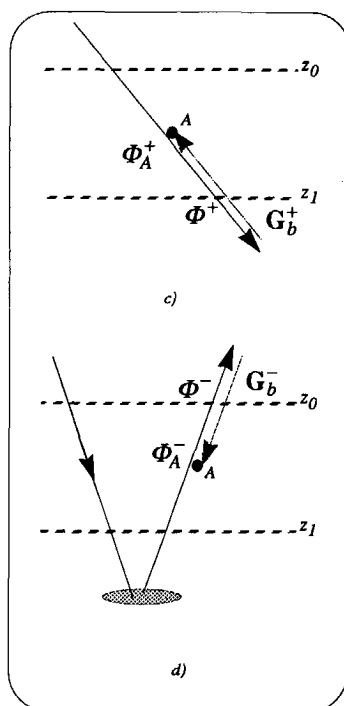
Fig. 3.9

With a forward propagating Green's function the upgoing wave field in A can be calculated from the upgoing wave field at z_1 , while with a backward propagating Green's function (G_b^-) that same wave field is calculated from the upgoing wave field at z_0 . The reference medium is chosen homogeneous above z_0 and below z_1 .

**Forward extrapolation with
Forward propagating
Green's functions**



**Inverse extrapolation with
Backward propagating
Green's functions**



Helmholtz integral (3.113) is exact and is equivalent to (3.23). Following a similar path as already taken in the derivation of (3.50) and (3.55) the next two Kirchhoff-Helmholtz integrals can be obtained

$$\Phi(\mathbf{r}_A, \omega) = \iint_S \left[\mathbf{T}(\mathbf{r}, \omega) \mathbf{G}_\phi^*(\mathbf{r}, \mathbf{r}_A, \omega) - \mathbf{\Theta}_\phi^*(\mathbf{r}, \mathbf{r}_A, \omega) \mathbf{U}(\mathbf{r}, \omega) \right] \cdot \mathbf{n} dS \quad (3.114)$$

and

$$\Psi_h(\mathbf{r}_A, \omega) = \iint_S \left[\mathbf{T}(\mathbf{r}, \omega) \mathbf{G}_{\Psi_h}^*(\mathbf{r}, \mathbf{r}_A, \omega) - \mathbf{\Theta}_{\Psi_h}^*(\mathbf{r}, \mathbf{r}_A, \omega) \mathbf{U}(\mathbf{r}, \omega) \right] \cdot \mathbf{n} dS. \quad (3.115)$$

Again, these three integrals can be captured in the following way (compare eq.(3.58))

$$\Omega(\mathbf{r}_A, \omega) = \iint_S \left[\mathbf{T}(\mathbf{r}, \omega) \mathbf{G}_\Omega^*(\mathbf{r}, \mathbf{r}_A, \omega) - \mathbf{\Theta}_\Omega^*(\mathbf{r}, \mathbf{r}_A, \omega) \mathbf{U}(\mathbf{r}, \omega) \right] \cdot \mathbf{n} dS, \quad (3.116)$$

with Ω , \mathbf{G}_Ω^* and $\mathbf{\Theta}_\Omega^*$ given in Table 3-2.

Table 3-2

$\Omega :$	U_m	or	Φ	or	Ψ_h
$\mathbf{G}_\Omega^* :$	\mathbf{G}_m^*	or	\mathbf{G}_ϕ^*	or	$\mathbf{G}_{\Psi_h}^*$
$\mathbf{\Theta}_\Omega^* :$	$\mathbf{\Theta}_m^*$	or	$\mathbf{\Theta}_\phi^*$	or	$\mathbf{\Theta}_{\Psi_h}^*$

3.3.2 Rayleigh-integrals with backward propagating Green's functions

Consider the configuration of Fig. 3.9. Surface S_0 corresponds to the recording surface, thus the wave field is considered to be known only at surface S_0 (which corresponds to the seismic situation). Sources are again assumed to be present only above S_0 . For this situation Kirchhoff-Helmholtz integral may be divided into two separate integrals

$$\begin{aligned} \Omega(\mathbf{r}_A, \omega) = & \iint_{S_0} \left[\underline{\mathbf{T}}(\mathbf{r}_0, \omega) \mathbf{G}_{\Omega}^*(\mathbf{r}_0, \mathbf{r}_A, \omega) - \underline{\Theta}_{\Omega}^*(\mathbf{r}_0, \mathbf{r}_A, \omega) \mathbf{U}(\mathbf{r}_0, \omega) \right] \cdot \mathbf{n} dx dy + \\ & \iint_{S_1} \left[\underline{\mathbf{T}}(\mathbf{r}_I, \omega) \mathbf{G}_{\Omega}^*(\mathbf{r}_I, \mathbf{r}_A, \omega) - \underline{\Theta}_{\Omega}^*(\mathbf{r}_I, \mathbf{r}_A, \omega) \mathbf{U}(\mathbf{r}_I, \omega) \right] \cdot \mathbf{n} dx dy \end{aligned} \quad (3.117)$$

where $\mathbf{r}_0 = (x, y, z_0)$ and $\mathbf{r}_I = (x, y, z_I)$, or, using a somewhat more compact notation,

$$\Omega(\mathbf{r}_A, \omega) = \Omega_0(\mathbf{r}_A, \omega) + \Omega_I(\mathbf{r}_A, \omega), \quad (3.118)$$

where

$$\Omega_0(\mathbf{r}_A, \omega) = \iint_{S_0} \left[\underline{\mathbf{T}}(\mathbf{r}_0, \omega) \mathbf{G}_{\Omega}^*(\mathbf{r}_0, \mathbf{r}_A, \omega) - \underline{\Theta}_{\Omega}^*(\mathbf{r}_0, \mathbf{r}_A, \omega) \mathbf{U}(\mathbf{r}_0, \omega) \right] \cdot \mathbf{n} dx dy, \quad (3.119)$$

and

$$\Omega_I(\mathbf{r}_A, \omega) = \iint_{S_1} \left[\underline{\mathbf{T}}(\mathbf{r}_I, \omega) \mathbf{G}_{\Omega}^*(\mathbf{r}_I, \mathbf{r}_A, \omega) - \underline{\Theta}_{\Omega}^*(\mathbf{r}_I, \mathbf{r}_A, \omega) \mathbf{U}(\mathbf{r}_I, \omega) \right] \cdot \mathbf{n} dx dy. \quad (3.120)$$

Unlike in section 3.2, the integral over S_I does not vanish when S_I is moved infinitely downward. For the following analysis it is assumed that the medium at z_0 and z_I is isotropic and that the gradient of the medium parameters is zero. At z_0 and z_I it is allowed to separate the wave field into up- and downgoing P and S wave fields. The reference medium for the Green's function is chosen homogeneous above z_0 (including z_0) and below z_I (including z_I). Hence, at z_0 the Green's function is only upgoing and at z_I the Green's function is only downgoing. The contributions from S_0 and S_I may then be written as

$$\Omega_0(\mathbf{r}_A, \omega) = \iint_{S_0} \left[\mathbf{\Theta}_{z, \Omega}^{-*} \cdot (\mathbf{U}^- + \mathbf{U}^+) - \mathbf{G}_{\Omega}^{-*} \cdot (\mathbf{T}_z^- + \mathbf{T}_z^+) \right] dx dy \quad (3.121)$$

and

$$\Omega_I(\mathbf{r}_A, \omega) = - \iint_{S_I} \left[\mathbf{\Theta}_{z, \Omega}^{+*} \cdot (\mathbf{U}^- + \mathbf{U}^+) - \mathbf{G}_{\Omega}^{+*} \cdot (\mathbf{T}_z^- + \mathbf{T}_z^+) \right] dx dy, \quad (3.122)$$

respectively. Notice that in (3.121) and (3.122) complex conjugation of the Green's functions results in a Green's wave field that travels towards the Green's source. Thus, \mathbf{G}_{Ω}^{-*} (in (3.121)) is actually a Green's displacement field that travels in the *positive* z -direction.

Using (3.87) and (3.90) then for (3.121) and (3.122), after some calculus (similarly as in section 3.2), the following may be written

$$\Omega_0(\mathbf{r}_A, \omega) \approx 2 \iint_{S_0} \frac{1}{\rho \omega^2} \left[\left(\partial_z \Gamma_{\phi, \Omega}^- \right)^* \Phi^- + \left(\partial_z \Gamma_{\psi, \Omega}^- \right)^* \Psi^- \right] dx dy \quad (3.123)$$

and

$$\Omega_I(\mathbf{r}_A, \omega) \approx -2 \iint_{S_I} \frac{1}{\rho \omega^2} \left[\left(\partial_z \Gamma_{\phi, \Omega}^+ \right)^* \Phi^+ + \left(\partial_z \Gamma_{\psi, \Omega}^+ \right)^* \cdot \Psi^+ \right] dx dy. \quad (3.124)$$

In the derivation of (3.123) and (3.124) it is assumed that the wavenumbers $k_{z,p}$ and $k_{z,s}$ satisfy

$$k_{z,p} = k_{z,p}^* \quad (3.125)$$

and

$$k_{z,s} = k_{z,s}^* \quad (3.126)$$

at z_0 and z_I . Equations (3.125) and (3.126) and, therefore, also (3.123) and (3.124), only hold for *propagating* waves. In other words, *evanescent* waves are not correctly handled.

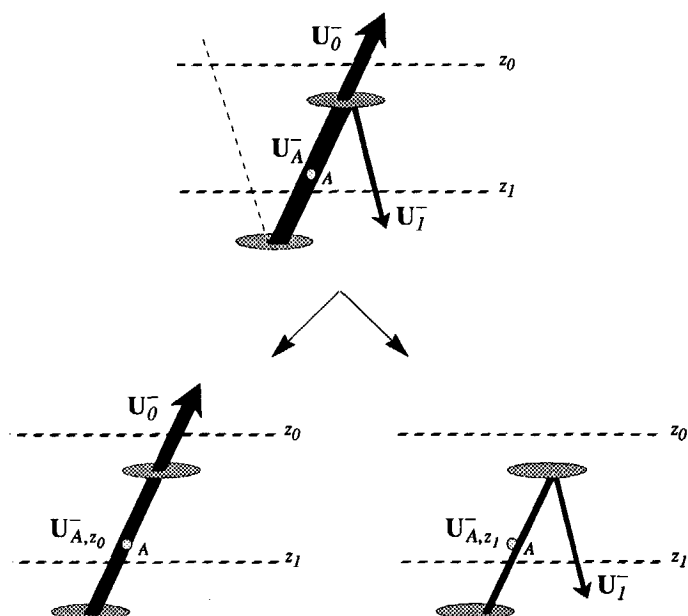
From Fig. 3.9 *d* it is clear that with the use of a backward propagating Green's function the *upgoing* wave field through A can be obtained by integration over surface S_0 only. There is, however, still a missing upgoing part as illustrated in Fig. 3.10. This missing part is caused by inhomogeneities above A . A small portion of the upgoing wave field will be scattered back by these inhomogeneities and will travel as a downgoing wave field through S_I . Hence, the *upgoing* wave field in A may be written as

$$\Omega^-(\mathbf{r}_A, \omega) = \Omega_0(\mathbf{r}_A, \omega) + \Omega_I^-(\mathbf{r}_A, \omega) \quad (3.127)$$

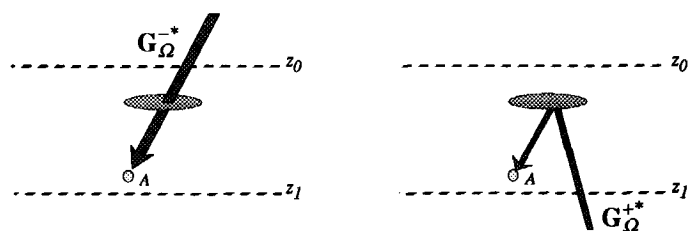
or

Fig. 3.10

The upgoing wave field in A can be divided into a transmitted part that continues through z_0 and a reflected part that continues through z_1 . The same can be done with the Green's function. If the contrasts are not too strong between z_0 and z_1 the contribution of the interacting wave field and the Green's function at z_1 may be considered a second order effect compared to the contribution from z_0 .



The upgoing wave field through A can be divided in a transmitted and a reflected part



Splitting up the back-propagating Green's function leaves a transmitted part and a reflected part that act upon the wave field at z_0 and z_1 respectively.

$$\begin{aligned}\Omega^-(\mathbf{r}_A, \omega) = & 2 \iint_{S_0} \frac{1}{\rho \omega^2} \left[\left(\partial_z \Gamma_{\phi, \Omega}^- \right)^* \Phi^- + \left(\partial_z \Gamma_{\psi, \Omega}^- \right)^* \cdot \Psi^- \right] dx dy \\ & - 2 \iint_{S_1} \frac{1}{\rho \omega^2} \left[\left(\partial_z \Gamma_{\phi, \Omega}^+ \right)^* \Phi^+ + \left(\partial_z \Gamma_{\psi, \Omega}^+ \right)^* \cdot \Psi^+ \right] dx dy. \quad (3.128)\end{aligned}$$

Since the wave field is only known on S_0 this small part of the upgoing wave field in A can not be taken into account and will express itself as an error in the amplitude of the upgoing wave field in A . If the contrasts between z_0 and z_1 are weak to moderate (which is certainly the case in seismic practice) it is allowed to neglect this term since this term is an interaction of a scattered wave field and a scattered Green's function (Fig. 3.10). Neglecting this term will cause a second order amplitude error only. Hence, by neglecting the error term $\Omega_l^-(\mathbf{r}_A, \omega)$ the upgoing wave field in A can be written as

$$\Omega^-(\mathbf{r}_A, \omega) \approx 2 \iint_{S_0} \frac{1}{\rho \omega^2} \left[\left(\partial_z \Gamma_{\phi, \Omega}^- \right)^* \Phi^- + \left(\partial_z \Gamma_{\psi, \Omega}^- \right)^* \cdot \Psi^- \right] dx dy. \quad (3.129)$$

3.3.3 Inverse extrapolation operator for primary P waves

Similar as in section 3.2.3 only primary wave fields will be considered in the macro model ($\Gamma \rightarrow \bar{\Gamma}$). The *upgoing* primary P potential in A can be obtained by choosing an impulsive P wave source for the Green's function, in that case (3.129) becomes

$$\Phi^-(\mathbf{r}_A, \omega) \approx 2 \iint_{S_0} \frac{1}{\rho \omega^2} \left[\left(\partial_z \bar{\Gamma}_{\phi, \phi}^- \right)^* \Phi^- \right] dx dy. \quad (3.130)$$

Similarly, the *downgoing* primary P wave field in A reads

$$\Phi^+(\mathbf{r}_A, \omega) \approx 2 \iint_{S_I} \frac{1}{\rho \omega^2} \left[\left(\partial_z \bar{\Gamma}_{\phi, \phi}^+ \right)^* \Phi^+ \right] dx dy . \quad (3.131)$$

3.3.4 Inverse extrapolation operator for *primary S waves*

For the primary S_h potential an impulsive S_h wave source is chosen for the Green's function and (3.129) then becomes

$$\Psi_h^-(\mathbf{r}_A, \omega) \approx -2 \iint_{S_0} \frac{1}{\rho \omega^2} \left[\left(\partial_z \bar{\Gamma}_{\psi, \psi_h}^- \right)^* \cdot \Psi^- \right] dx dy . \quad (3.132)$$

Similarly, the primary downgoing S wave in A reads

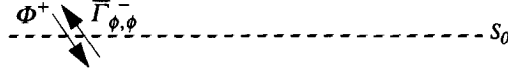
$$\Psi_h^+(\mathbf{r}_A, \omega) \approx -2 \iint_{S_I} \frac{1}{\rho \omega^2} \left[\left(\partial_z \bar{\Gamma}_{\psi, \psi_h}^+ \right)^* \cdot \Psi^+ \right] dx dy . \quad (3.133)$$

3.3.5 Summary

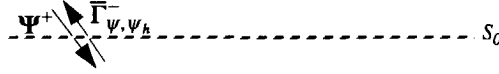
Equations (3.130) and (3.132) represent non-recursive inverse wave field extrapolation operators for propagating P and S waves respectively. The *upgoing* wave field in a point A in the medium below (acquisition) surface S_0 is expressed in terms of a surface integral over S_0 . In case of inhomogeneities (not too severe) amplitude errors are of second order only, which corresponds to the negligence of multiply reflected and multiply converted waves. For high contrast media the error term $\Omega_I^-(\mathbf{r}_A, \omega)$ may no longer be neglected and should be estimated in an iterative way (Wapenaar and Berkhout, 1989). Together with equation (3.108) and (3.109) these equations express the up- and downgoing (reflected and incident) primary P wave field or primary S wave field respectively in point A (see Fig. 3.11).

Fig. 3.11

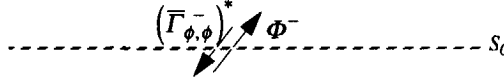
Overview of primary down- and upgoing P and S waves in a point A in the subsurface in terms of an integral over surface S_0 .



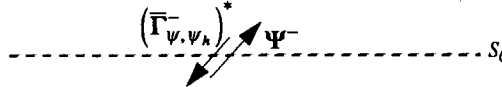
$$A \bullet \quad \Phi^+(\mathbf{r}_A, \omega) \approx 2 \iint_{S_0} \frac{1}{\rho \omega^2} \left[\left(\partial_z \bar{\Gamma}_{\phi,\phi}^- \right) \Phi^+ \right] dx dy$$



$$A \bullet \quad \Psi_h^+(\mathbf{r}_A, \omega) \approx 2 \iint_{S_0} \frac{1}{\rho \omega^2} \left[\left(\partial_z \bar{\Gamma}_{\psi,\psi_h}^- \right) \Psi^+ \right] dx dy$$



$$A \bullet \quad \Phi^-(\mathbf{r}_A, \omega) \approx 2 \iint_{S_0} \frac{1}{\rho \omega^2} \left[\left(\partial_z \bar{\Gamma}_{\phi,\phi}^- \right)^* \Phi^- \right] dx dy$$



$$A \bullet \quad \Psi_h^-(\mathbf{r}_A, \omega) \approx 2 \iint_{S_0} \frac{1}{\rho \omega^2} \left[\left(\partial_z \bar{\Gamma}_{\psi,\psi_h}^- \right)^* \Psi^- \right] dx dy$$

For the generation of Green's functions a reference medium is needed describing the relevant parameters for wave propagation as a function of space and time. In seismics such a reference medium is often referred to as a 'macro model' (see also Chapter 3, section 3.1.1). In the elastic situation, besides a velocity model for the *P* waves, also a velocity model is needed for the *S* waves. A macro model is estimated from the most important horizons that occur in the seismic data, therefore a macro model describes mainly the propagation properties of the subsurface. Very small contrasts or rapidly changing horizons in the true medium are of minor influence on the traveltimes of the wave field that travels from the surface to the target and vice versa.

The amplitude of a wave field propagating through a complex medium is subjected to a number of influences which can be categorized as follows:

- 1) Geometrical spreading
- 2) Angle dependent transmission effects, at macro boundaries
- 3) Angle dependent transmission effects, at micro boundaries
- 4) Internal multiples between macro boundaries
- 5) Internal multiples between micro boundaries
- 6) Anelastic losses

Almost every wave field extrapolation operator accounts for geometrical spreading and ignores the other effects. In this chapter I go one step further and shall focus on the second item. The effects of errors in the macro model on the P and S transmission amplitudes will also be studied. As stated in Chapter 3 it is necessary for the forward and inverse extrapolation operators derived in that chapter that the reference medium matches the true medium as close as possible (at least for the macro properties) otherwise errors are introduced that may be of influence on both the phase and the amplitude of the forward or inverse extrapolated wave field.

4.1 Error analysis

A seismic wave field that travels from the source to a reflector located in the target area will encounter several interfaces on its way down. Every time that an interface is passed the wave field will be distorted. The distortion is expressed in the amplitude of the transmitted wave field and is angle dependent. This distortion as a function of angle is called a transmission function. The reflections in the target caused by this downgoing wave field travel upward to the surface passing the same interfaces in the overburden again but now in the opposite direction. These target reflections carry important angle dependent reflectivity information with them and will also be distorted on their way to the recording surface. The task of inverse extrapolation operators is a.o. to remove the distorting *transmission* effects from the overburden, both from the illuminating (downgoing) wave field as well as from the recorded (upgoing) wave

field. These transmission effects can only be removed properly if the macro model is close to the true model. In general, the errors in the transmission functions caused by the mismatch between macro model and true model will also be angle dependent.

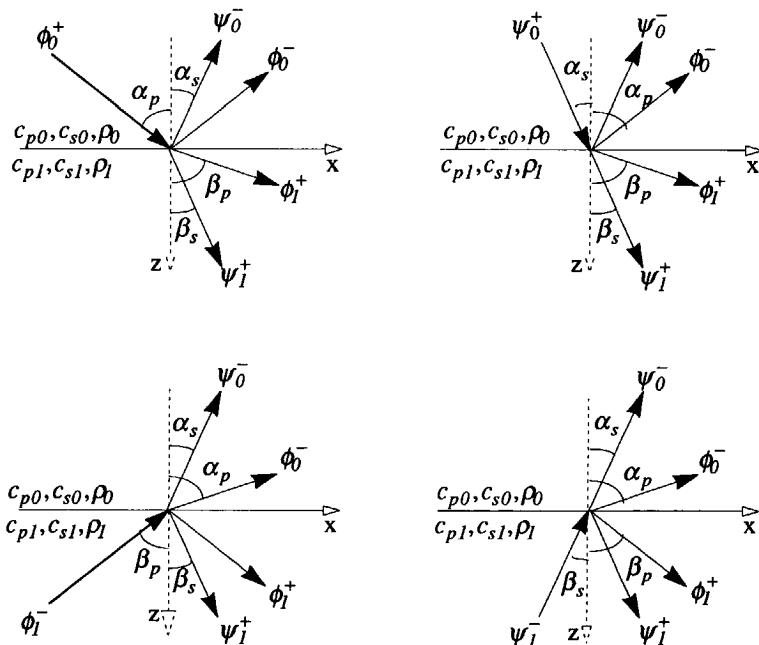
The elastic plane wave reflection and transmission coefficients at a horizontal interface between two homogeneous isotropic half spaces can be elegantly formulated in terms of a matrix notation, see Fig. 4.1 (Aki and Richards, 1980; Berkhout, 1987)

$$\underline{\underline{m}} \underline{\underline{s}} = \underline{\underline{h}} \underline{\underline{m}} \quad (4.1)$$

Fig. 4.1

Incident P and S waves on a horizontal interface.

ϕ and ψ are the P and S wave potentials as defined in Chapter 3. c_p , c_s and ρ represent the P wave velocity, the S-wave velocity and the mass density, respectively. The subscripts 0 and 1 refer to the upper and the lower half spaces, respectively. α and β correspond to the reflection and transmission angles in the upper and the lower half space respectively.



where matrix $\underline{\mathbf{m}}$ follows from the boundary conditions at the interface and is defined as

$$\underline{\mathbf{m}} = \begin{pmatrix} (1 - 2\sin^2 \alpha_s) & -(1 - 2\sin^2 \beta_s) & -2\sin \alpha_s \cos \alpha_s & -2\sin \beta_s \cos \beta_s \\ 2\frac{c_{s0}^2}{c_{p0}} \sin \alpha_p \cos \alpha_p & 2\frac{c_{s1}^2}{c_{p1}} \sin \beta_s \cos \beta_p & (1 - 2\sin^2 \alpha_s) & -(1 - 2\sin^2 \beta_s) \\ \sin \alpha_s & -\frac{\rho_0 c_{s0}}{\rho_1 c_{s1}} \sin \beta_s & \cos \alpha_s & \frac{\rho_0 c_{s0}}{\rho_1 c_{s1}} \cos \beta_s \\ \rho_1 c_{p1} \cos \alpha_p & \rho_0 c_{p0} \cos \beta_p & -\rho_1 c_{p1} \sin \alpha_p & \rho_0 c_{p0} \sin \beta_p \end{pmatrix} \quad (4.2)$$

Scattering matrix $\underline{\mathbf{s}}$ that holds all possible reflection and transmission coefficients as defined hereafter is written as

$$\underline{\mathbf{s}} = \begin{pmatrix} R_{pp}^+ & T_{pp}^- & R_{ps}^+ & T_{ps}^- \\ T_{pp}^+ & R_{pp}^- & T_{ps}^+ & R_{ps}^- \\ R_{sp}^+ & T_{sp}^- & R_{ss}^+ & T_{ss}^- \\ T_{sp}^+ & R_{sp}^- & T_{ss}^+ & R_{ss}^- \end{pmatrix} \quad (4.3)$$

and

$$\underline{\mathbf{h}} = \begin{pmatrix} -1 & 0 & 0 & 0 \\ 0 & 1 & 0 & 0 \\ 0 & 0 & -1 & 0 \\ 0 & 0 & 0 & 1 \end{pmatrix} \quad (4.4)$$

The reflection and transmission coefficients can be obtained by solving the following equation

$$\underline{s} = \underline{m}^{-1} \underline{h} \underline{m}. \quad (4.5)$$

The reflection and transmission coefficients for an incident P wave from medium 0 to medium 1 are defined as follows

$$\phi_0^- \triangleq R_{pp}^+ \phi_0^+ \quad (4.6)$$

$$\phi_1^+ \triangleq T_{pp}^+ \phi_0^+ \quad (4.7)$$

$$\psi_0^- \triangleq R_{sp}^+ \phi_0^+ \quad (4.8)$$

$$\psi_1^+ \triangleq T_{sp}^+ \phi_0^+, \quad (4.9)$$

where ϕ and ψ are the P and S wave potentials as defined in Chapter 3. (Similar relations can be given for the other coefficients.)

For the moment we will restrict the analysis for simplicity to the acoustic situation. In the acoustic situation only the four coefficients in the top-left corner of matrix \underline{s} are non-zero. Thus for this situation the matrices that appear in (4.1) reduce to

$$\underline{m} = \begin{pmatrix} I & -I \\ \rho_1 c_{p1} \cos \alpha_p & \rho_0 c_{p0} \cos \beta_p \end{pmatrix}, \quad (4.10)$$

$$\underline{\mathbf{s}} = \begin{pmatrix} R_{pp}^+ & T_{pp}^- \\ T_{pp}^+ & R_{pp}^- \end{pmatrix} \quad (4.11)$$

and

$$\underline{\mathbf{h}} = \begin{pmatrix} -1 & 0 \\ 0 & 1 \end{pmatrix}. \quad (4.12)$$

Note that in the acoustic situation the P wave potential ϕ is equal to the acoustic pressure. Solving (4.1) for the acoustic situation yields,

$$R_{pp}^+ = \frac{c_{p1}\rho_1 \cos \alpha - c_{p0}\rho_0 \cos \beta}{\text{Det}[\underline{\mathbf{m}}]}, \quad (4.13)$$

$$T_{pp}^+ = \frac{2c_{p1}\rho_1 \cos \alpha}{\text{Det}[\underline{\mathbf{m}}]}, \quad (4.14)$$

$$R_{pp}^- = \frac{c_{p0}\rho_0 \cos \beta - c_{p1}\rho_1 \cos \alpha}{\text{Det}[\underline{\mathbf{m}}]} \quad (4.15)$$

and

$$T_{pp}^- = \frac{2c_{p0}\rho_0 \cos \beta}{\text{Det}[\underline{\mathbf{m}}]} \quad (4.16)$$

where

$$\text{Det}[\underline{\mathbf{m}}] = (c_{p0}\rho_0 \cos\beta + c_{p1}\rho_1 \cos\alpha). \quad (4.17)$$

From (4.13)-(4.17) some interesting relations can be deduced that will later be extended for the elastic situation. The first relation that is particularly interesting for inverse wave field extrapolation involves the transmission and reflection coefficients related to an upgoing wave field. It can be verified with (4.13)-(4.17) that

$$T_{pp}^- T_{pp}^- \frac{c_{p1}\rho_1 \cos\alpha}{c_{p0}\rho_0 \cos\beta} + R_{pp}^- R_{pp}^- = 1 \quad (4.18)$$

or with

$$T_{pp}^- = T_{pp}^+ \frac{c_{p0}\rho_0 \cos\beta}{c_{p1}\rho_1 \cos\alpha} \quad (4.19)$$

it easily follows that

$$T_{pp}^- T_{pp}^+ + R_{pp}^- R_{pp}^- = 1 \quad (4.20)$$

holds for all angles.

The physical meaning of (4.18) and (4.20) can be explained by looking at the Rayleigh integral for inverse wave field extrapolation (for the acoustic situation) in the wavenumber domain (see also Fig 4.2). The acoustic Rayleigh integral reads (compare eq. (3.128), where in the acoustical limit both products concerning the S waves are zero; Wapenaar et al., 1989)

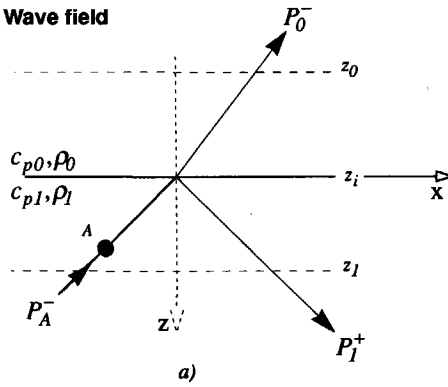
$$P_A^-(\mathbf{r}_A, \omega) = \frac{2}{\rho_0 \omega^2} \int_{-\infty}^{+\infty} \int \left[(\partial_z G_0^-)^* P_0^- \right]_{z_0} dx dy - \frac{2}{\rho_l \omega^2} \int_{-\infty}^{+\infty} \int \left[(\partial_z G_l^+)^* P_l^+ \right]_{z_l} dx dy \quad (4.21)$$

Fig. 4.2

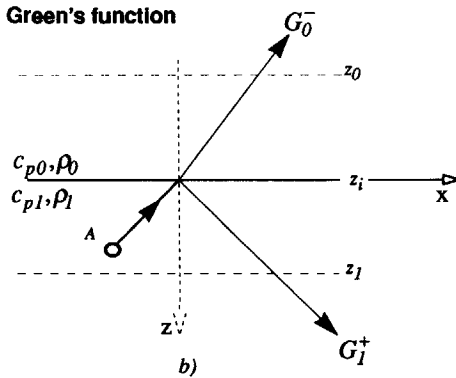
a) An upgoing P wave through A splits in an upgoing (transmitted) part through S_0 and a downgoing (reflected) part through S_l .

b) Corresponding Green's function.

Acoustic Wave field



Acoustic Green's function



where the elastic symbols Φ and Γ have been replaced according to

$$P(\mathbf{r}) = \Phi(\mathbf{r}) \quad (4.22)$$

and

$$G(\mathbf{r}, \mathbf{r}_A) = \Gamma_{\phi, \phi}(\mathbf{r}, \mathbf{r}_A) \quad (4.23)$$

where P and G represent the acoustic pressures related to the physical wave field and the acoustic Green's function respectively.

Using Parseval, (4.21) can also be written as

$$\begin{aligned} P_A^-(\mathbf{r}_A, \omega) = & \frac{2}{\rho_0 \omega^2} \left(\frac{1}{2\pi} \right)^2 \int_{-\infty}^{+\infty} \int_{-\infty}^{+\infty} \left[ik_{z_0} (\tilde{G}_0^-)^* \tilde{P}_0^- \right]_{z_0} dk_x dk_y \\ & - \frac{2}{\rho_l \omega^2} \left(\frac{1}{2\pi} \right)^2 \int_{-\infty}^{+\infty} \int_{-\infty}^{+\infty} \left[ik_{z_l} (\tilde{G}_l^+)^* \tilde{P}_l^+ \right]_{z_l} dk_x dk_y. \end{aligned} \quad (4.24)$$

In (4.24) it is assumed again that $k_z = k_z^*$ (hence, (4.24) only hold for propagating waves). In the following integral relation (4.24) will be evaluated for a simple situation. For this position vector \mathbf{r}_A is chosen to be $\mathbf{r}_A = (0, 0, z_A)$. With this choice the left hand side of (4.24) can be written as (in accordance with the Fourier integral definition used in this thesis),

$$P_A^-(\mathbf{r}_A, \omega) = \left(\frac{1}{2\pi} \right)^2 \int_{-\infty}^{+\infty} \int_{-\infty}^{+\infty} \tilde{P}_A^-(k_x, k_y, z_A; \omega) dk_x dk_y. \quad (4.25)$$

Without loss of generality, the wave field at z_A may be normalized, i.e. the wave field at z_A is chosen to be $\tilde{P}_A^-(k_x, k_y, z_A; \omega) = 1$. With this choice and dropping the integrals in (4.24) it follows that

$$I = \frac{2}{\rho_0 \omega^2} \left[ik_{z_0} (\tilde{G}_0^-)^* \tilde{P}_0^- \right]_{z_0} - \frac{2}{\rho_l \omega^2} \left[ik_{z_l} (\tilde{G}_l^+)^* \tilde{P}_l^+ \right]_{z_l}. \quad (4.26)$$

The (normalized) pressure at surface S_0 can be written as

$$\tilde{P}_0^- = e^{-ik_{z_0}|z_0-z_i|} \tilde{T}_{pp}^- e^{-ik_{z_l}|z_i-z_A|} \quad (4.27)$$

where the phase shift factors in the right hand side account for upward propagation from z_A to z_i and from z_i to z_0 . In a similar way, the (normalized) pressure at surface S_l reads

$$\tilde{P}_l^+ = e^{-ik_{z_l}|z_l-z_i|} \tilde{R}_{pp}^- e^{-ik_{z_l}|z_i-z_A|}. \quad (4.28)$$

The Green's function at S_0 , that is due to an impulsive monopole source situated in A , reads

$$\tilde{G}_0^- = \rho_l \omega^2 \frac{e^{-ik_{z_0}|z_0-z_i|} \tilde{T}_{pp}^- e^{-ik_{z_l}|z_i-z_A|}}{2ik_{z_l}}, \quad (4.29)$$

and at surface S_l

$$\tilde{G}_l^+ = \rho_l \omega^2 \frac{e^{-ik_{z_l}|z_l-z_i|} \tilde{R}_{pp}^- e^{-ik_{z_l}|z_i-z_A|}}{2ik_{z_l}}, \quad (4.30)$$

where the denominator $2ik_{z1}$, in (4.29) and (4.30) accounts for the monopole character of the Green's source. Substituting (4.27)-(4.30) into (4.26) yields

$$I = \bar{T}_{pp}^- \bar{T}_{pp}^- \frac{\rho_0 i k_{z0}}{\rho_0 i k_{z1}} + \bar{R}_{pp}^- \bar{R}_{pp}^- , \quad (4.31)$$

which is the wavenumber domain equivalent of (4.18).

On the other hand, by means of reciprocity instead of (4.29) the following Green's function (see Fig. 4.3) may be used

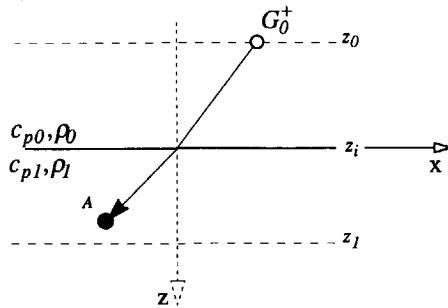
$$\tilde{G}_0^+ = \rho_0 \omega^2 \frac{e^{-ik_{z1}|z_A - z_i|} \tilde{T}_{pp}^+ e^{-ik_{z0}|z_i - z_0|}}{2ik_{z0}} . \quad (4.32)$$

Substituting this reciprocal Green's function into (4.26) together with (4.27), (4.28) and (4.30) yields

Fig. 4.3

The upgoing Green's function in (4.29) may be replaced by a downgoing Green's function on basis of reciprocity.

Reciprocal Acoustic Green's function



$$I = \tilde{T}_{pp}^+ \tilde{T}_{pp}^- + \tilde{R}_{pp}^- \tilde{R}_{pp}^- \quad (4.33)$$

which is the wavenumber domain equivalent of (4.20). Equation (4.20) (or (4.33)) are extremely suitable for error analysis. Immediately it can be seen from (4.33) that neglecting the contribution from surface S_I in (4.21) (which corresponds to the second product on the right hand side of (4.33)) means that a factor of $\tilde{R}_{pp}^- \tilde{R}_{pp}^-$ is missing in the amplitude. For the following an amplitude error function \tilde{E} will be defined, i.e.

$$\tilde{E} = 1 - \left| \tilde{T}_{pp}^+ \tilde{T}_{pp}^- \right| \quad (4.34)$$

where $\tilde{E} = \tilde{E}(k_x) \triangleq \tilde{E}(\omega p)$, and where p represents the ray parameter defined by

$$p = \frac{\sin \alpha_p}{c_{p1}} = \frac{\sin \alpha_s}{c_{s1}} = \frac{\sin \beta_p}{c_{p2}} = \frac{\sin \beta_s}{c_{s2}} = \frac{k_x}{\omega} \quad (4.35)$$

Note that \tilde{E} quantifies the angle dependent error that is made in practice when only the integral over surface S_0 in (4.21) is computed.

In Fig. 4.4 a graphical representation is given of (4.34) for three different contrasts as a function of the ray parameter. For the first contrast the first transition in the elastic model from Fig. 2.1 is chosen (the first contrast will be referred to as $g=1$, the second as $g=2$ and the third as $g=3$). Notice that the ray parameter that corresponds with an angle of emergence of 90° (i.e. $p=4400^{-1} \text{ s/m}$, $p=3600^{-1} \text{ s/m}$ and $p=2800^{-1} \text{ s/m}$ for $g=1, 2$ and 3 respectively) is different for all three contrasts as indicated in Fig. 4.4. Beyond these points the wave field becomes evanescent and is of no more interest to us. As can be seen, the error in the amplitude keeps fairly constant for a wide range of angles and grows rapidly for very high angles. Obviously, one always aims to keep the error function

Fig. 4.4

a) The transmission

product

 $\tilde{T}_{pp}^- \tilde{T}_{pp}^+$ and

b) the error function

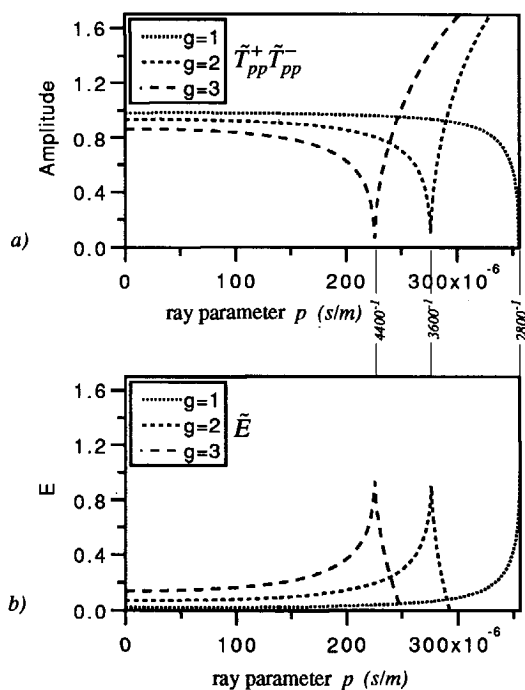
 \tilde{E}

for three different

contrasts ($g=1,2,3$)

given by the table.

		c_p	ρ
$g=1$	layer 0	2200	2000
	layer 1	2800	2100
$g=2$	layer 0	2200	2000
	layer 1	3600	2100
$g=3$	layer 0	2200	2000
	layer 1	4400	2100



as constant as possible for a wide range of angles in order to preserve angle-dependent amplitude behavior.

In a similar way elastic expressions such as acoustic expression (4.33) can be deduced from the solution of matrix equation (4.5) or equivalently from the

elastic Rayleigh integral that for the reconstruction of the upgoing P potential in point A in the subsurface reads

$$\begin{aligned}\Phi^-(\mathbf{r}_A, \omega) \approx & 2 \iint_{S_0} \frac{1}{\rho_0 \omega^2} \left[\left(\partial_z \Gamma_{\phi, \phi}^- \right)^* \Phi^- + \left(\partial_z \Gamma_{\psi, \phi}^- \right)^* \Psi^- \right] dx dy \\ & - 2 \iint_{S_I} \frac{1}{\rho_I \omega^2} \left[\left(\partial_z \Gamma_{\phi, \phi}^+ \right)^* \Phi^+ + \left(\partial_z \Gamma_{\psi, \phi}^+ \right)^* \Psi^+ \right] dx dy, \quad (4.36)\end{aligned}$$

(which follows immediately from (3.123) and (3.124)). It is shown in Appendix A that for the contributions to an upgoing P wave field in A the following relation holds

$$\tilde{T}_{pp}^+ \tilde{T}_{pp}^- + \tilde{T}_{ps}^+ \tilde{T}_{sp}^- + \tilde{R}_{pp}^- \tilde{R}_{pp}^- + \tilde{R}_{ps}^- \tilde{R}_{sp}^- = I \quad (4.37)$$

which is the more general expression of acoustic expression (4.20) (or equivalently (4.33)).

It should be emphasized though that to come to (4.37) in (4.36) the P and S potentials $(\Phi^-, \Psi^-, \Phi^+$ and $\Psi^+)$ at surfaces S_0 and S_I are wave field components (transmitted and converted) that are directly related to the upgoing P wave field through A . In addition to the acoustic expression (4.33) there are two extra products that appear in (4.37) where the converted components are involved. Notice that, in the inverse wave field operator derived in Chapter 3 (expressed by equation (3.130)) only the first product in (4.36) is taken into account (it is argued that the other terms are of second order only). From (4.37) the individual contributions of these four products can now easily be analyzed and from the following analysis it will be clear why this choice is justified. In Fig. 4.5 these four contributions are visualized for three different contrasts. Again it can be seen that the amplitude error remains constant up to high angles of emergence even in case of the highest contrast ($g=3$). As expected, the error term due to the converted waves slowly grows as the contrast grows but seems

Fig. 4.5

a)-b) The first two products from equation (4.37) for three different contrasts calculated for three contrasts given by the table.

		c_p	c_s	ρ
$g=1$	layer 0	2200	1400	2000
	layer 1	2800	1600	2100
$g=2$	layer 0	2200	1400	2000
	layer 1	3600	2057	2100
$g=3$	layer 0	2200	1400	2000
	layer 1	4400	2517	2100

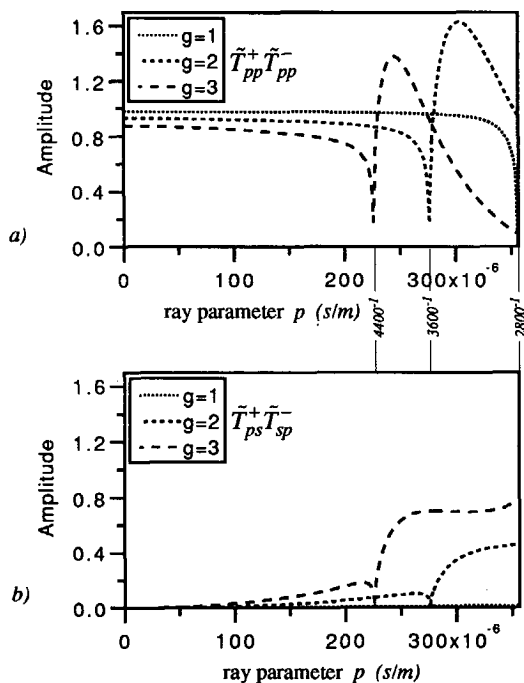


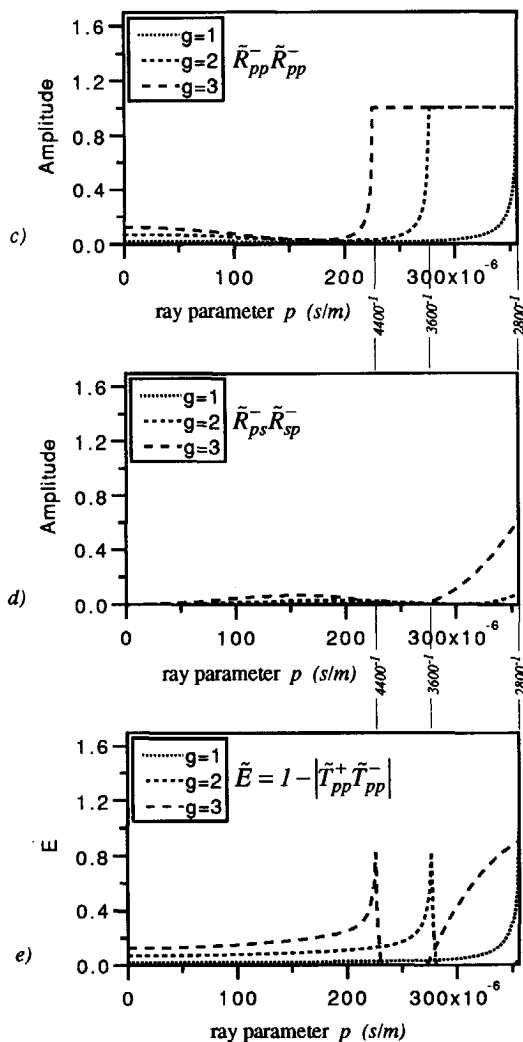
Fig. 4.5

(continued)

c)-d) The last two products from equation (4.37) for three different contrasts.

e) The error function

$\tilde{E} = 1 - |\tilde{T}_{pp}^+ \tilde{T}_{pp}^-|$
as a function of the ray parameter.



to have very little influence for the smaller angles. Notice that the first contrast ($g=1$) is closest to most seismic situations.

The elastic Rayleigh integral for an upgoing S wave through subsurface point A reads

$$\begin{aligned} \Psi_h^-(\mathbf{r}_A, \omega) \approx & 2 \iint_{S_0} \frac{1}{\rho_0 \omega^2} \left[\left(\partial_z \Gamma_{\phi, \psi_h}^- \right)^* \Phi^- + \left(\partial_z \Gamma_{\psi, \psi_h}^- \right)^* \cdot \Psi^- \right] dx dy \\ & - 2 \iint_{S_I} \frac{1}{\rho_I \omega^2} \left[\left(\partial_z \Gamma_{\phi, \psi_h}^+ \right)^* \Phi^+ + \left(\partial_z \Gamma_{\psi, \psi_h}^+ \right)^* \cdot \Psi^+ \right] dx dy. \end{aligned} \quad (4.38)$$

From this integral a similar expression can be derived

$$\tilde{T}_{sp}^+ \tilde{T}_{ps}^- + \tilde{T}_{ss}^+ \tilde{T}_{ss}^- + \tilde{R}_{sp}^- \tilde{R}_{ps}^- + \tilde{R}_{ss}^- \tilde{R}_{ss}^- = I, \quad (4.39)$$

where again the four products in this equation correspond to the four products that appear in the integrals in (4.38). Fig. 4.6 shows the individual contributions of these four terms to an upgoing S wave in A for the same contrasts as the ones given by the table in Fig. 4.5. Comparing these results and the results in Fig. 4.5 it follows that for the extrapolation of S waves the error function is not as constant as for the extrapolation of P waves for this particular example. It seems that especially for the high angles the error is no longer constant and therefore for these angles the converted term (Fig. 4.6 *b*) is no longer negligible. The irregular behavior in all the functions displayed in Fig. 4.6 is caused by the fact that the P waves in the upper and lower layer become evanescent.

4.2 Influence of macro model errors

Suppose that one chooses to extrapolate the P and S wave fields simultaneously from level z_0 to another level z_I through a horizontal interface (this can be considered equivalent to the situation where one chooses to extrapolate the total

Fig. 4.6

a)-b) The first two products from equation (4.39) calculated for three contrasts given by the table.

		c_p	c_s	ρ
$g=1$	layer 0	2200	1400	2000
	layer 1	2800	1600	2100
$g=2$	layer 0	2200	1400	2000
	layer 1	3600	2057	2100
$g=3$	layer 0	2200	1400	2000
	layer 1	4400	2517	2100

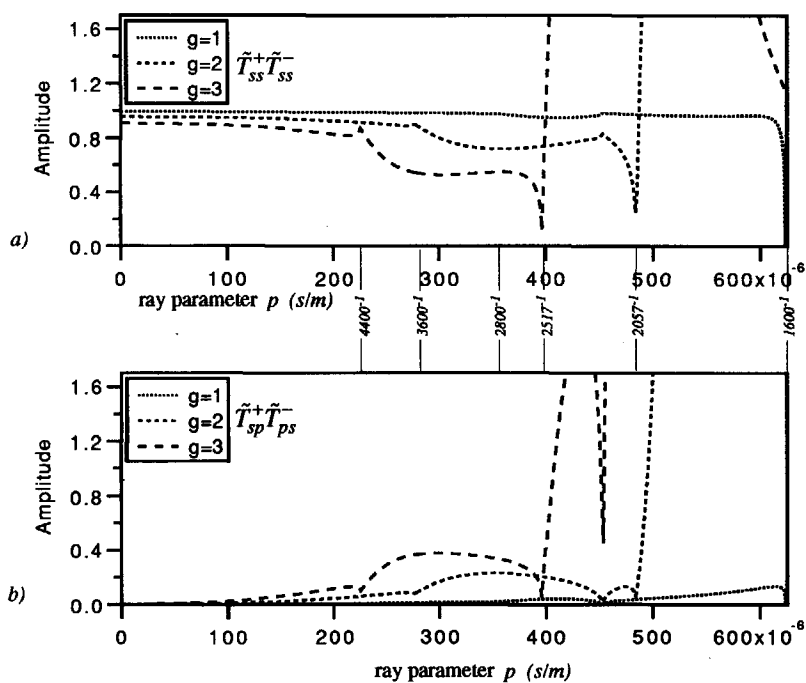
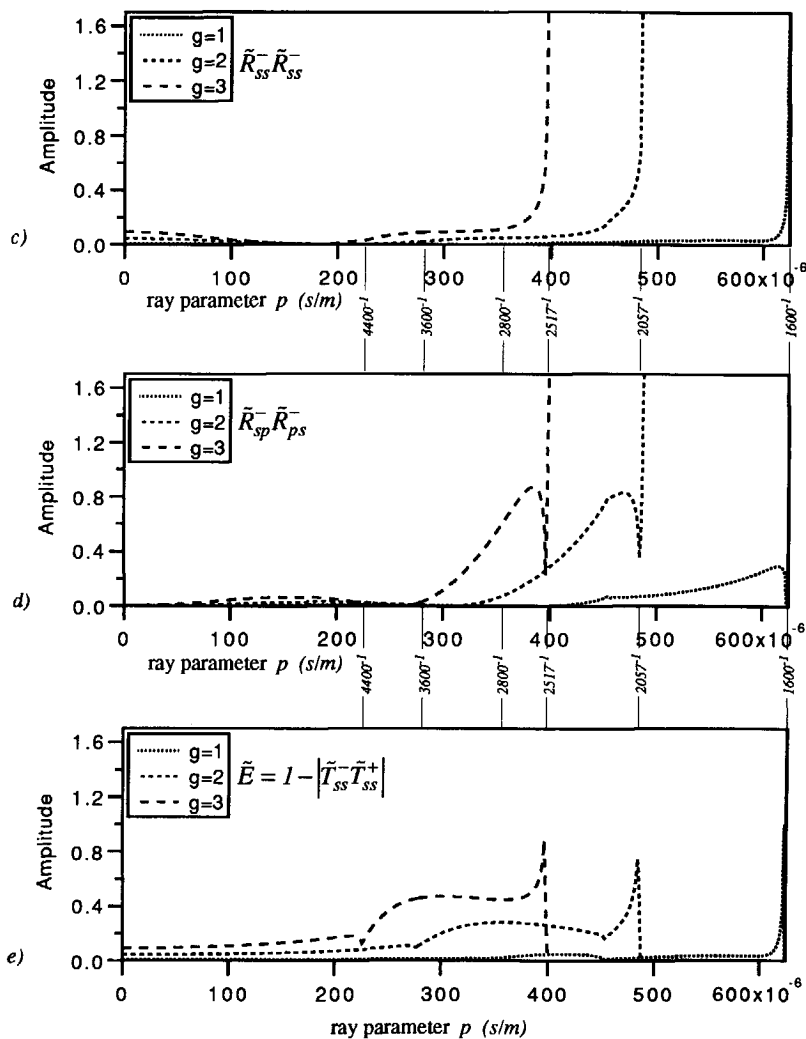


Fig. 4.6

(continued)

c)-d) The last two products from equation (4.39) for three different contrasts.

e) The error function

$$\tilde{E} = 1 - |\tilde{T}_{ss}^- \tilde{T}_{ss}^+|$$
 as a function of the ray parameter.


vector wave field in terms of particle velocities, thus without decomposition). The data is supposed to be known on level z_0 only. In the case of a correct macro model and neglecting the two reflection terms (the contribution of level z_l) relation (4.37) reduces to

$$\tilde{T}_{pp}^+ \tilde{T}_{pp}^- + \tilde{T}_{ps}^+ \tilde{T}_{sp}^- \approx 1. \quad (4.40)$$

In case of an erroneous macro model, however, for which the parameters of the first layer are chosen to be \hat{c}_{p0} , \hat{c}_{s0} and $\hat{\rho}_0$ and of the second layer these are \hat{c}_{pl} , \hat{c}_{sl} and $\hat{\rho}_l$ (the depth of the reflector is chosen equal to the one in the true model) equation (4.37) then transforms to (see Appendix A, eq.(A.21))

$$\begin{aligned} \tilde{T}_{pp}^+ \tilde{T}_{pp}^- e^{-i(k_{zp,0} - \hat{k}_{zp,0})|z_i - z_0|} e^{-i(k_{zp,l} - \hat{k}_{zp,l})|z_A - z_i|} + \\ + \tilde{T}_{ps}^+ \tilde{T}_{sp}^- e^{-i(k_{zs,0} - \hat{k}_{zs,0})|z_i - z_0|} e^{-i(k_{zp,l} - \hat{k}_{zp,l})|z_A - z_i|} \approx 1. \end{aligned} \quad (4.41)$$

An amplitude error function may now be defined according to

$$\begin{aligned} \tilde{E}_{sim} = 1 - \left| \tilde{T}_{pp}^+ \tilde{T}_{pp}^- e^{-i(k_{zp,0} - \hat{k}_{zp,0})|z_i - z_0|} e^{-i(k_{zp,l} - \hat{k}_{zp,l})|z_A - z_i|} + \right. \\ \left. \tilde{T}_{ps}^+ \tilde{T}_{sp}^- e^{-i(k_{zs,0} - \hat{k}_{zs,0})|z_i - z_0|} e^{-i(k_{zp,l} - \hat{k}_{zp,l})|z_A - z_i|} \right|, \end{aligned} \quad (4.42)$$

or

$$\tilde{E}_{sim} = 1 - \left| \tilde{T}_{pp}^+ \tilde{T}_{pp}^- e^{-i(k_{zp,0} - \hat{k}_{zp,0})|z_i - z_0|} + \tilde{T}_{ps}^+ \tilde{T}_{sp}^- e^{-i(k_{zs,0} - \hat{k}_{zs,0})|z_i - z_0|} \right|, \quad (4.43)$$

where the subscript *sim* stands for the *simultaneous* extrapolation of *P* and *S* waves. Similarly, an amplitude error function for the extrapolation of *decomposed PP* data only may be defined as (see Fig. 4.8)

$$\tilde{E}_{pp} = 1 - \left| \tilde{T}_{pp}^+ \tilde{T}_{pp}^- \right|. \quad (4.44)$$

In the following two sections error functions (4.43) and (4.44) will be used to analyze the influence of macro model errors.

4.2.1 Sensitivity

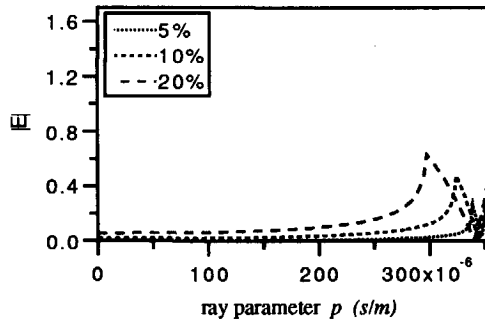
In order to study the sensitivity of amplitude errors in the transmitted wave field due to macro model errors first the situation will be considered when the extrapolation is carried out on the decomposed wave field (thus for the extrapolation of the decomposed *PP* data the error function as defined in (4.44) is considered). Wave field extrapolation operators as described in Chapter 3 aim to compensate for transmission losses. Therefore it is important to realize that the main interest is to study the effects of macro model errors on a transmitted wave field.

Fig. 4.7 shows several angle dependent error functions (eq.(4.44)) in relation to the parameters of the first interface in the Graben model. Plots are shown due to errors introduced in the *P* wave velocity of the second layer increasing from 5%, 10% and 20% respectively. Notice that in spite of the large error (20%) the error function is relatively small but what is more important is the fact that this function remains nearly flat up to high values of the ray parameter.

Fig. 4.7

The error function for increasing velocity errors. A deviation of the P wave velocity of the second layer is introduced of 5%, 10% and 20% respectively.

			c_p	c_s	ρ
	true model	layer 0	2200	1400	2000
		layer 1	2800	1600	2100
macro model 5%	5%	layer 0	2200	1400	2000
		layer 1	2960	1600	2100
macro model 10%	10%	layer 0	2200	1400	2000
		layer 1	3080	1600	2100
macro model 20%	20%	layer 0	2200	1400	2000
		layer 1	3360	1600	2100



$$\tilde{E}_{pp} = 1 - \left| \tilde{T}_{pp}^+ \tilde{T}_{pp}^- \right|$$

Normal incidence

In the following expressions will be derived that are exact for normal incidence. The reflection coefficient for normal incidence is written as

$$R = \frac{\rho_1 c_1 - \rho_0 c_0}{\rho_1 c_1 + \rho_0 c_0} \quad (4.45)$$

or equivalently

$$R = \frac{1 - A}{1 + A}, \quad (4.46)$$

where A shall be referred to as the impedance ratio defined by

$$A = \frac{\rho_0 c_0}{\rho_1 c_1}. \quad (4.47)$$

It can be easily verified that the relative error in the reflection coefficient due to a relative error in A is given by

$$\frac{\Delta R}{R} = \frac{2A}{(1 - A^2)} \frac{\Delta A}{A} \quad (4.48)$$

where

$\frac{\Delta R}{R}$ = relative error in the reflection coefficient and

$\frac{\Delta A}{A}$ = relative error in the impedance contrast.

A similar relation may be derived for the transmission coefficient which is defined as

$$T = 1 + R. \quad (4.49)$$

From (4.49) it then easily follows that

$$\frac{\Delta T}{T} = \frac{A}{(1 + A)} \frac{\Delta A}{A} \quad (4.50)$$

where

$\frac{\Delta T}{T}$ = relative error in the transmission coefficient.

For seismic applications where in general the impedance ratios lie somewhere in the vicinity of 1 it follows from (4.48) and (4.50) that the sensitivity for errors in the macro model is less strong for the transmitted wave than for the reflected wave. In fact a relation between the reflection and transmission errors can be readily obtained from (4.48) and (4.50) and reads

$$\frac{\Delta T}{T} = \frac{(I - A)}{2} \frac{\Delta R}{R}. \quad (4.51)$$

If contrasts are not too severe relations (4.48), (4.50) and (4.51) may be used as an approximation for even higher angles.

According to these formulas, if the impedance contrast for the first interface in the Graben model (Fig 2.1) is 5% then the relative reflection error (4.50) amounts to 17% while the relative transmission error amounts to only 2.1%.

4.2.2 Decomposition; before or after extrapolation?

In case of a correct macro model it makes no difference, from a mathematical point of view, whether one decomposes the data into P and S waves before extrapolation or after extrapolation, however, from (4.43) it immediately follows why in practice it should be preferably done *before* extrapolation.

Equation (4.43) shows that beside the error in amplitude there is also an error in phase for the two products that appear in this equation which is a consequence of the use of an erroneous macro model. The phase difference can easily be obtained from (4.43) and can accordingly be written as

$$-\left| \left(k_{z_{p,0}} - \hat{k}_{z_{p,0}} \right) - \left(k_{z_{s,0}} - \hat{k}_{z_{s,0}} \right) \right| z_i - z_0|. \quad (4.52)$$

In general, depending on the magnitude of the phase difference, it may be concluded that amplitude information may be lost due to possible destructive interference of these two products.

Example

For the layer parameters given in Fig. 4.8 (where only an error in the P wave velocity of the first layer is included) and choosing the distance $z_i - z_0$ equal to 160 m, it can be shown that, for a seismic wavelet with a typical central frequency of 30 Hz, $\left| \left(k_{z_{p,0}} - \hat{k}_{z_{p,0}} \right) - \left(k_{z_{s,0}} - \hat{k}_{z_{s,0}} \right) \right| |z_i - z_0| \approx \pi \text{ rad}$. The corresponding ray parameter equals $125 \cdot 10^{-6} \text{ s/m}$. Hence, for this particular example the two products will be added with a phase difference of π (for $p = 125 \cdot 10^{-6} \text{ s/m}$ and approximately π for all other values of the ray parameter), which means that there is a subtraction (destruction) rather than an addition of amplitudes. As a consequence there will be a disturbance in the amplitude behavior which could lead to errors in the lithostratigraphic inversion process. Fig. 4.8 shows the results of this particular example. First the result is shown if a correct macro model is used followed by the effects of the use of an erroneous macro model. The corresponding error functions for these two situations are included as well. Notice that the error that corresponds with the erroneous macro model (Fig. 4.8 d) is, due to the phase difference, already varying for relatively small values of the ray parameter which is of course an undesirable feature.

Decomposing the data *before* extrapolation allows separate extrapolation of the decomposed P and S data. The fact that the extrapolation is carried out separately means that after extrapolation two separate extrapolated wave fields (both originated from one and the same event) are obtained. One is now free to decide whether to add these results (with or without a residual correction) or after comparison to decide to update the macro model in case of inconsistencies (phase shifts) and extrapolate one or both wave field potentials once more in order to eliminate the phase difference.

From the results in Fig. 4.8 it may be concluded that in practice the separate result that leads to the error function expressed by (4.44) is preferred above the simultaneous result that leads to error function (4.43). Taking into account the

		c_p	c_s	ρ
true model	layer 0	2000	1000	1000
	layer 1	4000	2000	2000
macro model	layer 0	2500	1000	1000
	layer 1	4000	2000	2000

Fig. 4.8

a) The two products from equation (4.43) and after addition for a correct macro model.
 b) The error function as a function of the ray parameter.

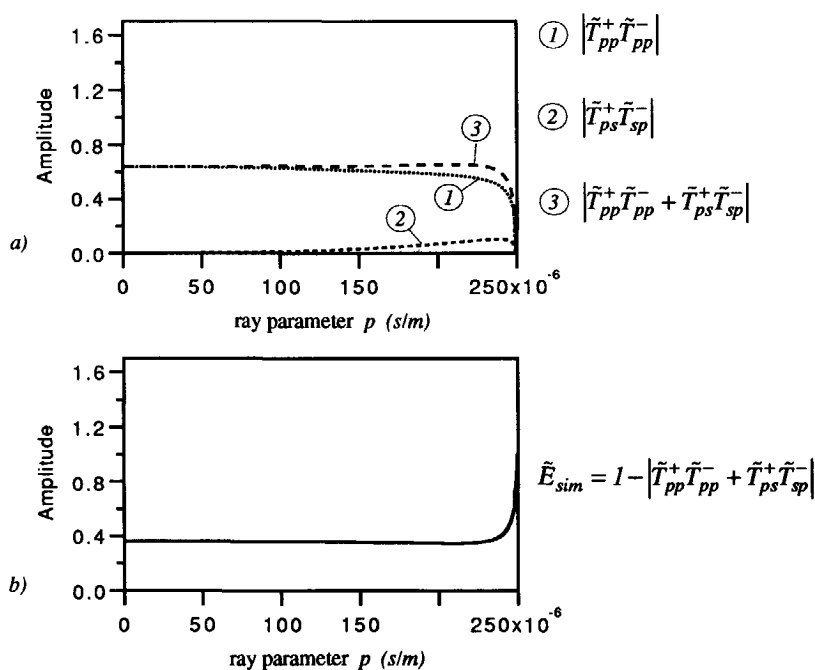
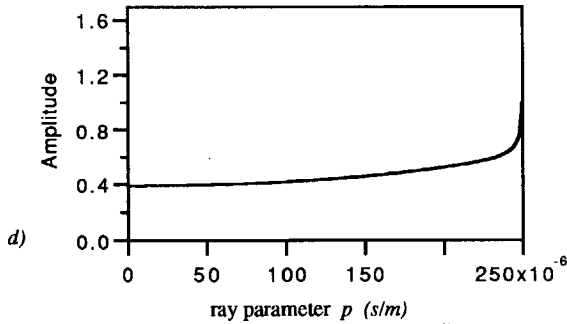
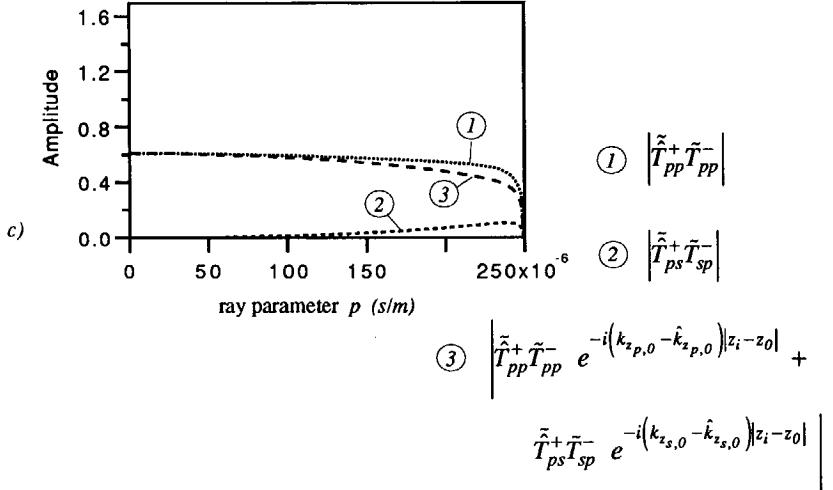


Fig. 4.8

(continued)

c) The two products from equation (4.43) and after addition for an erroneous macro model.
d) The corresponding error function as a function of the ray parameter.



$$\tilde{E}_{sim} = 1 - \left| \tilde{T}_{pp}^+ \tilde{T}_{pp}^- e^{-i(k_{zp,0} - \hat{k}_{zp,0})|z_i - z_0|} + \tilde{T}_{ps}^+ \tilde{T}_{sp}^- e^{-i(k_{zs,0} - \hat{k}_{zs,0})|z_i - z_0|} \right|$$

extra converted component is only necessary for the very high angles and can be of use in order to use the phase shift between the two results to update the macro model.

In practice often an acoustic operator is used to extrapolate the elastic reflection response. The difference between the use of an acoustic and an elastic operator for the parameters given in the previous figure is demonstrated in Fig. 4.9.

4.3 Concluding remarks

Using a perfectly known macro model, the amplitude analysis results in this chapter show that the negligence of the contribution from surface z_1 as well as the contribution of the converted term on z_0 is valid as long as the contrasts are weak. For large angles (close to critical) this approximation no longer holds. It should be emphasized though that the results presented in the various figures are all related to a particular set of parameters. Therefore equations (4.33) (acoustic relation), (4.37) (elastic P) and (4.39) (elastic S), which hold for any set of parameters, should be seen as the main result from this chapter.

In case of an erroneous macro model (which is always the case in practice) it is shown that because of inconsistent P and S macro models it is better to do the decomposition into P and S waves at the surface, thus before extrapolation. The results also show that errors in the macro model lead to relatively small amplitude errors in the extrapolated wave field (transmitted wave field) and that this error remains fairly constant for a wide range of angles. Thus the angle dependent behavior is hardly affected except for a constant factor. Finally, from the result in Fig 4.9, where (for an elastic medium) an acoustic operator is tested against an elastic operator, it can be concluded that for a wide range of angles the acoustic operator is as accurate as the elastic operator.

Fig. 4.9

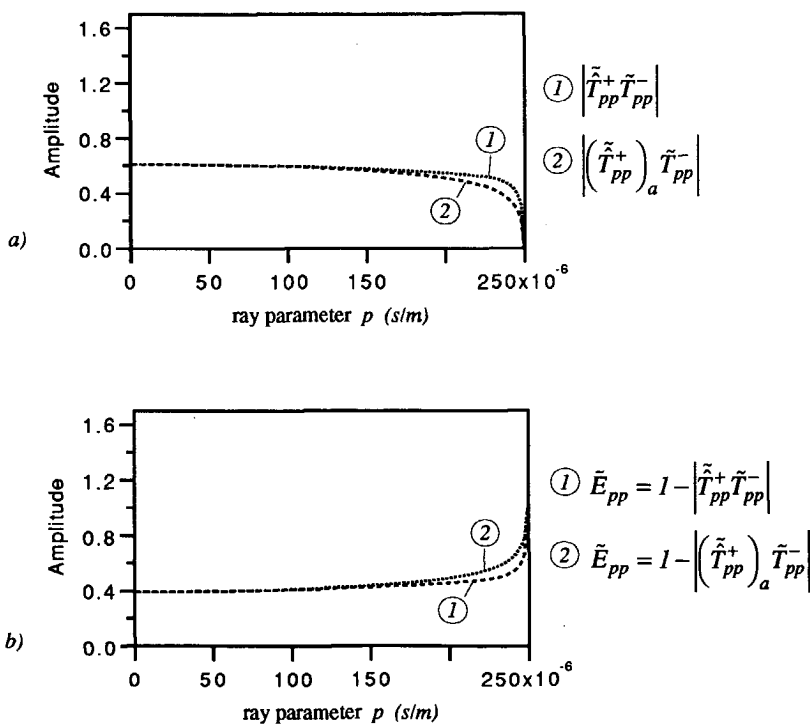
a) The difference
when using an elastic
operator

\tilde{T}_{pp}^+
and an acoustic
operator

$$\left(\tilde{T}_{pp}^+\right)_a$$

for the parameter set
given in the table.

		c_p	c_s	ρ
true model	layer 0	2000	1000	1000
	layer 1	4000	2000	2000
elastic macro model	layer 0	2500	1000	1000
	layer 1	4000	2000	2000
acoustic macro model	layer 0	2500	--	1000
	layer 1	4000	--	2000



5

Modified Rayleigh operators in redatuming and migration

The operators derived in Chapter 3 are to be used in elastic redatuming and migration schemes. In this chapter the performance of these operators will be studied on data generated for the Graben model displayed in Fig 2.1. First a description of the theory concerning redatuming and migration will be presented and it will be pointed out where these elastic operators fit into these schemes. A more detailed description concerning these subjects may be found in Berkhout, 1982 and Wapenaar and Berkhout, 1989.

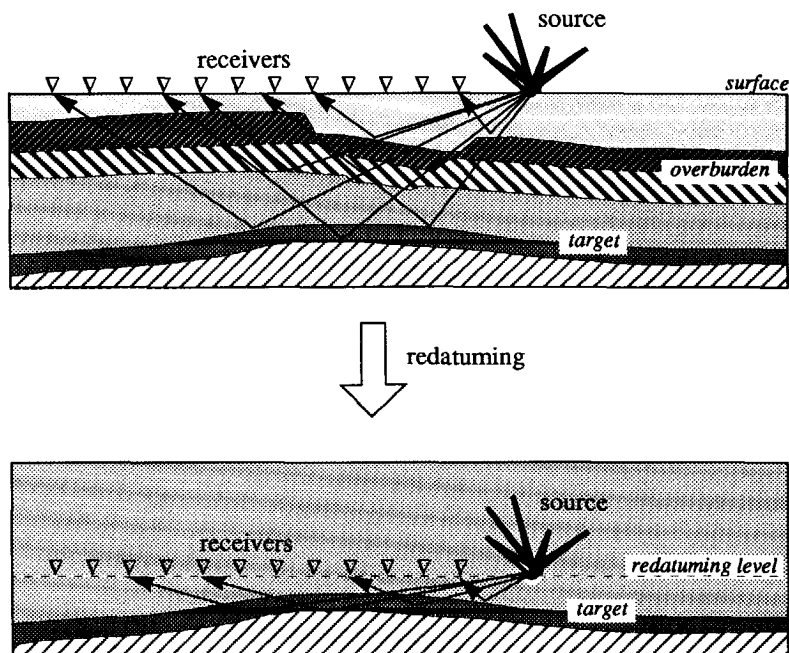
5.1 Elastic redatuming and migration

5.1.1 Principles

Moving the data to a new datum other than the surface is a process that is often referred to as redatuming. In the beginning this terminology originated from the

Fig. 5.1

Redatuming from surface acquisition to an acquisition level just above the target.



theory related to the statics correction problem. In this thesis this term will be used in a somewhat more general sense. The redatuming process that is referred to in this thesis is the mathematical process that transforms the original surface acquisition (source and receiver positions at the surface) to an acquisition at a different (often deeper) level without any loss of information (see Fig. 5.1). Obviously, this process aims to obtain 'clear' recordings just above the region of interest which enables us to do a better job in delineating the target area.

As already stated in Chapter 2 the wave field operators from Chapter 3 are applied to decomposed, multiple free elastic data. The decomposition and the surface related multiple elimination process are the two preprocessing steps in

the elastic processing scheme. The original multi-component seismic data in terms particle velocities (or equivalently in terms of displacements) due to stress sources can be organized in a matrix as follows

$$\underline{\mathbf{Y}}(z_0, z_0) = \begin{bmatrix} \underline{\mathbf{Y}}_{v_x, \tau_{xx}}(z_0, z_0) & \underline{\mathbf{Y}}_{v_x, \tau_{yz}}(z_0, z_0) & \underline{\mathbf{Y}}_{v_x, \tau_{zz}}(z_0, z_0) \\ \underline{\mathbf{Y}}_{v_y, \tau_{xx}}(z_0, z_0) & \underline{\mathbf{Y}}_{v_y, \tau_{yz}}(z_0, z_0) & \underline{\mathbf{Y}}_{v_y, \tau_{zz}}(z_0, z_0) \\ \underline{\mathbf{Y}}_{v_z, \tau_{xx}}(z_0, z_0) & \underline{\mathbf{Y}}_{v_z, \tau_{yz}}(z_0, z_0) & \underline{\mathbf{Y}}_{v_z, \tau_{zz}}(z_0, z_0) \end{bmatrix} \quad (5.1)$$

where each of the submatrices contains a monochromatic single-component multi-source multi-receiver data set. The first subscript (v_x , v_y or v_z) refers to the type of receiver and the second subscript (τ_{xx} , τ_{yz} and τ_{zz}) to the type of source. After the preprocessing this data matrix is transformed to an equivalent multi-component one-way data matrix but now the data is written in terms of received potentials (ϕ , ψ_x and ψ_y) due to potential sources (ϕ , ψ_x and ψ_y). The data resulting from the preprocessing modules at surface level z_0 may be captured in a multi-component one-way response matrix (Wapenaar and Berkhout, 1989)

$$\underline{\mathbf{X}}(z_0, z_0) = \begin{bmatrix} \underline{\mathbf{X}}_{\phi, \phi}(z_0, z_0) & \underline{\mathbf{X}}_{\phi, \psi_x}(z_0, z_0) & \underline{\mathbf{X}}_{\phi, \psi_y}(z_0, z_0) \\ \underline{\mathbf{X}}_{\psi_x, \phi}(z_0, z_0) & \underline{\mathbf{X}}_{\psi_x, \psi_x}(z_0, z_0) & \underline{\mathbf{X}}_{\psi_x, \psi_y}(z_0, z_0) \\ \underline{\mathbf{X}}_{\psi_y, \phi}(z_0, z_0) & \underline{\mathbf{X}}_{\psi_y, \psi_x}(z_0, z_0) & \underline{\mathbf{X}}_{\psi_y, \psi_y}(z_0, z_0) \end{bmatrix} \quad (5.2)$$

where again the submatrices are data matrices where each submatrix holds a multi-source multi-receiver data set for one particular potential component that is due to only one potential source type (single-component one-way response matrices). For instance, the i th column of the first submatrix $\underline{\mathbf{X}}_{\phi, \phi}(z_0, z_0)$ contains the (monochromatic) P wave recordings (indicated by the first index) due

to a P source (indicated by the second index) that is placed at the i th source position. After redatuming a similar multi-component one-way response matrix should be obtained at the redatuming level. The relation between this matrix and the one at the surface is given by

$$\underline{\mathbf{X}}(z_0, z_0) = \underline{\mathbf{W}}^-(z_0, z_A) \underline{\mathbf{X}}(z_A, z_A) \underline{\mathbf{W}}^+(z_A, z_0) + \text{'overburden response'}, \quad (5.3)$$

where z_A denotes the new redatuming level and matrices $\underline{\mathbf{W}}^-$ and $\underline{\mathbf{W}}^+$ are propagation matrices that describe upward and downward propagation through the overburden respectively. They are based on the modified Rayleigh integrals derived in Chapter 3. The overburden response are all the reflections caused by the inhomogeneities in the overburden and have no relation whatsoever to the target reflections which are of course our main interest. These overburden reflections, however, form the main ingredient for a macro model estimation procedure. For the elastic situation both a P and an S macro model has to be estimated. Propagation operators $\underline{\mathbf{W}}^-$ and $\underline{\mathbf{W}}^+$ are then calculated using the estimated macro model. In order to obtain the response at redatuming level these operators should be inverted and be applied to the left hand side and to the right hand side of equation (5.3) after moving the 'overburden response' to the left hand side first, such that this equation now becomes

$$\begin{aligned} \underline{\mathbf{X}}(z_A, z_A) = \\ \left[\underline{\mathbf{W}}^-(z_0, z_A) \right]^{-1} \left(\underline{\mathbf{X}}(z_0, z_0) - \text{'overburden response'} \right) \left[\underline{\mathbf{W}}^+(z_A, z_0) \right]^{-1} \end{aligned} \quad (5.4)$$

or

$$\begin{aligned} \underline{\mathbf{X}}(z_A, z_A) = & \left[\underline{\mathbf{W}}^-(z_0, z_A) \right]^{-I} \underline{\mathbf{X}}(z_0, z_0) \left[\underline{\mathbf{W}}^+(z_A, z_0) \right]^{-I} + \\ & - \left[\underline{\mathbf{W}}^-(z_0, z_A) \right]^{-I} (\text{'overburden response'}) \left[\underline{\mathbf{W}}^+(z_A, z_0) \right]^{-I}. \end{aligned} \quad (5.5)$$

After transforming the results to the time domain, the second part on the right hand side of (5.5) concerning the 'overburden response' will appear at negative times and will not seriously interfere with the target response. In the remainder of this chapter I shall no longer pay any attention to the overburden response and shall concentrate only on the target response and on the way this response is handled by the wave field operators. Hence, the multi-component one-way target response matrix at the new datum may be written as

$$\underline{\mathbf{X}}(z_A, z_A) = \underline{\mathbf{F}}^-(z_A, z_0) \underline{\mathbf{X}}(z_0, z_0) \underline{\mathbf{F}}^+(z_0, z_A), \quad (5.6)$$

where

$$\underline{\mathbf{F}}^-(z_A, z_0) = \left[\underline{\mathbf{W}}^-(z_0, z_A) \right]^{-I} \quad (5.7)$$

and

$$\underline{\mathbf{F}}^+(z_0, z_A) = \left[\underline{\mathbf{W}}^+(z_A, z_0) \right]^{-I}. \quad (5.8)$$

In Chapter 3 it is already argued that during propagation converted waves may be neglected for a wide range of angles. For the first submatrix in the multi-component target response matrix $\underline{\mathbf{X}}(z_A, z_A)$ from (5.6) the following may then be written

$$\underline{\underline{X}}_{\phi,\phi}(z_A, z_A) \approx \underline{\underline{F}}_{\phi,\phi}^-(z_A, z_0) \underline{\underline{X}}_{\phi,\phi}(z_0, z_0) \underline{\underline{F}}_{\phi,\phi}^+(z_0, z_A) \quad (5.9)$$

or using a more general notation that includes all other submatrices of matrix $\underline{\underline{X}}(z_A, z_A)$ as well

$$\underline{\underline{X}}_{\Omega_2, \Omega_l}(z_A, z_A) \approx \underline{\underline{F}}_{\Omega_2, \Omega_2}^-(z_A, z_0) \underline{\underline{X}}_{\Omega_2, \Omega_l}(z_0, z_0) \underline{\underline{F}}_{\Omega_l, \Omega_l}^+(z_0, z_A) \quad (5.10)$$

where Ω_l and Ω_2 stand for ϕ or ψ_x or ψ_y and where

$$\underline{\underline{F}}_{\Omega_2, \Omega_2}^-(z_A, z_0) = \left[\underline{\underline{W}}_{\Omega_2, \Omega_2}^-(z_0, z_A) \right]^{-I} \quad (5.11)$$

and

$$\underline{\underline{F}}_{\Omega_l, \Omega_l}^+(z_0, z_A) = \left[\underline{\underline{W}}_{\Omega_l, \Omega_l}^+(z_A, z_0) \right]^{-I}. \quad (5.12)$$

Note that conversion during reflection is still included in the matrices in (5.10). Assuming that the contrasts in the subsurface are weak to moderate, which is a valid assumption in the seismic situation, then in analogy with Chapter 3 for the forward and the inverse operators the modified matched inverse operators may be used, i.e.

$$\underline{\underline{F}}_{\Omega_2, \Omega_2}^-(z_A, z_0) = \left[\underline{\underline{W}}_{\Omega_2, \Omega_2}^+(z_A, z_0) \right]^* \quad (5.13)$$

and

$$\underline{\mathbf{F}}_{\Omega_l, \Omega_l}^+(z_0, z_A) = \left[\underline{\mathbf{W}}_{\Omega_l, \Omega_l}^-(z_0, z_A) \right]^* \quad (5.14)$$

where $*$ denotes complex conjugation. Notice that each row of propagation operator $\underline{\mathbf{W}}_{\Omega_l, \Omega_l}^+(z_A, z_0)$ corresponds to the z -derivative of the complex conjugated Green's function that is derived in Chapter 3 (compare (3.130) or (3.132)). In fact, using the first submatrix as an example (eq. (5.9)), by applying the first inverse operator to the surface response only, it follows that

$$\underline{\mathbf{X}}_{\phi, \phi}(z_A, z_0) = \underline{\mathbf{F}}_{\phi, \phi}^-(z_A, z_0) \underline{\mathbf{X}}_{\phi, \phi}(z_0, z_0) \quad (5.15)$$

or, with (5.13), that

$$\underline{\mathbf{X}}_{\phi, \phi}(z_A, z_0) = \left[\underline{\mathbf{W}}_{\phi, \phi}^+(z_A, z_0) \right]^* \underline{\mathbf{X}}_{\phi, \phi}(z_0, z_0). \quad (5.16)$$

Note that (5.16) is merely a matrix notation for the integral operator (3.130) that is derived in Chapter 3 (at least for a finite aperture). This first step is the process that downward extrapolates the receivers to level z_A . Thus $\underline{\mathbf{X}}_{\phi, \phi}(z_A, z_0)$ represents the one-way target response at level z_A due to sources at level z_0 . The next step is to apply (5.14) to (5.16) which is actually the process that downward extrapolates the sources to level z_A , i.e.

$$\underline{\mathbf{X}}_{\phi, \phi}(z_A, z_A) = \underline{\mathbf{X}}_{\phi, \phi}(z_A, z_0) \underline{\mathbf{F}}_{\phi, \phi}^+(z_0, z_A) \quad (5.17)$$

or with (5.14)

$$\underline{X}_{\phi,\phi}(z_A, z_A) = \underline{X}_{\phi,\phi}(z_A, z_0) \left[\underline{W}_{\phi,\phi}^-(z_0, z_A) \right]^* \quad (5.18)$$

It should be emphasized that the quality of the redatuming process depends on 1) the accuracy with which one is able to estimate the macro model (P and S velocity models) and 2) the way the Green's function is generated with the use of this macro model. Often in the seismic industry the Green's function is calculated using a ray-tracing algorithm. In this thesis the Green's function is calculated using a full elastic finite difference algorithm (see Appendix B). In such an algorithm all wave types are included (reflections, transmissions, wave conversions, diffractions, headwaves, surface waves, interface waves).

Redatuming of PP data

In order to redatum the $8I$ ($=NS$) decomposed data sets from the Graben model, 256 ($=NGSr$) Green's functions are calculated using the correct macro model (so the macro model matches the overburden exactly, see also Fig. 5.2). After a Fourier transform, the z -derivatives of these Green's functions form the rows of the propagation matrix in (5.13). Another $8I$ ($=NGSs$) Green's functions need to be generated (either by modeling or by applying the reciprocity principle), again using the correct macro model, in order to downward continue the $8I$ sources. After a Fourier transform, the z -derivatives of these $8I$ Green's functions form the rows of the propagation matrix in (5.14) (see Fig. 5.3 where this redatuming process is visualized using the decomposed PP data). For the Green's functions a P wave source is used and at the receiver side the response is decomposed into one-way P and S responses. Thus, similarly as to the seismic data the Green's functions are decomposed at the source side and at the receiver side. The seismic wavelet and the source signature of the Green's function are displayed in Fig. 5.4. Of course one expects a delta pulse for the Green's function but this is not necessary. A sufficient condition is that the spectrum of the Green's source is unity within the seismic bandwidth (compare

Fig. 5.2

Configurations used to calculate the inverse and forward operators.

a) Green's functions to bring down the 256 receivers.
b) Green's functions to bring down the 81 sources.

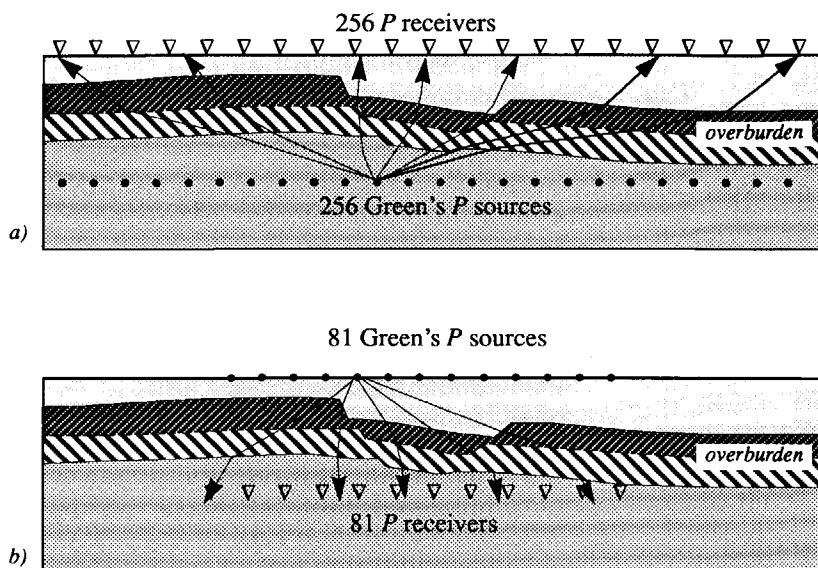


Fig. 5.4 *b* and *d*). In Fig. 5.5 one of the 81 redatumed *PP* data sets can be observed. The first data set, Fig. 5.5 *a*, corresponds to the *PP* target response after this has been isolated from the rest of the surface *PP* data (see Fig. 2.9 *a*). The maximum angle from the target that is recorded at the far sides of the receiver array is about 70° . Fig. 5.5 *b* shows the redatumed *PP* data after the complete redatuming procedure where source and receivers are at one and the same level, $z_A = 300 \text{ m}$ (eq. (5.18)). The arrows indicate how angles in the surface data map to angles in the redatumed data. Of course, we may expect accurate wave field reconstruction only between the (approximate) bounds of -70° and $+70^\circ$ degrees. In the following this range shall be referred to as the 'expected aperture' (see Fig. 5.6). This aperture is calculated for the first interface (layer#3 to layer#4) in the target. For deeper interfaces another aperture (often wider) is applicable. (It should be emphasized though that the indicated

Fig. 5.3

Inverse and forward operators applied to the PP data from the Graben model.

NR=number of receivers

NS=number of sources

NT=number of time samples

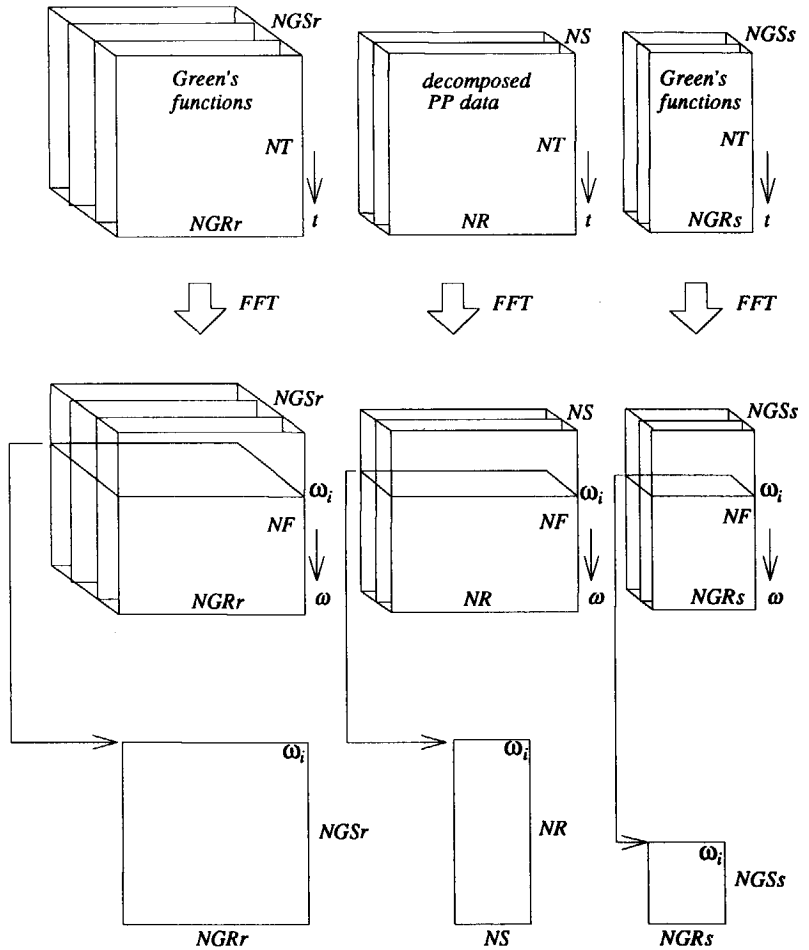
NF=number of frequencies

NGSr=number of Green's sources to bring down the receivers

NGRr(=NR)=number of Green's receivers to bring down the receivers

NGSs(=NS)=number of Green's sources to bring down the sources

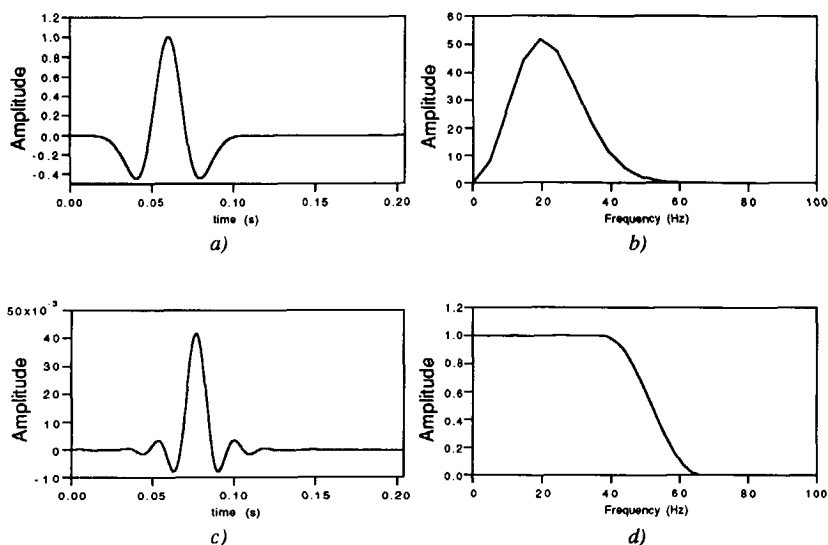
NGRs=number of Green's receivers to bring down the sources.



$$X_{\phi,\phi}(z_A, z_A) = F_{\phi,\phi}^-(z_A, z_0) \times X_{\phi,\phi}(z_0, z_0) \times F_{\phi,\phi}^+(z_0, z_A)$$

Fig. 5.4

a) Seismic wavelet.
b) Spectrum of the seismic wavelet.
c) Green's source wavelet.
d) Spectrum of the Green's source wavelet.



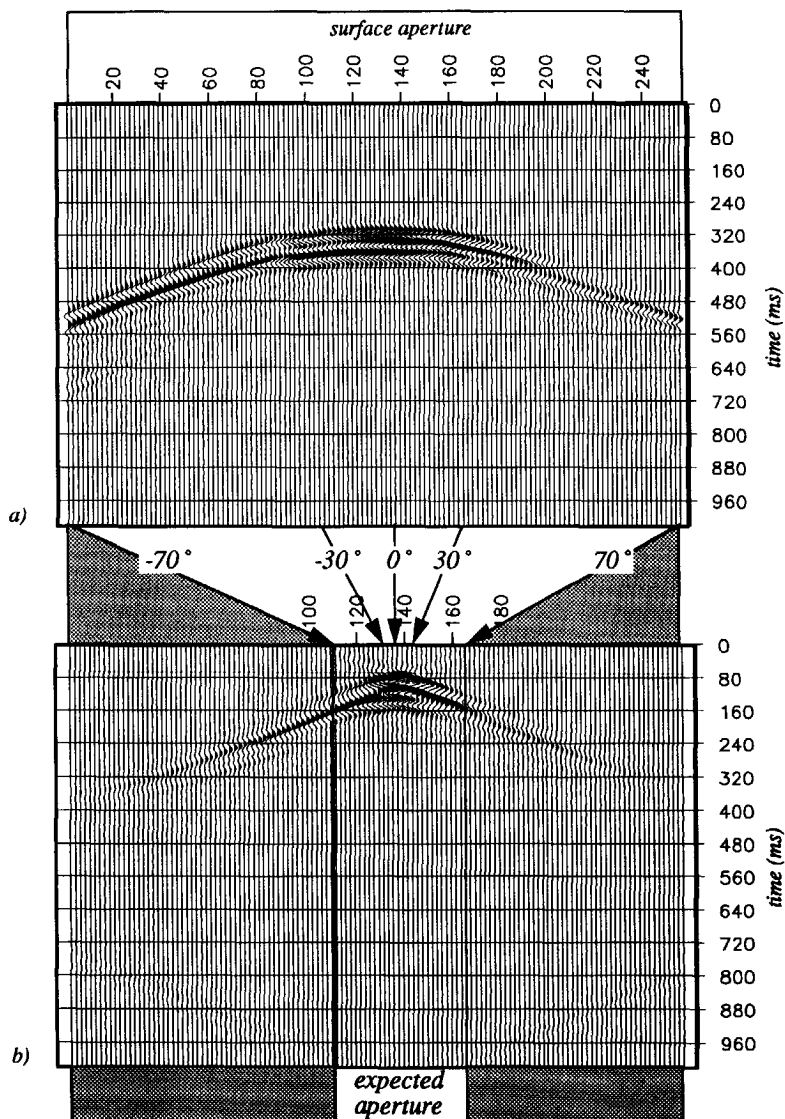
bounds of -70 to $+70$ degrees are not stringent..) For comparison, a data set for exactly the same source position as the redatumed source position has been simulated at $z_A=300$ m and this simulated data set is displayed in Fig. 5.5 c. The first thing that can be noticed is that, due to the finite aperture at the surface, the aperture at the redatuming level has reduced considerably. This does *not* mean however that the range of angles has been reduced in comparison to the range of angles that was available in the surface data. Although the aperture at the redatuming level is smaller it is still expected that true amplitudes can be reconstructed for a wide range of angles because the redatuming level is very close to the target zone (the distance between the redatuming level and the top of the target amounts to only 40 m!). Notice in Fig. 5.5 b and c, that the angle changes rapidly as a function of offset because of the small distance). Taking a closer look at the redatumed data it can also be observed that toward the edges of the expected aperture there is a decrease of the amplitude. This amplitude decay can be explained by the presence of artifacts. These artifacts are due to

Fig. 5.5

a) Isolated PP target response at the surface.

b) Redatumed PP target response (source position $x=1112$ m, source #41). Source and receiver at $z=300$ m.

c) For comparison. Simulated PP data. Source and receivers at $z=300$ m. Notice that, the redatumed data (b) is supposed to match the simulated data only within the window of the expected aperture. Outside this aperture (shaded area) the data are out of range of the surface aperture so it is not possible to reconstruct the wave field for this area.



the truncation of the data and the operators at the surface. One way to suppress these artifacts, at least for the smaller offsets, is by tapering the data (or the operators) at the sides. This, however, will *not* restore the amplitudes at the edges of the aperture (a more accurate way to reduce aperture artifacts, based on diffraction theory, is presently under investigation). To obtain the result in Fig. 5.5 *b* and later on in Fig. 5.9 *b* no taper was used. One can observe some tails of the artifacts just above the hyperbolas. In Fig. 5.7*a* the zero-offset traces (for source #41 this corresponds to receiver #137) of the redatumed *PP* data and the simulated *PP* data are plotted and in Fig. 5.7*b* their spectra are compared. Note that the match is very good. Selecting the zero-offset traces from all the 81 redatumed data sets yields a zero-offset data set at level

Fig. 5.5
(continued).

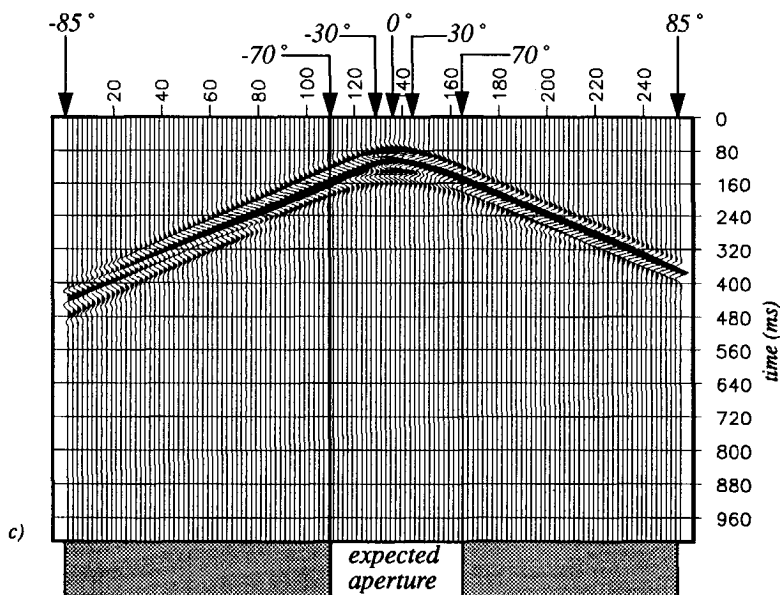


Fig. 5.6

Surface aperture and the aperture after redatuming. Notice that, although the expected aperture is smaller it still covers the same range of angles that was already present at the surface.

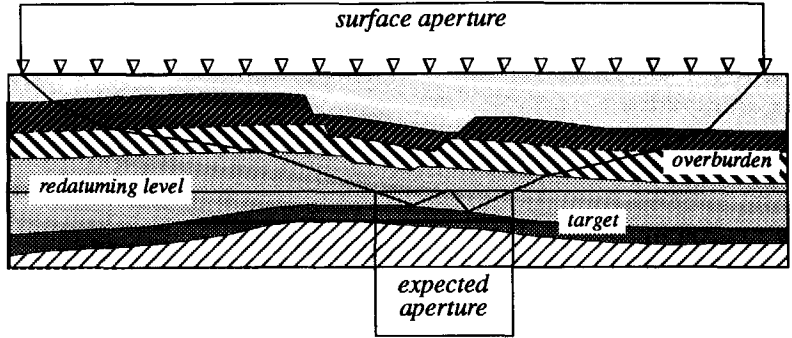


Fig. 5.7

a) Comparison of the zero-offset traces of the redatumed PP data and the simulated PP data.
b) Comparison of the spectra.

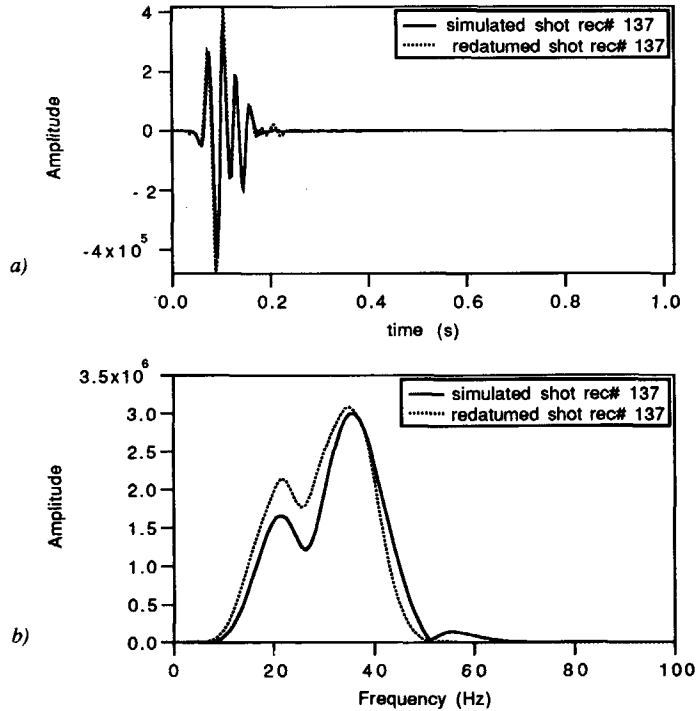
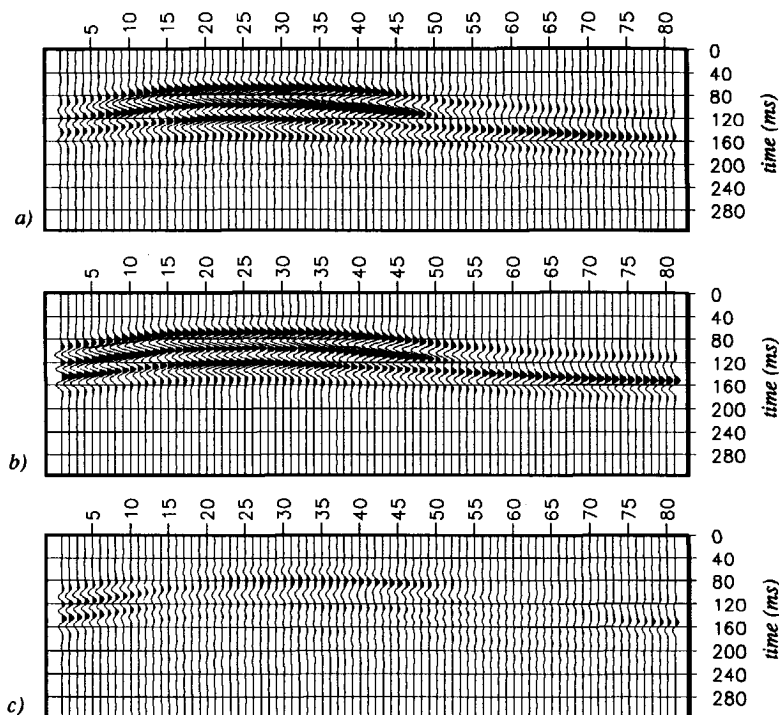


Fig. 5.8

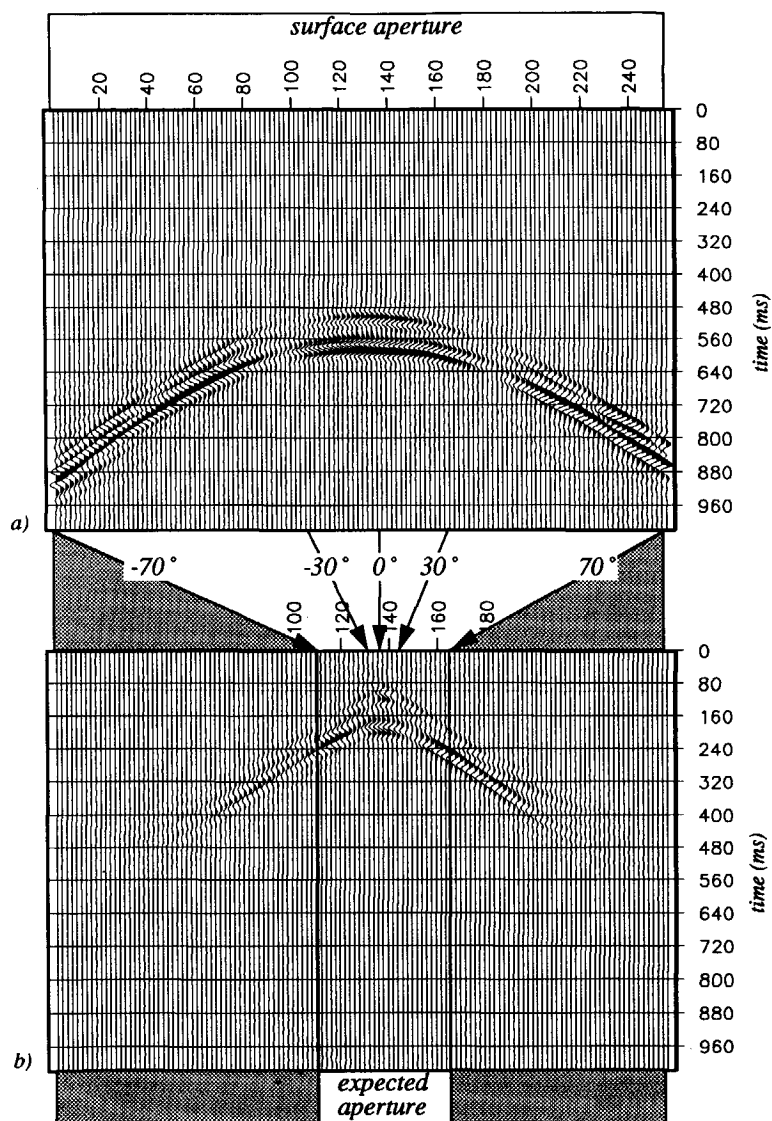
Comparison between
 a) the redatumed
 zero-offset PP data
 and
 b) the simulated
 zero-offset PP data.
 c) Residual section.
 Notice that in these
 pictures both axes
 have been scaled
 compared to previ-
 ous data displays



$z=300$ m. A comparison between this data set and the simulated zero-offset data at $z=300$ m can be seen in Fig. 5.8. The trace shown in Fig. 5.7 corresponds to trace 41 (source#41) in Fig. 5.8. Note that the match is very good.

Fig. 5.9

a) Isolated SS target response at the surface.
 b) Redatumed SS target response (source position $x=1112$ m, source #41). Source and receiver at $z=300$ m.
 c) For comparison. Simulated SS data. Source and receivers at $z=300$ m. Again, similarly as in the PP example, the redatumed SS data (b) is supposed to match the simulated data within the range of the indicated expected aperture.



Redatuming of SS data

To extrapolate the SS data now instead of P sources, SV sources have to be used for the calculation of the Green's functions. The configurations for these SV Green's functions remain exactly the same as the one displayed in Fig. 5.2. So, in this figure P has to be replaced by SV . Similarly as in the case of redatuming the PP data, Fig. 5.9 *a* shows the (isolated) SS target response at the surface (compare Fig. 2.9 *c*), the redatumed SS data and for comparison the simulated SS data at the redatuming level, respectively. (The displayed angles in this figure are approximations and may differ a few degrees compared to the angles in Fig. 5.5.) Again, as can be observed there is a good match within the aperture bounds. The expected apertures as indicated in Fig. 5.5 and Fig. 5.9 are calculated for the first transition in the target area (i.e. from layer #3 to layer #4). For a deeper transition the expected apertures are supposed to be wider, although the range of angles will, in general, decrease compared to a shallower interface.

Fig. 5.9
(continued)

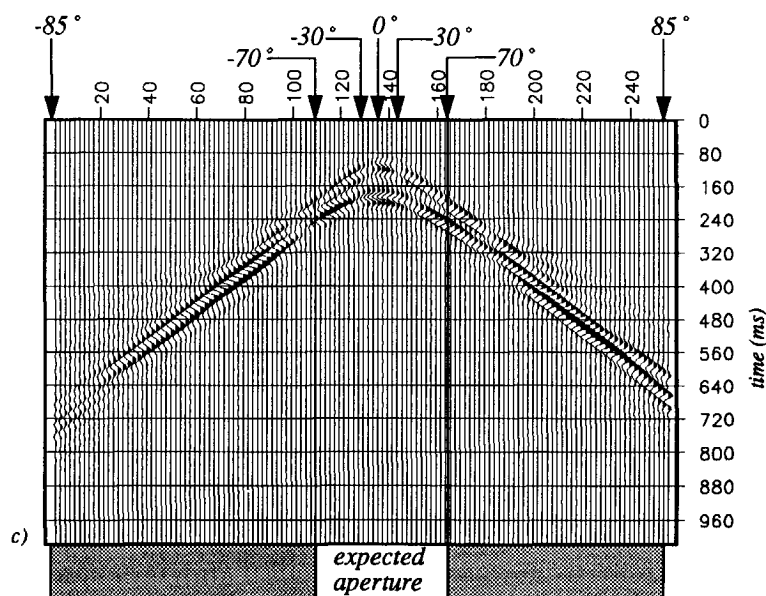
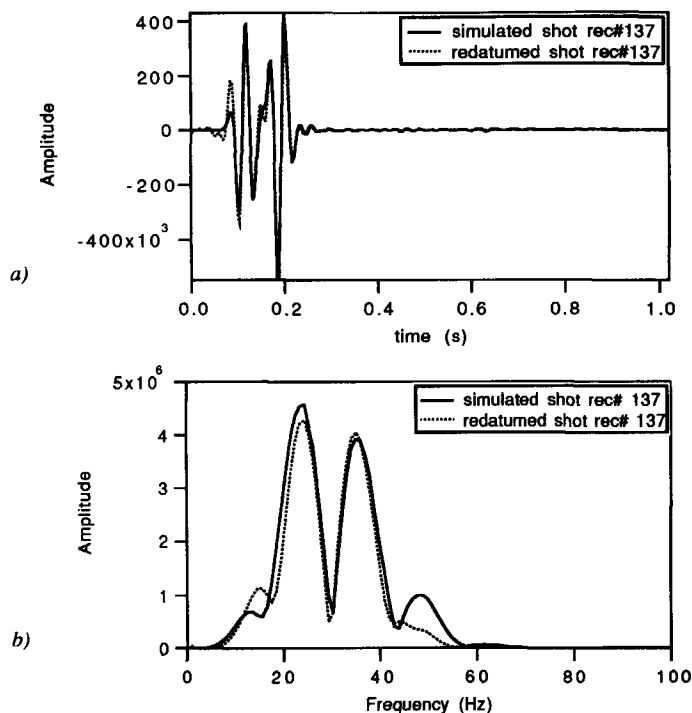


Fig. 5.10

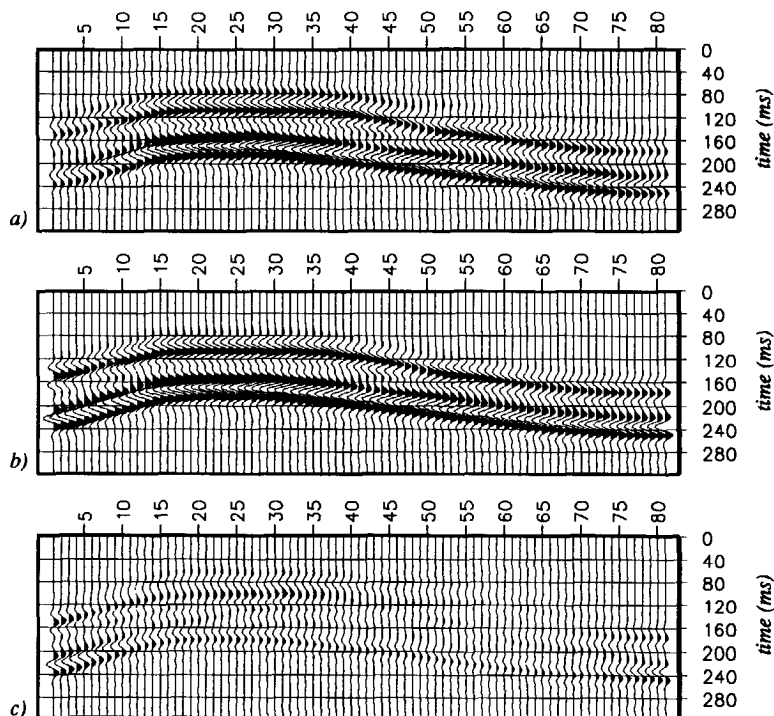
a) Comparison of the zero-offset traces of the redatumed PP data and the simulated PP data.
b) Comparison of the spectra.



In Fig. 5.9 *b* it can be clearly seen that for the first (weaker) event the corresponding aperture (as indicated) is smaller than for the second (strong) event, which corresponds to the transition from layer#6 to layer#7. For the second event the amplitudes are still strongly present even outside the expected aperture, suggesting that for this second event another aperture (wider) should be applied. In Fig. 5.10 *a* the zero-offset traces of the redatumed SS data and the simulated SS data are plotted and in Fig. 5.10 *b* their spectra are compared. A comparison between the zero-offset SS data set and the simulated zero-offset SS data at $z=300$ m can be observed in Fig. 5.11. Again, as can be observed, the match is very good.

Fig. 5.11

Comparison between
*a) the redatumed
 zero-offset SS data
 and
 b) the simulated
 zero-offset SS data.
 c) Residual section.*



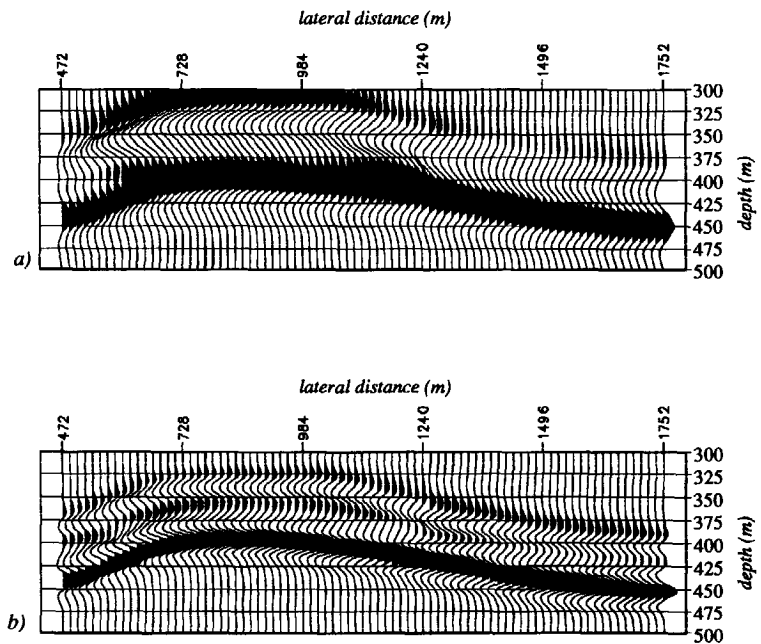
5.1.2 Imaging condition

The final goal of the extrapolation process is to obtain an image (x, z) of the Earth's interior. This image should then reveal the true layer structure. One possibility to reveal the layer structure is to redatum to several levels in the region of interest and then to pick the $t=0$ component at the zero offset from each redatumed data set. These $t=0$ components are then stored in a (x, z) image at the corresponding redatumed source position. In this way one builds up a genuine zero-offset image of the target zone. In this image the zero offset

reflection coefficients are available for every point in the target and can be used to estimate the impedances.

From the redatumed *PP* and *SS* data migrated *PP* and *SS* sections are obtained which can be observed in Fig. 5.12*a* and *b* respectively. Obviously, due to the lower shear wave velocity (shorter wavelength), the migrated *SS* section has a higher resolution than the migrated *PP* section. The redatumed *PP* data have been migrated with a constant velocity that corresponds with the compressional wave velocity at the redatuming level (layer #3), i.e. $c_p = 3100$ m/s. Similarly, the redatumed *SS* data have been migrated using a constant velocity that corre-

Fig. 5.12
a) Migrated *PP* data
 for the target area.
b) Migrated *SS* data
 for the target area.



sponds with the shear wave velocity at the redatuming level, i.e. $c_s = 1700$ m/s. Due to the relatively long wavelength and the thin layering there is a strong interference of the different reflectors as can be seen in both migrated sections. Notice that in these sections only the zero-offset reflectivity is available and therefore one can invert for impedances only.

To be able to invert for the elastic parameters (c_p , c_s and the density) we go one step backward and examine the redatumed data more closely (e.g. Fig. 5.5 *b* and Fig. 5.9 *b*). Then, it can be shown that angle dependent reflection information is available in each of these data sets. By performing a generalized imaging procedure it is possible to obtain from each redatumed data set angle dependent reflection information for each depth point (a detailed description on the concept of generalized imaging and the retrieval of angle-dependent reflectivity would lead us beyond the scope of this thesis. The interested reader is referred to de Bruin, 1988 and 1992). Thus, instead of having a scalar (*zero-offset reflectivity* $R(0)$) per depth point it is possible to have a vector (*angle-dependent reflectivity* $R(\alpha)$) per depth point. Obviously, the range of angles that can be retrieved fully depends on the range of angles available in the surface data which, of course, on its turn depends on the acquisition geometry of the seismic survey.

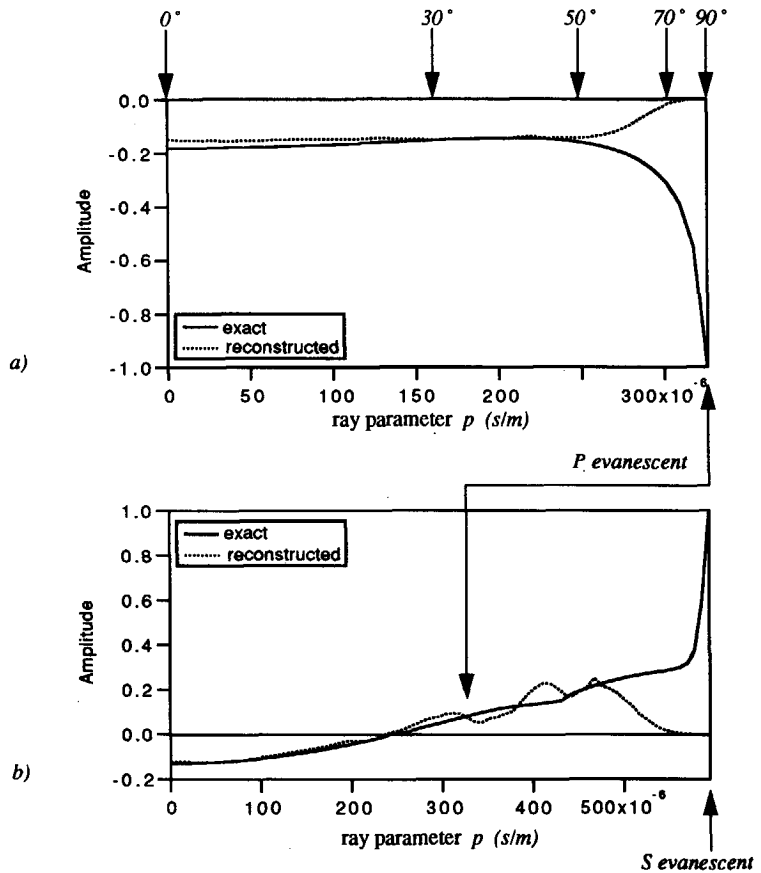
For the shale-gas transition on top of the reservoir (from layer #3 to layer #4) the amplitude behavior as a function of the ray parameter p has been reconstructed for one x location. For the *PP* data this behavior is displayed in Fig. 5.13 *a* and for the *SS* data this is displayed in Fig. 5.13 *b*. Notice that, in Fig. 5.13 *a* the maximum ray parameter corresponds to the critical angle belonging to the *P* wave velocity ($p=1/3100 \approx 323 \cdot 10^{-6}$ s/m), whereas in Fig. 5.13 *b* the maximum value corresponds to the *S* wave velocity ($p=1/1700 \approx 588 \cdot 10^{-6}$ s/m). It can be observed in Fig. 5.13 *b* that the match in the *SS* data deteriorates at the point where the *P* wave becomes evanescent as was expected according to the results achieved in Chapter 4.

Fig. 5.13

a) PP amplitudes as function of the ray parameter for the shale-gas transition on top of the reservoir (layer #3 to layer #4).

b) SS amplitudes as function of the ray parameter for the shale-gas transition on top of the reservoir (layer #3 to layer #4).

On top of the first picture the corresponding angles are indicated.



5.2 Conclusions

The redatuming results shown in Fig. 5.5 (PP data) and Fig. 5.9 (SS data) illustrate that the amplitude handling of the P and S extrapolation operators ((3.130) and (3.132) respectively) is as we expected good, at least for not too large offsets. For larger offsets the example clearly illustrates the effect of truncation

(finite aperture) when applying these P and S extrapolation operators, where it is assumed that the data is collected over a range from $-\infty$ to $+\infty$. Truncation artifacts mainly affect amplitudes that are close to the edge of the aperture. Although the recovered aperture at the redatuming level is small (because this is very close to the target) the results in Fig. 5.13 *a* and *b* show that the reconstructed angle dependent P and S reflection curves match the true curves very well for a wide range of angles. As expected from the results in Chapter 4 the match in case of the SS data (Fig. 5.13 *b*) deteriorates after the p -value where the P wave becomes evanescent (i.e. $p=1/3100 \approx 323.10^{-6}$ s/m). Also in both figures it can be seen that at about 50 degrees and higher the amplitude decays considerably which is, as stated before, the effect of truncation.

Appendix A

Elastic Rayleigh integral contributions

Although it can be verified from the solution of (4.5) that elastic equations (4.37) and (4.39) are true, for the proof that these equations are indeed correct we shall start in this Appendix from the modified Rayleigh integrals that are derived in Chapter 3. In this Chapter 3 we showed that for the reconstruction of the upgoing P potential in point A in the subsurface the modified elastic Rayleigh integral reads

$$\begin{aligned}\Phi^-(\mathbf{r}_A, \omega) \approx & 2 \iint_{S_0} \frac{1}{\rho_0 \omega^2} \left[\left(\partial_z \Gamma_{\phi, \phi}^- \right)^* \Phi^- + \left(\partial_z \Gamma_{\psi, \phi}^- \right)^* \Psi^- \right] dx dy \\ & - 2 \iint_{S_I} \frac{1}{\rho_I \omega^2} \left[\left(\partial_z \Gamma_{\phi, \phi}^+ \right)^* \Phi^+ + \left(\partial_z \Gamma_{\psi, \phi}^+ \right)^* \Psi^+ \right] dx dy, \quad (\text{A.1})\end{aligned}$$

(which follows immediately from (3.123) and (3.124)) where in (A.1) both surface integrals (i.e. over S_0 and S_I) are included (see Fig. A.1).

Again, without any loss of generality, we choose for the spectrum of the wave field in A a flat spectrum (i.e. $\tilde{\Phi}^-(k_x, k_y, z_A; \omega) = 1$). In order to keep the calculations orderly this analysis will be carried out for the 2D situation (in this way we may take into account only one of the three components of the vectorial wave fields). With this choice and after rewriting (A.1) it follows that

$$\begin{aligned}I = & \frac{2}{\rho_0 \omega^2} \left[ik_{z_{p,0}} \left(\tilde{r}_{\phi, \phi}^- \right)^* \tilde{\Phi}_0^- + ik_{z_{s,0}} \left(\tilde{r}_{\psi, \phi}^- \right)^* \tilde{\Psi}_{y,0}^- \right]_{z_0} \\ & - \frac{2}{\rho_I \omega^2} \left[ik_{z_{p,I}} \left(\tilde{r}_{\phi, \phi}^+ \right)^* \tilde{\Phi}_I^+ + ik_{z_{s,I}} \left(\tilde{r}_{\psi, \phi}^+ \right)^* \tilde{\Psi}_{y,I}^+ \right]_{z_I}. \quad (\text{A.2})\end{aligned}$$

At surface S_0 we may write for the upgoing P wave field potential

$$\tilde{\Phi}_0^- = e^{-ik_{z_{p,0}}|z_0 - z_i|} \tilde{T}_{pp}^- e^{-ik_{z_{p,I}}|z_i - z_A|} \quad (\text{A.3})$$

and for the upgoing S_y potential

$$\tilde{\Psi}_{y,0}^- = e^{-ik_{z_{s,0}}|z_0 - z_i|} \tilde{T}_{sp}^- e^{-ik_{z_{p,I}}|z_i - z_A|} \quad (\text{A.4})$$

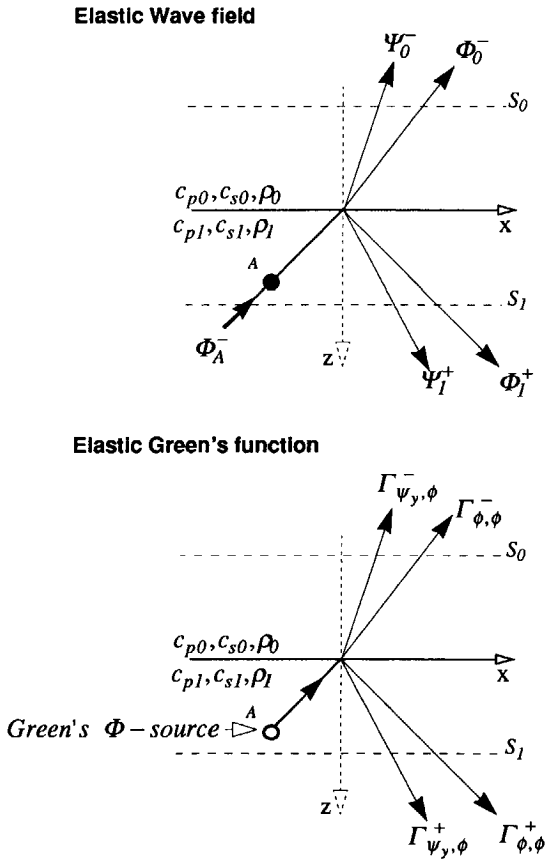
Similarly, at surface S_I we may write for the downgoing P potential

$$\tilde{\Phi}_I^- = e^{-ik_{zp,I}|z_I - z_i|} \tilde{R}_{pp}^- e^{-ik_{zp,I}|z_i - z_A|} \quad (\text{A.5})$$

and for the downgoing S_y potential

Fig. A.1

The elastic wave field and Green's function due to an upgoing P wave through A.



$$\tilde{\Psi}_{y,l}^- = e^{-ik_{zs,l}|z_l-z_i|} \tilde{R}_{sp}^- e^{-ik_{zp,l}|z_i-z_A|}. \quad (\text{A.6})$$

For the Green's P potential at S_0 we may write

$$\tilde{\Gamma}_{\phi,\phi}^- = \rho_l \omega^2 \frac{e^{-ik_{zp,0}|z_0-z_i|} \tilde{T}_{pp}^- e^{-ik_{zp,l}|z_i-z_A|}}{2ik_{zp,l}} \quad (\text{A.7})$$

and for the Green's S_y potential

$$\tilde{\Gamma}_{\psi,\phi}^- = \rho_l \omega^2 \frac{e^{-ik_{zs,0}|z_0-z_i|} \tilde{T}_{sp}^- e^{-ik_{zp,l}|z_i-z_A|}}{2ik_{zp,l}}. \quad (\text{A.8})$$

Similarly, at surface S_l we may write for the downgoing Green's P potential

$$\tilde{\Gamma}_{\phi,\phi}^+ = \rho_l \omega^2 \frac{e^{-ik_{zp,l}|z_l-z_i|} \tilde{R}_{pp}^- e^{-ik_{zp,l}|z_i-z_A|}}{2ik_{zp,l}} \quad (\text{A.9})$$

and for the Green's S_y potential

$$\tilde{\Gamma}_{\psi,\phi}^+ = \rho_l \omega^2 \frac{e^{-ik_{zs,l}|z_l-z_i|} \tilde{R}_{sp}^- e^{-ik_{zp,l}|z_i-z_A|}}{2ik_{zp,l}}. \quad (\text{A.10})$$

For this situation equation (A.2) transforms to

$$I = \frac{\rho_l}{\rho_0} \left[\frac{k_{z_{p,0}}}{k_{z_{p,l}}} \tilde{T}_{pp}^- \tilde{T}_{pp}^- + \frac{k_{z_{s,0}}}{k_{z_{p,l}}} \tilde{T}_{sp}^- \tilde{T}_{sp}^- \right]_{z_0} - \left[\tilde{R}_{pp}^- \tilde{R}_{pp}^- + \frac{k_{z_{s,l}}}{k_{z_{p,l}}} \tilde{R}_{sp}^- \tilde{R}_{sp}^- \right]_{z_l}. \quad (\text{A.11})$$

On the other hand, similarly as in the acoustic situation we may use reciprocal Green's functions (see Fig. A.2). The reciprocal Green's function of (A.7) reads

$$\tilde{\Gamma}_{\phi,\phi}^+ = \rho_0 \omega^2 \frac{e^{-ik_{z_{p,l}}|z_A - z_i|} \tilde{T}_{pp}^+ e^{-ik_{z_{p,0}}|z_i - z_0|}}{2ik_{z_{p,0}}} \quad (\text{A.12})$$

while the reciprocal Green's function for the Green's S_y potential in (A.8) reads

$$\tilde{\Gamma}_{\phi,\psi_y}^+ = \rho_0 \omega^2 \frac{e^{-ik_{z_{p,0}}|z_A - z_i|} \tilde{T}_{ps}^+ e^{-ik_{z_{s,l}}|z_i - z_0|}}{2ik_{z_{s,0}}} \quad (\text{A.13})$$

Similarly, at surface S_l we may write for the reciprocal Green's S_y potential expressed in (A.10)

$$\tilde{\Gamma}_{\phi,\psi_y}^+ = \rho_l \omega^2 \frac{e^{-ik_{z_{p,l}}|z_A - z_i|} \tilde{R}_{ps}^- e^{-ik_{z_{s,l}}|z_i - z_l|}}{2ik_{z_{s,l}}}. \quad (\text{A.14})$$

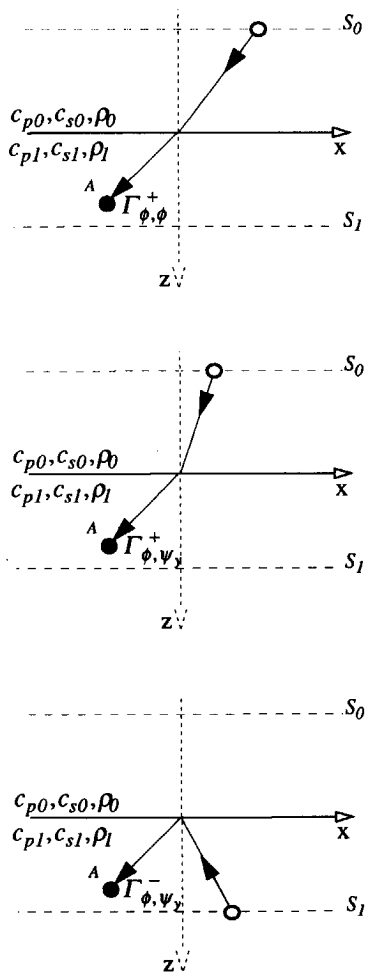
Notice that there is no need to specify a reciprocal Green's function for (A.9) because these are exactly the same. Using these reciprocal Green's functions it can be verified that after substitution into equation (A.2) this equation now becomes

$$I = \tilde{T}_{pp}^+ \tilde{T}_{pp}^- + \tilde{T}_{ps}^+ \tilde{T}_{sp}^- + \tilde{R}_{pp}^- \tilde{R}_{pp}^- + \tilde{R}_{ps}^+ \tilde{R}_{sp}^-. \quad (\text{A.15})$$

Fig. A.2

Reciprocal elastic Green's functions that correspond to the Green's function's in (A.7), (A.8) and (A.10) respectively.

Reciprocal Elastic Green's functions



The four products that appear in this equation correspond with the four products in integral relation (A.1). Thus, (A.15) enables us to analyze the contribution of each of the four products in elastic Rayleigh integral (A.1) in a quantitative way. In the forward and inverse operators that are derived in Chapter 3 only the first term is taken into account. The other three terms are of second order as demonstrated in Chapter 4.

For the reconstruction of the upgoing S potential in A the Kirchhoff integral reads

$$\begin{aligned} \Psi_h^-(\mathbf{r}_A, \omega) \approx & 2 \iint_{S_0} \frac{1}{\rho_0 \omega^2} \left[\left(\partial_z \Gamma_{\phi, \psi_h}^- \right)^* \Phi^- + \left(\partial_z \Gamma_{\psi, \psi_h}^- \right)^* \cdot \Psi^- \right] dx dy \\ & - 2 \iint_{S_I} \frac{1}{\rho_I \omega^2} \left[\left(\partial_z \Gamma_{\phi, \psi_h}^+ \right)^* \Phi^+ + \left(\partial_z \Gamma_{\psi, \psi_h}^+ \right)^* \cdot \Psi^+ \right] dx dy. \quad (\text{A.16}) \end{aligned}$$

The derivation of (4.39) from (A.16) goes in a similar way as the previous derivation.

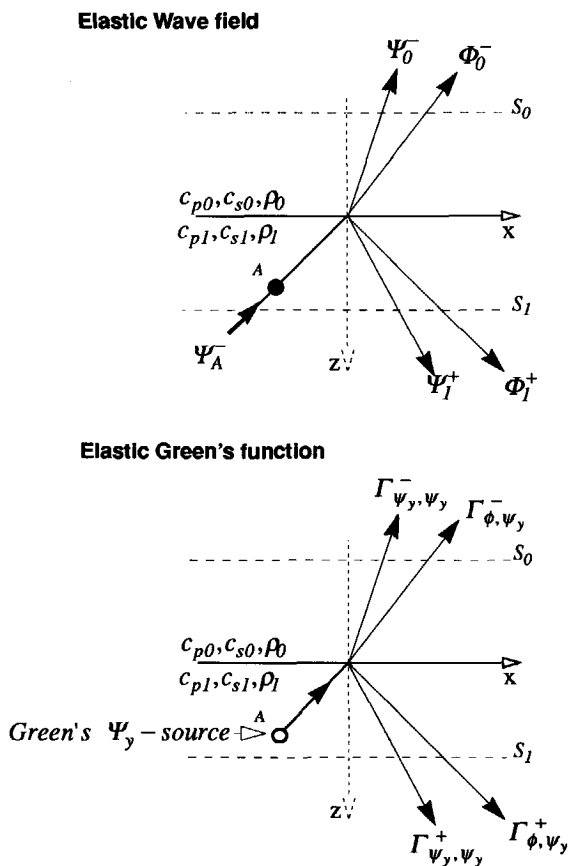
Erroneous macro model

The Green's functions that lead to the result in (A.15) are supposed to be calculated in a correct macro model. In the following we shall examine what happens if the macro model is in error.

Similar as in Chapter 4 we choose for the erroneous macro model the following parameters for the first layer \hat{c}_{p0} , \hat{c}_{s0} and $\hat{\rho}_0$ and for the second layer \hat{c}_{pI} , \hat{c}_{sI} and $\hat{\rho}_I$ (the depth of the reflector is chosen equal to the one in the true model). Using these macro model parameters it can be shown that equation (A.1) transforms to

Fig. A.3

The elastic wave field and Green's function due to an upgoing S wave through A.



$$\begin{aligned}
 I \approx & \frac{2}{\hat{\rho}_0 \omega^2} \left[i \hat{k}_{z_{p,0}} \left(\tilde{\tilde{F}}_{\phi, \phi}^- \right)^* \tilde{\Phi}_0^- + i \hat{k}_{z_{s,0}} \left(\tilde{\tilde{F}}_{\psi_y, \phi}^- \right)^* \tilde{\Psi}_{y,0}^- \right]_{z_0} \\
 & - \frac{2}{\hat{\rho}_1 \omega^2} \left[i \hat{k}_{z_{p,1}} \left(\tilde{\tilde{F}}_{\phi, \phi}^+ \right)^* \tilde{\Phi}_1^+ + i \hat{k}_{z_{s,1}} \left(\tilde{\tilde{F}}_{\psi_y, \phi}^+ \right)^* \tilde{\Psi}_{y,1}^+ \right]_{z_1}, \quad (\text{A.17})
 \end{aligned}$$

where the caret $\hat{}$ relates the underlying quantity to the estimated macro model. Neglecting the integral over S_I yields

$$I \approx \frac{2}{\hat{\rho}_0 \omega^2} \left[\hat{k}_{z_{p,0}} \left(\tilde{\Gamma}_{\phi,\phi}^- \right)^* \tilde{\Phi}_0^- + i \hat{k}_{z_{s,0}} \left(\tilde{\Gamma}_{\psi_y,\phi}^- \right)^* \tilde{\Psi}_{y,0}^- \right]_{z_0} \quad (\text{A.18})$$

At surface S_0 the upgoing P and S_y potentials are still correctly represented by equations (A.3) and (A.4). The reciprocal Green's P potential is now given by

$$\tilde{\Gamma}_{\phi,\phi}^+ = \hat{\rho}_0 \omega^2 \frac{e^{-i \hat{k}_{z_{p,1}} |z_A - z_i|} \tilde{\Gamma}_{pp}^+ e^{-i \hat{k}_{z_{p,0}} |z_i - z_0|}}{2i \hat{k}_{z_{p,0}}} \quad (\text{A.19})$$

and the reciprocal Green's S_y potential by

$$\tilde{\Gamma}_{\phi,\psi_y}^+ = \hat{\rho}_0 \omega^2 \frac{e^{-i \hat{k}_{z_{p,0}} |z_A - z_i|} \tilde{\Gamma}_{ps}^+ e^{-i \hat{k}_{z_{s,1}} |z_i - z_0|}}{2i \hat{k}_{z_{s,0}}}. \quad (\text{A.20})$$

Using these Green's functions it can be shown that (A.18) transforms to

$$\begin{aligned} & \tilde{\Gamma}_{pp}^+ \tilde{\Gamma}_{pp}^- e^{-i(k_{z_{p,0}} - \hat{k}_{z_{p,0}})|z_i - z_0|} e^{-i(k_{z_{p,1}} - \hat{k}_{z_{p,1}})|z_A - z_i|} + \\ & + \tilde{\Gamma}_{ps}^+ \tilde{\Gamma}_{sp}^- e^{-i(k_{zs,0} - \hat{k}_{zs,0})|z_i - z_0|} e^{-i(k_{z_{p,1}} - \hat{k}_{z_{p,1}})|z_A - z_i|} \approx 1, \end{aligned} \quad (\text{A.21})$$

where it can be seen that when an erroneous macro model is used the phase term in (A.21) will generally be non-zero.

Appendix B

Implementation aspects of seismic modeling

B.1 Introduction

The performance of newly developed elastic data processing algorithms can only be adequately determined if those algorithms pass several stages of testing and evaluation. One of these stages is to test the algorithm upon simulated data where all the parameters are known. Testing a new algorithm directly upon field data is from a scientific point of view inadmissible. Over the years a large number of elastic modeling algorithms has been presented in the literature. However, the moment one chooses either one of those algorithms to work with one notices that there are still lots of problems that have yet to be overcome for

which no solution is given. Fixing these “minor” problems is the most time consuming part in the development of a modeling algorithm. In this Appendix, a number of these problems will be addressed together with some solutions.

B.2 Theory

The displacement vector $\mathbf{u}=\mathbf{u}(x,y,z,t)$ satisfies for an isotropic, heterogeneous elastic medium the vector wave equation

$$\begin{aligned} \nabla[(\lambda + 2\mu)\nabla \cdot \mathbf{u}] - \nabla \times (\mu \nabla \times \mathbf{u}) + \\ 2[(\nabla \mu \cdot \nabla)\mathbf{u} - (\nabla \mu)\nabla \cdot \mathbf{u} + (\nabla \mu) \times (\nabla \times \mathbf{u})] - \rho \frac{\partial^2 \mathbf{u}}{\partial t^2} = -\nabla \delta(\mathbf{r} - \mathbf{r}_0)s(t) \end{aligned} \quad (\text{B.1})$$

where $\lambda=\lambda(x,y,z)$ and $\mu=\mu(x,y,z)$ represent the Lamé parameters. The density is denoted by $\rho=\rho(x,y,z)$. On the right hand side a compressional point source is taken into account at position $\mathbf{r}_0=(x_0,y_0,z_0)$. The time variation of the point source is given by $s(t)$. This equation can be written in a somewhat more compact notation as follows

$$\frac{\partial^2 \mathbf{u}}{\partial t^2} = \mathbf{L}\mathbf{u} + \frac{\nabla \delta(\mathbf{r} - \mathbf{r}_0)s(t)}{\rho} \quad (\text{B.2})$$

with operator \mathbf{L} defined by

$$\begin{aligned} \mathbf{L}\mathbf{u} = \rho^{-1} \left[\nabla[(\lambda + 2\mu)\nabla \cdot \mathbf{u}] - \nabla \times (\mu \nabla \times \mathbf{u}) + \right. \\ \left. 2[(\nabla \mu \cdot \nabla)\mathbf{u} - (\nabla \mu)\nabla \cdot \mathbf{u} + (\nabla \mu) \times (\nabla \times \mathbf{u})] \right]. \end{aligned} \quad (\text{B.3})$$

For the 2D situation (the medium and the wave field are assumed to be invariant in the y -direction) the components of displacement vector \mathbf{u} satisfy

$$\frac{\partial^2 u_x}{\partial t^2} = L_x \mathbf{u} + \frac{\partial \delta(\mathbf{r} - \mathbf{r}_0)}{\partial x} \frac{s(t)}{\rho} \quad (\text{B.4})$$

and

$$\frac{\partial^2 u_z}{\partial t^2} = L_z \mathbf{u} + \frac{\partial \delta(\mathbf{r} - \mathbf{r}_0)}{\partial z} \frac{s(t)}{\rho} \quad (\text{B.5})$$

with

$$L_x \mathbf{u} = \rho^{-1} \frac{\partial}{\partial x} \left[\lambda \left(\frac{\partial u_x}{\partial x} + \frac{\partial u_z}{\partial z} \right) + 2\mu \frac{\partial u_x}{\partial x} \right] + \rho^{-1} \frac{\partial}{\partial z} \left[\mu \left(\frac{\partial u_z}{\partial x} + \frac{\partial u_x}{\partial z} \right) \right] \quad (\text{B.6})$$

and

$$L_z \mathbf{u} = \rho^{-1} \frac{\partial}{\partial z} \left[\lambda \left(\frac{\partial u_x}{\partial x} + \frac{\partial u_z}{\partial z} \right) + 2\mu \frac{\partial u_z}{\partial z} \right] + \rho^{-1} \frac{\partial}{\partial x} \left[\mu \left(\frac{\partial u_z}{\partial x} + \frac{\partial u_x}{\partial z} \right) \right]. \quad (\text{B.7})$$

The differential operators that occur in these equations may be approximated by bandlimited versions that are valid within the seismic band (Berkhout, 1987). Let $d_1(\cdot)$ denote a bandlimited version of the first order differential operator and $d_2(\cdot)$ a bandlimited version of the second order differential operator, thus for example

$$\frac{\partial u_z}{\partial z} = d_1(z) * u_z \quad (\text{B.8})$$

and

$$\frac{\partial^2 u_x}{\partial t^2} = d_2(t) * u_x, \quad (\text{B.9})$$

where $*$ denotes convolution. In view of this notation (B.4), (B.5), (B.6) and (B.7) become

$$d_2(t) * u_x = L_x u + \rho^{-1} d_1(x) * \delta(\mathbf{r} - \mathbf{r}_0) s(t) \quad (\text{B.10})$$

and

$$d_2(t) * u_z = L_z u + \rho^{-1} d_1(z) * \delta(\mathbf{r} - \mathbf{r}_0) s(t) \quad (\text{B.11})$$

with

$$\begin{aligned} L_x u = & \rho^{-1} d_1(x) * [\lambda(d_1(x) * u_x + d_1(z) * u_z) + 2\mu d_1(x) * u_x] + \\ & \rho^{-1} d_1(z) * [\mu(d_1(x) * u_z + d_1(z) * u_x)] \end{aligned} \quad (\text{B.12})$$

and

$$\begin{aligned} L_z u = & \rho^{-1} d_1(z) * [\lambda(d_1(x) * u_x + d_1(z) * u_z) + 2\mu d_1(z) * u_z] + \\ & \rho^{-1} d_1(x) * [\mu(d_1(x) * u_z + d_1(z) * u_x)] \end{aligned} \quad (\text{B.13})$$

The length of the differential operators $d_1(\cdot)$ and $d_2(\cdot)$ depends on the desired accuracy. The longer the operator the more accurate the approximation gets. Second order approximations to $d_1(\cdot)$ and $d_2(\cdot)$ can already be found by use of a three points operator (Mitchell, 1969). For the first order derivative this is

$$d_1(.) = \frac{\delta(.+\Delta) - \delta(. - \Delta)}{2\Delta} \quad (\text{B.14})$$

and for the second order derivative

$$d_2(.) = \frac{\delta(.+\Delta) - 2\delta(.) + \delta(. - \Delta)}{2\Delta^2}, \quad (\text{B.15})$$

where Δ represents the discretization interval. Higher order approximations to the first- and second order differentiation operators $d_1(.)$ and $d_2(.)$ can be easily obtained through Taylor expansions (see also Abramowitz and Stegun, 1964; Mufti, 1990). The main advantage of these higher order operators is that the discretization interval Δ may be chosen larger which can be directly translated in an increase of speed or the ability to handle larger models. The price paid for having this advantage however is that the accurate representation of detail in the model has to be sacrificed.

Applying (B.14) and (B.15) to (B.10) and (B.11) yields

$$u_x(x, z, t + \Delta t) = 2u_x(x, z, t) - u_x(x, z, t - \Delta t) + \Delta t^2 \left[L_x u(x, z, t) + \left(\frac{\delta(x - x_0 - \Delta x) - \delta(x - x_0 + \Delta x)}{2\Delta x} \right) \delta(z - z_0) \frac{s(t)}{\rho} \right] \quad (\text{B.16})$$

and

$$u_z(x, z, t + \Delta t) = 2u_z(x, z, t) - u_z(x, z, t - \Delta t) + \Delta t^2 \left[L_z u(x, z, t) + \left(\frac{\delta(z - z_0 - \Delta z) - \delta(z - z_0 + \Delta z)}{2\Delta z} \right) \delta(x - x_0) \frac{s(t)}{\rho} \right] \quad (\text{B.17})$$

and after discretization (writing $u_x(x,z,t)$ as $u_x(m,n,l)$, $u_z(x,z,t)$ as $u_z(m,n,l)$ and $s(t)$ as $s(l)$, where $x=m\Delta x$, $z=n\Delta z$, $t=l\Delta t$ and $h=\Delta x=\Delta z$) the following second order explicit finite-difference scheme (see also Kelly et al., 1976) is obtained

$$u_x(m,n,l+1) = 2u_x(m,n,l) - u_x(m,n,l-1) + \Delta t^2 \left[L_x u(m,n,l) + \left(\frac{\delta_{m_0+1,m} - \delta_{m_0-1,m}}{2h} \right) \delta_{n,n_0} \frac{s(l)}{\rho} \right] \quad (\text{B.18})$$

and

$$u_z(m,n,l+1) = 2u_z(m,n,l) - u_z(m,n,l-1) + \Delta t^2 \left[L_z u(m,n,l) + \left(\frac{\delta_{n,n_0+1} - \delta_{n,n_0-1}}{2h} \right) \delta_{m_0,m} \frac{s(l)}{\rho} \right], \quad (\text{B.19})$$

where δ_{mn} represents the Kronecker delta ($\delta_{ij}=1$ if $i=j$; $\delta_{ij}=0$ if $i \neq j$). These finite-difference equations describe elastic wave propagation in a 2D heterogeneous medium. The medium parameters (λ , μ and ρ) are defined on a 2D grid. In order to avoid divergence of the errors (made in approximating the derivatives) during calculation, the finite-difference algorithm has to satisfy the following stability condition (Alterman and Loewenthal, 1970)

$$\Delta t \leq \frac{h}{\sqrt{c_p^2 + c_s^2}}, \quad (\text{B.20})$$

where c_p and c_s represent the compressional and shear wave velocities respectively and are related to the Lamé parameters through

$$c_p = \sqrt{\frac{\lambda + 2\mu}{\rho}} \quad (\text{B.21})$$

and

$$c_s = \sqrt{\frac{\mu}{\rho}}. \quad (\text{B.22})$$

Grid dispersion is another aspect of modeling that should be given serious consideration. As the waves travel through the grid these waves become progressively dispersed. The degree of dispersion depends largely on the coarseness of the grid. Alford et al. (1974) concluded that in order to keep grid dispersion below an acceptable level the grid interval h should be chosen at least ten times as low as the wavelength at the upper half-power frequency of the source $s(t)$. In formula from this reads

$$h \approx \frac{\lambda_{min}}{10} = \frac{c_{min}}{10f_h}, \quad (\text{B.23})$$

where λ_{min} is the shortest wavelength, c_{min} is the lowest velocity present in the model and f_h denotes the upper half-power frequency in the source function. It is our experience, however, that at least *twenty* grid points per wavelength are necessary for proper *amplitude* processing.

In (B.16) and (B.17) use is made of the differential operator given by (B.15) to approximate the second order time differentiation. In this way at least two time slices should be kept in memory. Applying a higher order approximation, for instance a five points operator, means that now at least four time slices should be stored. There is an other way to approximate the second order time derivative without the need for extra memory. Consider therefore equation (B.2) again

$$\frac{\partial^2 \mathbf{u}}{\partial t^2} = \mathbf{L}\mathbf{u} + \mathbf{S}, \quad (\text{B.24})$$

where a more general source vector function \mathbf{S} is used, scaled by the density.-
Writing $\mathbf{u}(t+\Delta t)$ as a Taylor expansion yields

$$\mathbf{u}(t + \Delta t) = \mathbf{u}(t) + \frac{\Delta t}{1!} \frac{\partial \mathbf{u}}{\partial t} + \frac{\Delta t^2}{2!} \frac{\partial^2 \mathbf{u}}{\partial t^2} + \frac{\Delta t^3}{3!} \frac{\partial^3 \mathbf{u}}{\partial t^3} + \frac{\Delta t^4}{4!} \frac{\partial^4 \mathbf{u}}{\partial t^4} + \dots \quad (\text{B.25})$$

and similarly writing $\mathbf{u}(t-\Delta t)$ as a Taylor expansion yields

$$\mathbf{u}(t - \Delta t) = \mathbf{u}(t) - \frac{\Delta t}{1!} \frac{\partial \mathbf{u}}{\partial t} + \frac{\Delta t^2}{2!} \frac{\partial^2 \mathbf{u}}{\partial t^2} - \frac{\Delta t^3}{3!} \frac{\partial^3 \mathbf{u}}{\partial t^3} + \frac{\Delta t^4}{4!} \frac{\partial^4 \mathbf{u}}{\partial t^4} - \dots \quad (\text{B.26})$$

Addition of these two series gives

$$\mathbf{u}(t + \Delta t) + \mathbf{u}(t - \Delta t) = 2\mathbf{u}(t) + \Delta t^2 \frac{\partial^2 \mathbf{u}}{\partial t^2} + \frac{\Delta t^4}{12} \frac{\partial^4 \mathbf{u}}{\partial t^4} + O(\Delta t^6) \quad (\text{B.27})$$

or

$$\frac{\partial^2 \mathbf{u}}{\partial t^2} = \frac{\mathbf{u}(t + \Delta t) - 2\mathbf{u}(t) + \mathbf{u}(t - \Delta t)}{\Delta t^2} - \frac{\Delta t^2}{12} \frac{\partial^4 \mathbf{u}}{\partial t^4} + O(\Delta t^4). \quad (\text{B.28})$$

Notice that the first term on the right hand side corresponds to the second order approximation given in (B.15). A fourth order approximation without effecting the memory usage can now be found in the following way. Taking the second order time derivative of (B.24) gives

$$\frac{\partial^4 \mathbf{u}}{\partial t^4} = \frac{\partial^2}{\partial t^2} (\mathbf{L}\mathbf{u} + \mathbf{S}) = \mathbf{L} \frac{\partial^2 \mathbf{u}}{\partial t^2} + \frac{\partial^2 \mathbf{S}}{\partial t^2}. \quad (\text{B.29})$$

Substitution of (B.24) in the right hand side of (B.29) yields

$$\frac{\partial^4 \mathbf{u}}{\partial t^4} = \mathbf{L}(\mathbf{L}\mathbf{u} + \mathbf{S}) + \frac{\partial^2 \mathbf{S}}{\partial t^2}. \quad (\text{B.30})$$

Substitution of this result in (B.28) yields a fourth order approximation to the second order time derivative that reads

$$\frac{\partial^2 \mathbf{u}}{\partial t^2} = \frac{\mathbf{u}(t + \Delta t) - 2\mathbf{u}(t) + \mathbf{u}(t - \Delta t)}{\Delta t^2} - \frac{\Delta t^2}{12} \left(\mathbf{L}(\mathbf{L}\mathbf{u} + \mathbf{S}) + \frac{\partial^2 \mathbf{S}}{\partial t^2} \right) + O(\Delta t^4). \quad (\text{B.31})$$

Finally, using this result then (B.24) becomes a fourth order FD scheme in time

$$\mathbf{u}(t + \Delta t) = 2\mathbf{u}(t) - \mathbf{u}(t - \Delta t) + \Delta t^2 \mathbf{L}\mathbf{u} + \frac{\Delta t^4}{12} \left(\mathbf{L}(\mathbf{L}\mathbf{u} + \mathbf{S}) + \frac{\partial^2 \mathbf{S}}{\partial t^2} \right). \quad (\text{B.32})$$

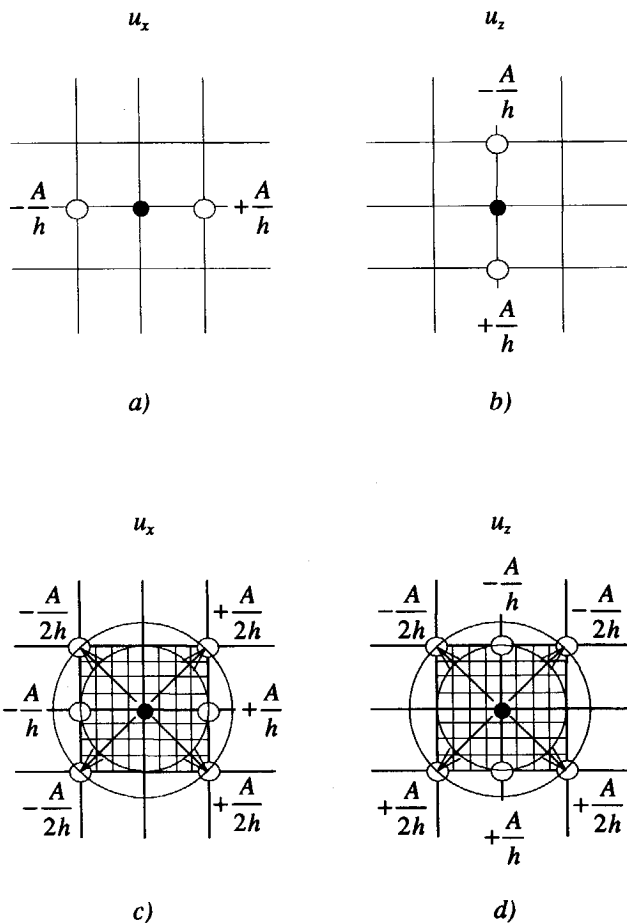
So instead of having to keep two extra time slices of the entire wave field in memory now an extra term has to be calculated given by the last term on the right hand side of (B.32).

B.3 P and SV buried sources

Differentiation of the source term the way it appears in (B.18) and (B.19) causes problems because the amplitudes are too high for such a small operator and higher order terms may no longer be neglected. Often, to overcome this problem, the source components are calculated analytically and then imposed on the numerical grid on the edge of a small rectangular area enclosing the source. To avoid source components to travel inwards the source contribution is then deleted inside the square at every time step. This method is due to Alterman and Karal (1968) and later on used by several other authors. Although this

Fig. B.1

a) and b): P wave source implementation stencils the way they appear in (B.18) and (B.19) for the x-component and z-component respectively. The black dot marks the source position. c) and d): Corner points are used as well in order to compensate for the energy loss over the diagonal paths.



way to implement the source may seem to work satisfactorily it is certainly not the easiest and most elegant way of source implementation. I shall now present an alternative way to implement sources (P and SV) which is much easier and more direct. First the P wave line source. From the source term on the right hand side of (B.18) and (B.19) it can be seen that for each component (u_x or u_z) there are only two points to be used (see Fig. B.1 *a* and *b*). The weight of these components is defined by the source amplitude, which I shall denote by A , divided by the traveled distance h (for brevity I shall for the moment omit the division by $2\Delta x$ as it appears in (B.14)). Because of the very high amplitudes in the vicinity of the source location one would desire a much finer mesh in the source area to get a better distribution of energy over there (Fig. B.1 *c* and *d*). If a finer mesh was used then the source energy would travel along the diagonal paths as well instead of only the horizontal path and vertical path as Fig. B.1 *a* and *b* suggest. Hence, in the scheme of Fig. B.1 *a* and *b* there is energy missing on the diagonal elements. This energy loss however can fully be accounted for by adding an additional term on the corner points. The weight of such a corner term is determined by two factors. The first one is the loss of amplitude due to geometrical spreading (i.e. $A/(h\sqrt{2})$) and the second one from the cosine directivity of the displacements, i.e. $\cos(45^\circ) = \sqrt{2}/2$. Together this makes $(A/(h\sqrt{2}) \times \sqrt{2}/2 =) A/2h$ (see Fig. B.1 *c* and *d*).

A comparison can be made between the analytical solution and the FD solution for a homogeneous medium. To verify the validity of the source implementation described above the following experiment is performed. Consider the model displayed in Fig. B.2. A receiver is placed 300 m vertically (0°) under the source and another one is placed on the diagonal (45°) at a distance of about 424 m (see Fig. B.2). A 60 Hz Gaussian wavelet is used described by $s(t)$. The spatial grid interval is 2 m. The size of the grid is 400x400 points. The results of this experiment can be observed in Fig. B.3. From Fig. B.3 *a* and *b* it can be seen that there is no problem whatsoever concerning the amplitudes in the source area and the source behaves as a perfect P wave line source. Fig. B.3 *c* and *d* show that there is an almost perfect match between the FD solution and the analytical solution using this way of source implementation.

For an SV wave line source the source term on the right hand side of wave equation (B.1) should read

$$\nabla \times \begin{pmatrix} 0 \\ \delta(\mathbf{r} - \mathbf{r}_0) \\ 0 \end{pmatrix} s(t). \quad (\text{B.33})$$

With this term on the right hand side of (B.1), then with (B.14) and (B.15) for the 2D situation (B.18) and (B.19) now become

Fig. B.2

Homogeneous model. Source is positioned at (0,0) and two receivers are positioned at (0,300) and (300,300) respectively.

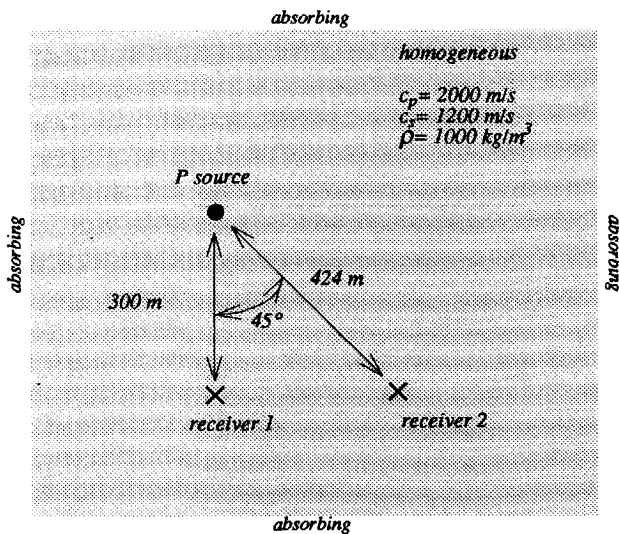
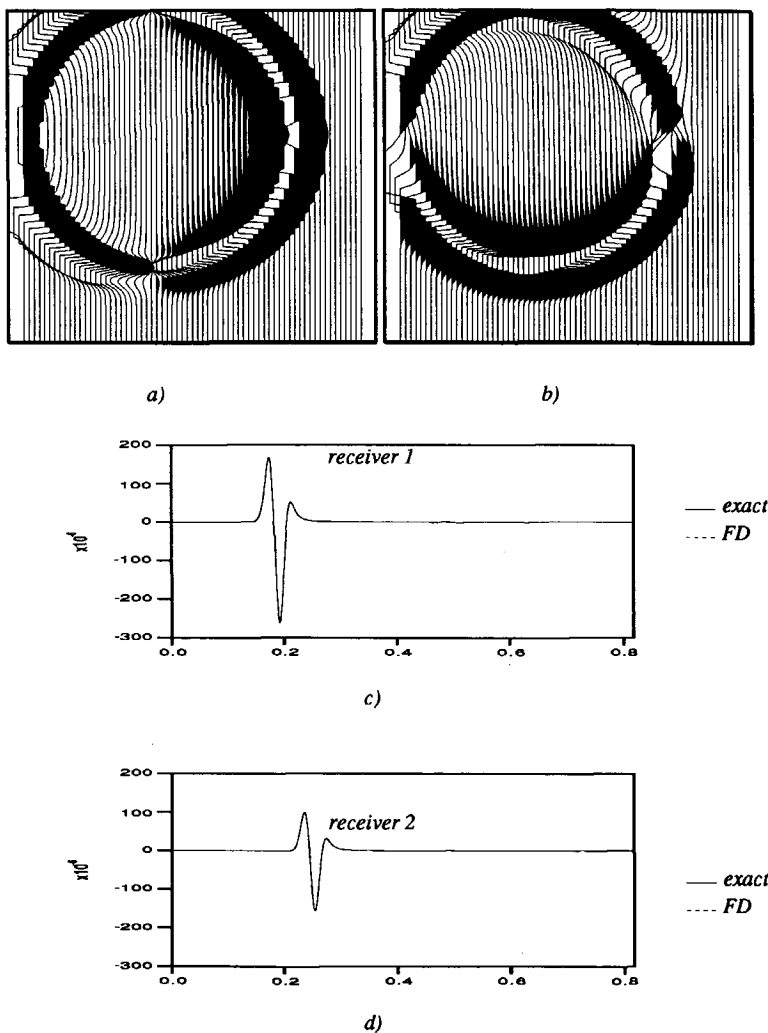


Fig. B.3 a) and b): Snapshots of the horizontal and vertical displacement at time 200 ms using a P wave line source (20 dB clipped). c) and d): Comparison between the FD solution and analytical solution for the two receiver positions.



$$u_x(m, n, l+1) = 2u_x(m, n, l) - u_x(m, n, l-1) + \Delta t^2 \left[\mathbf{L}_x \mathbf{u}(m, n, l) + \left(\frac{\delta_{n, n_0+1} - \delta_{n, n_0-1}}{2h} \right) \delta_{m_0, m} \frac{s(l)}{\rho} \right] \quad (\text{B.34})$$

and

$$u_z(m, n, l+1) = 2u_z(m, n, l) - u_z(m, n, l-1) + \Delta t^2 \left[\mathbf{L}_z \mathbf{u}(m, n, l) - \left(\frac{\delta_{m_0+1, m} - \delta_{m_0-1, m}}{2h} \right) \delta_{n, n_0} \frac{s(l)}{\rho} \right]. \quad (\text{B.35})$$

The source implementation stencils for the *SV* wave source are shown in Fig. B.4. Just like in the *P* source situation the *SV* source implementation is tested against the model and configuration displayed in Fig. B.2. Results are presented in Fig. B.5. A slight mismatch can be noticed that is due to the fact that in order to satisfy the dispersion relation the lowest velocity should be involved and most often this will be the shear wave velocity. Thus, in this example, for the shear waves 10 gridpoints per wavelength are chosen but as the compressional wave velocity is larger then the shear wave velocity this number is often higher (≈ 15 -30) for compressional waves.

The problem of high amplitudes in the source area can be solved by simply taking into account values at the corner points (Fig. B.1 *c* and *d* and Fig. B.4 *c* and *d*). The weight of these values is half of the ones that are used in the horizontal or vertical direction. Source implementation in this way is easy and direct. Early reflections will travel through the source in a natural way without interfering with the direct source wave. Sources can be placed *anywhere* in the heterogeneous medium, close to inhomogeneities or even right across inhomogeneities.

Fig. B.4

a) and b) SV wave source implementation stencils the way they appear in (B.34) and (B.35) for the x-component and z-component respectively. The black dot marks the source position.

c) and d) corner points are used as well in order to compensate for the energy loss over the diagonal paths.

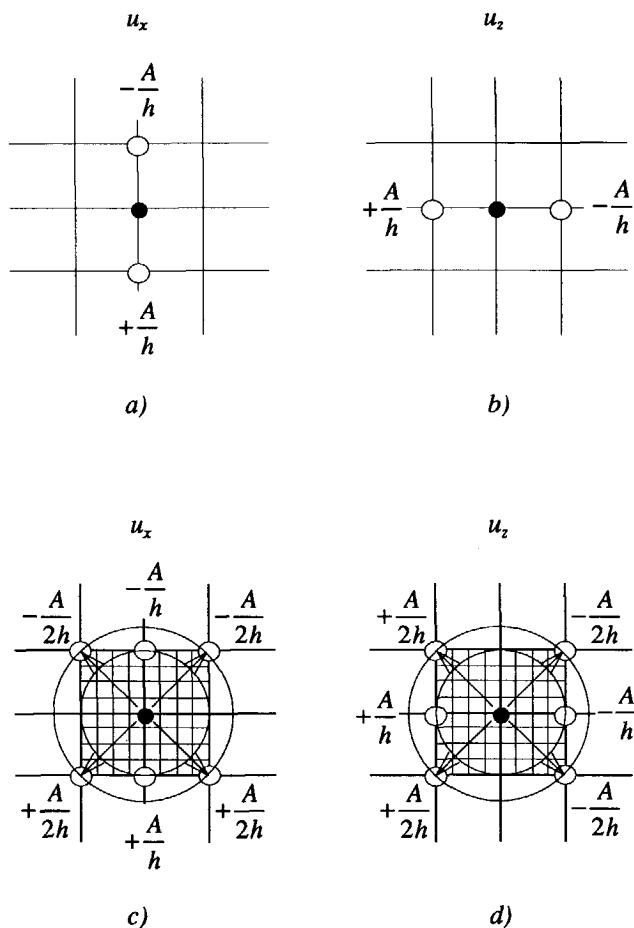
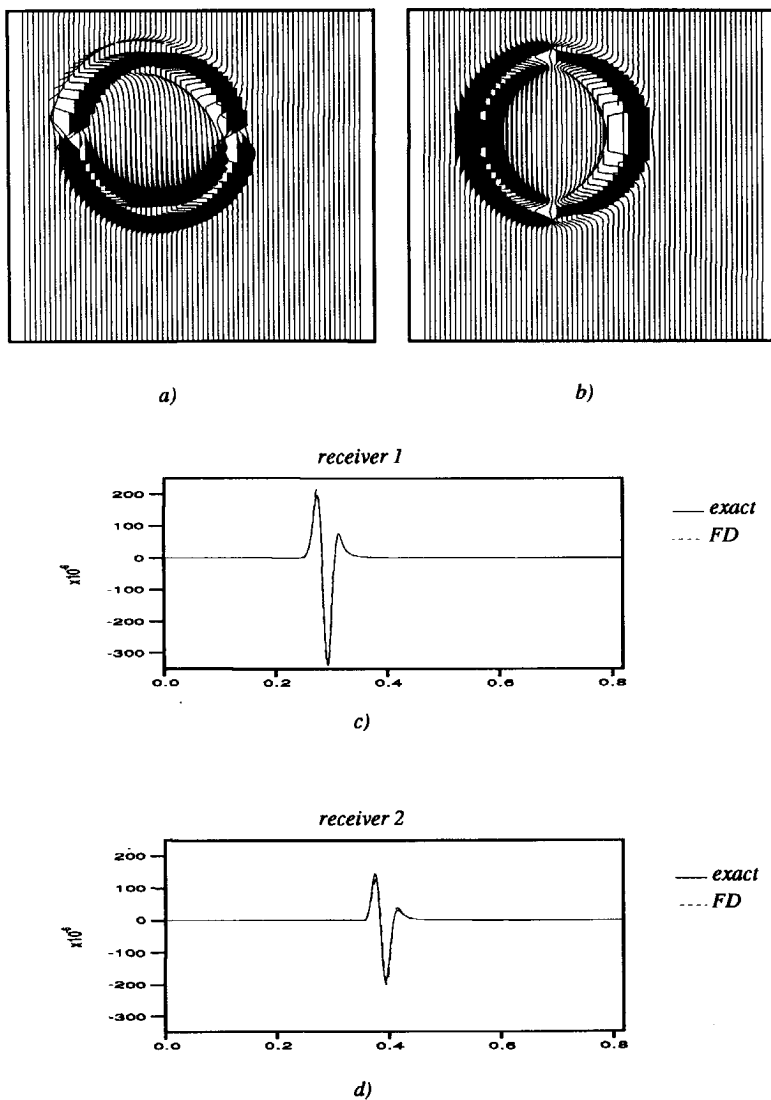


Fig. B.5

*a) and b): Snapshots of the horizontal and vertical displacement at time 200 ms using a SV wave line source (20 dB clipped).
c) and d): Comparison between the FD solution and analytical solution for the two receiver positions.*



B.4 Stress-sources at a free surface

At a (horizontal) free surface stresses have to vanish. For the 2D situation this implies

$$\tau_{xz} = \tau_{zz} = 0 \quad (\text{B.36})$$

(which obviously does not apply to sources located at the free surface). According to the stress-displacement relationship this means that

$$\tau_{zz} = (\lambda + 2\mu) \frac{\partial u_z}{\partial z} + \lambda \frac{\partial u_x}{\partial x} = 0 \quad (\text{B.37})$$

and

$$\tau_{xz} = \mu \left(\frac{\partial u_x}{\partial z} + \frac{\partial u_z}{\partial x} \right) = 0. \quad (\text{B.38})$$

Applying the first order differential operator (B.14) to these two conditions yields (Kelly et al., 1976)

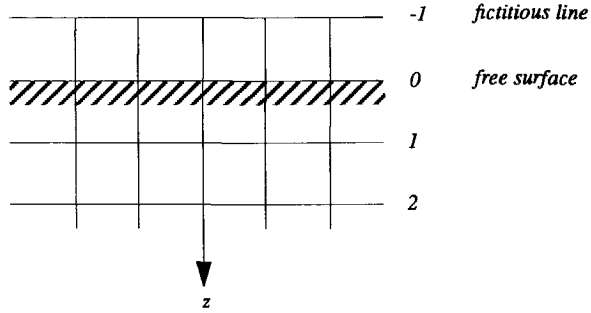
$$(\lambda + 2\mu)(u_z(m, 1, l) - u_z(m, -1, l)) + \lambda(u_x(m + 1, 0, l) - u_x(m - 1, 0, l)) = 0 \quad (\text{B.39})$$

and

$$u_x(m, 1, l) - u_x(m, -1, l) + u_z(m + 1, 0, l) - u_z(m - 1, 0, l) = 0. \quad (\text{B.40})$$

Fig. B.6

A fictitious line is introduced in order to satisfy the free surface conditions at $z=0$. The displacements at this line are calculated using (B.39) and (B.40).



With these equations the values for the horizontal and vertical displacement at a fictitious line at ($z=-\Delta z$ or $m=-1$) are calculated to guarantee the free surface condition (Fig. B.6). Unlike the scheme given in Kelly et al. it can be noticed in (B.39) and (B.40) that I prefer to apply a centered difference in the z -direction which is centered at the $z=0$ line. In this way the free surface is located exactly at $z=0$ while in the scheme from Kelly's paper the free surface is actually between $z=-\Delta z$ (fictitious line) and $z=0$.

Applying a τ_{zz} -source at a free surface with source variation $s(l)$ means that at a certain lateral position $(x_0, 0) \hat{=} (m_0 \Delta x, 0)$ the following may be written

$$(\lambda + 2\mu)(u_z(m_0, 1, l) - u_z(m_0, -1, l)) + \lambda(u_x(m_0 + 1, 0, l) - u_x(m_0 - 1, 0, l)) = s(t) \quad (\text{B.41})$$

and with (B.40) still holding at the source position. Similarly for a τ_{xx} -source at a free surface with source variation $s(t)$ the following can be written

$$u_x(m_0, 1, l) - u_x(m_0, -1, l) + u_z(m_0 + 1, 0, l) - u_z(m_0 - 1, 0, l) = s(t) \quad (\text{B.42})$$

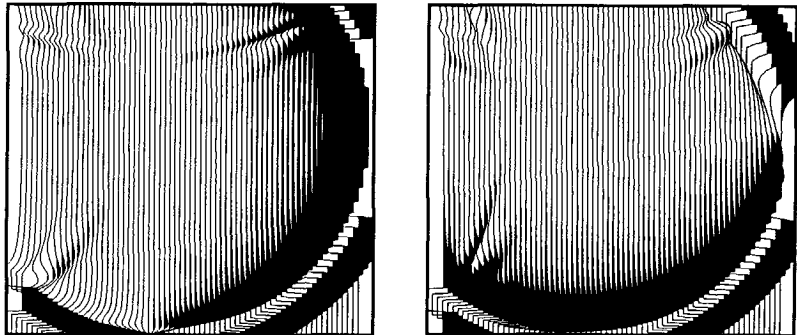
and now (B.39) still holds at the source position.

B.5 Absorbing boundaries; Clayton and Engquist (1977)

At the edges of the grid absorbing boundaries are applied given by Clayton and Engquist (1977). These conditions are based on the paraxial approximation of the elastic wave equation. This approximation has the property that the absorbing boundary works well for small angles of incidence but rapidly deteriorates for higher angles with almost total reflection for very high angles. Fig. B.7

Fig. B.7

a) and b) Snapshots for the horizontal and vertical displacement from the same experiment depicted in Fig. B.2 at time 300 ms (25 dB clipped). At the edges boundary conditions are applied that are due to Clayton and Engquist (1977).



a)

b)

shows the same snapshot displayed in Fig. B.3 but now 25 dB clipped. It may be concluded that these conditions fail for high angles looking at the reflection data because the reflected amplitudes from the absorbing boundary easily exceed that of events reflected at an interface. Later on in section B.7 a comparison is made with absorbing boundary conditions formulated by Lindman (1975) for the scalar wave equation and later on extended to the elastic case by Randall (1988, 1989).

B.6 Staggered grid

Instead of starting of with the second order differential wave equation (B.1) it is also possible to start with the first order elastodynamic equations given by

$$\rho \frac{\partial v_x}{\partial t} = \frac{\partial \tau_{xx}}{\partial x} + \frac{\partial \tau_{xz}}{\partial z}, \quad (\text{B.43})$$

$$\rho \frac{\partial v_z}{\partial t} = \frac{\partial \tau_{xz}}{\partial x} + \frac{\partial \tau_{zz}}{\partial z}, \quad (\text{B.44})$$

$$\frac{\partial \tau_{xx}}{\partial t} = (\lambda + 2\mu) \frac{\partial v_x}{\partial x} + \lambda \frac{\partial v_z}{\partial z}, \quad (\text{B.45})$$

$$\frac{\partial \tau_{zz}}{\partial t} = (\lambda + 2\mu) \frac{\partial v_z}{\partial z} + \lambda \frac{\partial v_x}{\partial x} \quad (\text{B.46})$$

and

$$\frac{\partial \tau_{xz}}{\partial t} = \mu \left(\frac{\partial v_x}{\partial z} + \frac{\partial v_z}{\partial x} \right) \quad (\text{B.47})$$

where v_x and v_z represent the horizontal and vertical component respectively of the particle velocity vector \mathbf{v} . Using the differential notation from equation (B.8) this system transforms to

$$d_1(t) * v_x = \rho^{-1} (d_1(x) * \tau_{xx} + d_1(z) * \tau_{xz}), \quad (\text{B.48})$$

$$d_1(t) * v_z = \rho^{-1} (d_1(x) * \tau_{xz} + d_1(z) * \tau_{zz}), \quad (\text{B.49})$$

$$d_1(t) * \tau_{xx} = (\lambda + 2\mu)d_1(x) * v_x + \lambda d_1(z) * v_z, \quad (\text{B.50})$$

$$d_1(t) * \tau_{zz} = (\lambda + 2\mu)d_1(x) * v_z + \lambda d_1(z) * v_x \quad (\text{B.51})$$

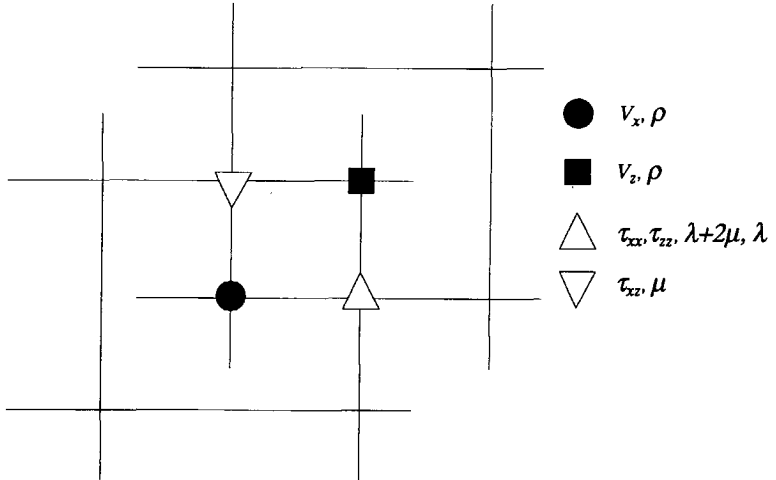
and

$$d_1(t) * \tau_{xz} = \mu(d_1(z) * v_x + d_1(x) * v_z). \quad (\text{B.52})$$

Discretization of the above system leads to a staggered grid as can be seen in Fig. B.8 (Virieux, 1984). The differential operator $d_1(\cdot)$ may be approximated by a second order centered difference given by

Fig. B.8

Calculation stencil for a staggered grid. Black symbols and white symbols are staggered $1/2 \Delta t$ in time.



$$d_1(.) = \frac{\delta(.+1/2\Delta) - \delta(. - 1/2\Delta)}{\Delta} \quad (\text{B.53})$$

A fourth order approximation of the differential operator $d_1(.)$ is given by Levander, 1988. Unlike the non-staggered method discussed previously the velocity components v_x and v_z do not coincide. The grid is staggered in place but also in time, hence, the stress fields and the velocity fields are never known at the same time. The implementation of a P wave line source is extremely easy and is done just by adding an equal portion of the source variation to τ_{xx} and τ_{zz} which are defined at the same nodal point (Gauthier, 1983). The implementation of an SV wave line source can be done by adding the source term to one point on τ_{xz} . One has to be careful though, because this term should be positive to calculate the horizontal velocity (B.48) and negative for the vertical velocity (B.49) and removed when calculating the τ_{xx} stress field (B.52) itself for each timestep. Stress-sources are also simple because the stress fields are now directly accessible. The stability criterion for a second order staggered grid scheme is somewhat more stringent and is given by

$$\Delta t \leq \frac{h}{c_p \sqrt{2}} \quad (\text{B.54})$$

The grid-dispersion relation is the same as the one valid for the non-staggered grid scheme.

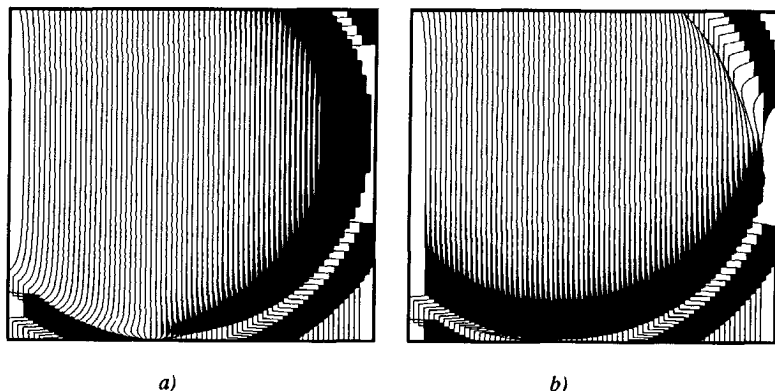
B.7 Absorbing boundary conditions; Randall (1988,1989)

Randall (1988, 1989) extended the highly absorbing boundary conditions presented by Lindman in 1975 for the acoustic wave equation to the elastic wave equation, for both the non-staggered grid scheme as well as for the staggered grid scheme (Randall, 1988 and Randall, 1989 respectively). I have implemented these conditions for a second order staggered grid scheme as the one described above. Using the same homogeneous model as depicted in Fig. B.2,

with the same P wave line source on the same location, it can be seen from Fig. B.9 that these conditions are far superior to the one given by Clayton and Engquist (1976), especially for high angles (compare Fig. B.7).

There is one disadvantage however and that is the fact that these conditions only work well if the boundary is completely homogeneous while in the case of the conditions given by Clayton and Engquist (1976) this restriction is not that severe. The only way to circumvent this problem for the moment is to smooth the velocity and density fields near the edges of the model. Another thing that can be noticed is that from these snapshots one may observe that the conditions applied in the *corners* also absorb the incoming wave energy extremely well. Randall (1989) proposed to use in the corners of the grid the transparent conditions formulated by Liao et al., (1984). Although this is probably one of the possible solutions I followed however a different path that led to the results in Fig. B.9. Because a detailed discussion on this would lead us beyond the scope of this appendix, I shall suffice by presenting the final results of the solution that were found to be effective for the corners. By separating the elastic wave field at the edges of the grid into compressional and shear waves it is possible to apply the highly absorbent boundary conditions from Lindman (1975). In

Fig. B.9 a) and b) Horizontal and vertical displacement. At the edges of the grid absorbing boundaries are applied that are due to Randall (1989). Snapshots are 25 dB clipped (compare Fig. B.7).



these boundary conditions use is made of so called correction functions h_m (one for compressional waves and two for shear waves). The boundary condition (the so called L1 condition, see Lindman (1975) or Randall (1989)) for the compressional wave on the right side of the grid reads

$$\frac{\partial \phi}{\partial t} + c \frac{\partial \phi}{\partial x} = - \sum_{m=1}^M h_m, \quad (\text{B.55})$$

where

$$\frac{\partial^2 h_m}{\partial t^2} - \beta_m c^2 \nabla_{\perp}^2 h_m = \alpha_m c^2 \nabla_{\perp}^2 \left(c \frac{\partial \phi}{\partial x} \right) \quad (\text{B.56})$$

and

$$\nabla_{\perp}^2 = \frac{\partial^2}{\partial y^2} + \frac{\partial^2}{\partial z^2}. \quad (\text{B.57})$$

For the 2D situation (x - z plane) this operator reduces to

$$\nabla_{\perp}^2 = \frac{\partial^2}{\partial z^2}. \quad (\text{B.58})$$

In equations (B.55) and (B.56) ϕ denotes the scalar P potential and c the compressional wave velocity. Coefficients α_m and β_m are obtained by minimizing a weighted average of the reflection coefficients. Lindman already got reflection coefficients less than 0.01 for propagating waves for angles up to 89° with only three terms ($M=3$). The correction function h_m is known everywhere on the edges of the grid except in the corners. A good estimate for these corner values

of the correction functions can readily be found by Taylor expansions. For the correction function on the right boundary $h_m(x_{\max}, z, t)$ this gives

$$h_m(x_{\max}, z + \Delta z, t + \Delta t) = h_m(x_{\max}, z, t) + \frac{\Delta z}{1!} \frac{\partial h_m}{\partial z} + \frac{\Delta t}{1!} \frac{\partial h_m}{\partial t} + 0(\Delta z^2, \Delta t^2) \quad (\text{B.59})$$

or

$$h_m(x_{\max}, z - \Delta z, t - \Delta t) = h_m(x_{\max}, z, t) - \frac{\Delta z}{1!} \frac{\partial h_m}{\partial z} - \frac{\Delta t}{1!} \frac{\partial h_m}{\partial t} + 0(\Delta z^2, \Delta t^2) \quad (\text{B.60})$$

Adding these two series yields a second order approximation for $h(x+\Delta x, t+\Delta t)$

$$h_m(x_{\max}, z + \Delta z, t + \Delta t) = 2h_m(x_{\max}, z, t) - h_m(x_{\max}, z - \Delta z, t - \Delta t) + 0(\Delta z^2, \Delta t^2) \quad (\text{B.61})$$

or after discretization

$$\bar{h}_m(N, M, l + 1) = 2h_m(N, M - 1, l) - h_m(N, M - 2, l - 1), \quad (\text{B.62})$$

where $x_{\max} = N\Delta x$ and $t = l\Delta t$ (see Fig. B.10). The same approximation can be made for the correction functions for the shear wave components.

B.8 Conclusions

Alternative implementations of P and SV buried sources in a second-order coupled displacement scheme (Kelly et al., 1976) are presented. These implementations are equivalent to the one presented by Alterman and Karal (1968) but have the advantage that implementation is very simple and that there is no

Fig. B.10 The corner value \bar{h}_m of the correction function for a staggered grid may be approximated by (B.62).

		ϕ	h_m	ϕ	
		ϕ	h_m	ϕ	$M-2$
		ϕ	h_m	ϕ	$M-1$
		ϕ	\bar{h}_m	ϕ	M

restriction to the complexity of the source area. Stress-sources at a free surface are also described for a second-order coupled displacement scheme and appear to work adequately.

One big disadvantage of the second-order coupled FD scheme is that there are some upper limits with respect to the Poisson's ratio (see Kelly et al., 1976). For the free surface the ratio between the compressional and shear wave velocity should be kept below 0.35. Liquid-solid boundaries are not possible. In a staggered grid scheme (Virieux, 1986) all Poisson's ratios can be modelled. Liquid-solid interfaces are correctly handled, which is important for marine seismic problems. Surface and buried sources are easily implemented. Because both stresses and velocities are directly available in the staggered grid scheme, boundary conditions such as free surface conditions can easily be satisfied. A disadvantage of the staggered grid scheme is that the different components of the wave field are not available on the same nodal point which is often desirable especially when collecting surface data.

A comparison between absorbing boundary conditions presented by Clayton and Engquist (1977) and by Randall (1988,1989) reveals the superior performance of the latter. An alternative solution for the corner points for this condition is presented by equation (B.62) to the one proposed by Randall (1988, 1989).

References

- Aki, K., and Richards, P. G., 1980, Quantitative Seismology, W. H. Freeman and Co.
- Alford, R. M., Kelly, K. R. and Boore, D. M., 1974, Accuracy of finite-difference modeling of the acoustic wave equation: *Geophysics*, v. 39, p. 834-842.
- Alterman, Z. S. and Karal, F. C., Jr., 1968, Propagation of elastic waves in layered media by finite-difference methods: *Bull. Seism. Soc. Am.*, v. 58, p. 367-398.
- Alterman, Z. S. and Loewenthal, D., 1970, Seismic waves in a quarter and three-quarter plane: *Geophys. J. Roy. Astr. Soc.*, 20, 101-126
- Berkhout, A. J., 1982, Seismic migration, Imaging of acoustic energy by wave field extrapolation, Elsevier Science Publ. Co., Inc.
- 1987, Applied seismic wave theory, Elsevier Science Publ. Co., Inc.
 - 1989, Key issues in integrated seismic extrapolation, *First Break*, vol. 7, nr. 8.
- Berkhout, A. J., and Wapenaar, C. P. A., 1990, Delft Philosophy on acoustic and elastic inversion, *Leading Edge*, p. 30-33.

- Beresford-Smith, G. and Rango, R., 1989, Suppression of ground roll by windowing in two domains, *First Break* 7, 55-63.
- Bernth, H., and Sonneland, L., 1983, Wave field extrapolation techniques for prestack attenuation of water reverberations: presented at the 53rd Ann. Internat. Mtg., Soc. Explor. Geophys.
- Berryhill, J.R., and Kim, Y.C., 1986, Deep-water peglegs and multiples: emulation and suppression, *Geophysics*, Volume 51, 2177-2184.
- Bleistein, N., 1984, *Mathematical methods for wave phenomena*: Academic Press, Inc.
- 1987, Kirchhoff inversion for reflector imaging and soundspeed and density variations, in *Deconvolution and Inversion*: Blackwell, 305-320.
- de Bruin, C. G. M., Wapenaar, C. P. A., and Berkhout, A. J., 1990, Angle dependent reflectivity by means of prestack migration: *Geophysics*, 55, 1223-1234.
- de Bruin, C. G. M., 1992, Linear AVO inversion by prestack depth migration. Ph.D. thesis, Delft University of Technology.
- Burridge, R. and Knopoff, L. 1964. Body force equivalents for seismic dislocations: *Bulletin of the Seismological Society of America*, 54, 1875-1888.
- Clayton, R. W. and Engquist, B., 1977, Absorbing boundary conditions for acoustic and elastic wave equations, *Bull. Seism. Soc. Am.*, 67, 1529-1541.
- Cox, H. L. H., 1991, Estimation of macro velocity models by wave field extrapolation, Ph.D. thesis, Delft University of Technology.
- Dankbaar, J.W.M., 1985, Separation of P- and S-waves. *Geophysical Prospecting*, 33, 970-986.
- 1987, Vertical seismic profiling - separation of P- and S-waves, *Geophysical Prospecting* 35, 803-814.
- Devaney, A.J. and Oristaglio, M.L., 1986, A plane wave decomposition for elastic wave-fields applied to the separation of P- and S-waves in a seismic vector. Short note, *Geophysics*, 51, 419-423.
- Dudgeon, D.E. and Mersereau, R.M. 1984. *Multidimensional Digital Signal Processing*. Prentice-Hall, Englewood Cliffs, N.J.
- Gauthier, O., 1983, Inversion de données de sismique réflexion dans l'approximation acoustique: Rapport de stage de D.E.A., Univ. de Paris 7.

-
- de Haas, J. C., 1992, Elastic Stratigraphic inversion, an integrated approach, Ph.D. thesis, Delft University of Technology.
- Herrmann, P., 1992, Decomposition of multi-component measurements into P and S waves. Ph.D. thesis, Delft University of Technology.
- van der Hijden, J.H.M.T., Propagation of transient elastic waves in stratified anisotropic media, Ph.D thesis, Delft University of Technology.
- de Hoop, A.T., 1958, Representation theorems for the displacement in an elastic solid and their application to elastodynamic diffraction theory. D.Sc. thesis, Delft University of Technology.
- 1990, Reciprocity theorems for acoustic wave fields in fluid/solid configurations, J. Acoust. Soc. Am., 87 (5), 1932-1937.
- de Hoop, M.V., 1992, Directional decomposition of transient acoustic wave fields, Ph.d. thesis, Delft University of Technology.
- Kennett, B.L.N., 1979, The suppression of surface multiples on seismic records, Prospecting, Volume 27, 584-600.
- 1983, Seismic wave propagation in stratified media, Cambridge University Press.
- Kelly K. R., Ward, R. W., Treitel, S. and Alford, R. M., 1976, Synthetic seismograms: A finite-difference approach: Geophysics, 41, 2-27.
- Kuo, J.T. and Dai, T.F. 1984, Kirchhoff elastic wave migration for the case of noncoincident source and receiver. Geophysics 49, 1223-1238.
- Levander, A. R., 1988, Fourth-order finite-difference *P-SV* seismograms, Geophysics, v. 53, p. 1425-1436.
- Liao, E. L., Wong, H. L., Yang, B. P. and Yuan, Y. F., 1984, A transmitting boundary for transient wave analysis: Scientia Sinica A, 27, 1063-1076
- Lindman, E. L., 1975, Free space boundaries for the scalar wave equation: J. Comp. Phys., 18, 66-78.
- Lörtzer, G. J., 1990, An integrated approach to lithological inversion, Ph.D. thesis, Delft University of Technology.
- *

References

- McMechan, G.A. and Sun, R., 1991, Depth filtering of first breaks and ground roll, *Geophysics*, 56, 390-396.
- Mitchell, A. R., 1969, *Computational methods in partial differential equations*: New York, John Wiley & Sons.
- Morse, P. F., and Hildebrandt, G. F., 1989, Ground-roll suppression by the stackarray: *Geophysics*, 54, 290-301.
- Mufti, I. R., 1990, Large-scale three-dimensional seismic models and their interpretive significance, *Geophysics*, v. 55, p. 1166-1182.
- Pao, Y.H. and Varatharajulu, V. 1976. Huygen's principle, radiation conditions, and integral formulas for the scattering of elastic waves, *Journal of the Acoustical Society of America* 59, 1361-1371.
- Randall, C. J., 1988, Absorbing boundary condition for the elastic wave equation, *Geophysics*, v. 53, p. 611-624.
- 1989, Absorbing boundary condition for the elastic wave equation: velocity-stress formulation, *Geophysics*, v. 54, p. 1141-1152.
- Saatcilar, R., and Canitez, N., 1988, A method of ground-roll elimination: *Geophysics*, 53, 894-902.
- Tarantola, A., 1987, *Inverse problem theory, methods for data fitting and model parameter estimation*, Elsevier Science Publ. Co., Inc.
- Ursin, B., 1983, Review of elastic and electromagnetic wave propagation in horizontally layered media: *Geophysics*, 48, 1063-1081.
- Verschuur, D. J., 1991, Surface-related multiple elimination, an inversion approach, Ph.D. thesis, Delft University of Technology.
- Virieux, J., 1984, *P-SV wave propagation in heterogeneous media: velocity-stress finite-difference method*: *Geophysics*, 51, 889-901.
- Wapenaar, C. P. A., 1986, Pre-stack migration in two and three dimensions, Ph.D. thesis, Delft University of Technology.
- Wapenaar, C. P. A., and Berkhout, A. J., 1989, *Elastic wave field extrapolation: Redatuming of Single- and Multi-component Seismic data*. Elsevier Science Publ. Co., Inc.

-
- Wapenaar, C. P. A., and Haimé, G.C., 1990, Elastic extrapolation of primary seismic P- and S-waves: *Geophys. Prosp.*, 38, 23-60.
- Wapenaar, C. P. A., Herrmann, P., Verschuur, D. J., and Berkhout, A. J., 1990, Decomposition of multi-component seismic data into primary P and S wave responses: *Geophys. Prosp.*, 38, 633-661.
- Wapenaar, C.P.A., Peels, G.L., Budejicky, V. and Berkhout, A.J., 1989. Inverse extrapolation of primary seismic waves. *Geophysics* 54, 853-863.
- Wapenaar, C.P.A., Verschuur, D. J., and Herrmann, P., 1992. Amplitude pre-processing of single- and multi-component 2D seismic data: *Geophysics*, September issue.

References

Summary

In commercially available seismic processing software wave field extrapolation operators are based on the acoustic assumption. It is well known that these operators can handle the P wave traveltime information properly but the amplitudes are not handled correctly. Currently there is an increasing interest concerning the amplitude contents of seismic reflection data. Seismic amplitudes contain important information on the litho-stratigraphy of hydrocarbon reservoirs. In view of this growing interest, this thesis presents forward and inverse elastic extrapolation operators that properly handle seismic amplitudes.

From the elastic Kirchhoff-Helmholtz integral relation, which is in terms of displacements and stresses, modified Rayleigh-type integrals are derived that express either the P or the S wave field in some subsurface point A in terms of a surface integral that is entirely expressed in terms of P and S potentials. These type of integrals use decomposed elastic P and S Green's functions related to either an impulsive P or an impulsive S source excitation in subsurface point A . From these modified Rayleigh integrals accurate P and S extrapolation opera-

tors can easily be obtained by evaluating the interaction between the decomposed primary P and S wave fields of the data and the Green's functions. For most realistic seismic situations the amplitude error involved can be neglected. The modified Rayleigh integrals are well suited for a quantitative elastic amplitude analysis of extrapolation results. The amplitude behavior is studied for both correct and incorrect macro models. It is found that small errors in the macro model do not affect transmission amplitudes up to high angles of incidence. For larger macro model errors the amplitude error is not negligible but it remains nearly constant for a wide range of angles. Hence, the amplitude versus offset is hardly affected by the extrapolation process except for a constant factor. It is also shown that due to inconsistencies in the P and S macro models the decomposition into P and S waves should preferably be performed before the actual wave field extrapolation takes place.

Finally, the extrapolation operators are tested on a 2D synthetic multi-component data example. After the data have been decomposed into up- and downgoing P and S waves, the extrapolation operators are used to downward extrapolate these P and S data in two separate extrapolation processes. The example clearly shows the benefits; but it also illustrates some of the problems to be expected in practice. One of these problems concerns the effect of the finite aperture, which is inherent to seismic data acquisition. The truncation of the data at the sides causes artifacts in the extrapolated data; they affect the amplitudes within the aperture, especially at the far offsets. However, despite these truncation artifacts the results show that the extrapolation operators handle amplitudes in such a way that for each lateral position in the target area accurate angle dependent reflection curves can be constructed.

Samenvatting

In commercieel beschikbare seismische processing software zijn golfveld extrapolatie operatoren gebaseerd op de akoestische aanname. Het is bekend dat deze operatoren de looptijden van de P golven correct meenemen maar dat de amplitudes incorrect behandeld worden. Momenteel is er een groeiende belangstelling met betrekking tot de amplitudeinhoud van seismische reflectie data. Seismische amplitudes herbergen belangrijke informatie over de lithostratigrafie van een gas en/of olie-reservoir. Met het oog op deze groeiende interesse worden in dit proefschrift voorwaartse en inverse elastische extrapolatie operatoren gepresenteerd die seismische amplitudes correct meenemen. Vanuit de Kirchhoff-Helmholtz integraal relatie, in termen van uitwijkingen en tracties, worden gemodificeerde Rayleigh integralen afgeleid die het P of het S golfveld in een punt A in de ondergrond beschrijven in termen van een oppervlakte integraal die geheel gespecificeerd is in termen van P en S potentialen.

Dit type integralen maakt gebruik van gedecomposeerde elastische P en S Greense funkties die gerelateerd zijn aan een impulsieve P bron of aan een impulsieve S bron in A . Vervolgens worden, uitgaande van deze gemodificeerde Rayleigh integralen, nauwkeurige P en S extrapolatie operatoren verkregen door de interactie tussen de de primaire P en S golven in de data en in de Greense funkties te evalueren. In de meeste realistische seismische situaties mogen amplitude fouten ten gevolge van deze operatoren verwaarloosd worden.

De gemodificeerde Rayleigh integralen zijn uiterst geschikt voor quantitative amplitude analyse van extrapolatie resultaten. Het amplitude gedrag is bekeken voor correcte en voor incorrecte macro modellen. Het blijkt dat transmissie amplitudes tot op grote hoeken niet in belangrijke mate beïnvloed worden door kleine fouten in het macro model. Voor grote fouten is de invloed significant maar deze blijft vrijwel constant voor een groot hoekbereik. Dus het laterale amplitude gedrag wordt nauwelijks beïnvloed door het extrapolatie proces afgezien van een constante factor. Verder wordt aangetoond dat het beter is het elastische golfveld in P en S te decomponeren nog voor het extrapolatie proces plaatsvindt. Dit ten gevolge van inconsistente P en S macro modellen.

Tenslotte zijn de extrapolatie operatoren getest op een 2D gesimuleerde multi-componenten dataset. Nadat de data aan het oppervlak gesplitst zijn in P en S golven worden vervolgens de extrapolatie operatoren gebruikt om deze in P en S gescheiden data neerwaarts te extrapoleren in twee afzonderlijke extrapolatie processen. Het voorbeeld maakt heel duidelijk wat de voordelen zijn, maar illustreert ook de problemen die verwacht kunnen worden in de praktijk. Een van deze problemen betreft het effect van een eindige apertuur, hetgeen inherent is aan seismische data acquisitie. De truncatie van de data aan weerszijden heeft tot gevolg dat er artefacten ontstaan in de geëxtrapolerde data; deze tasten de amplitudes binnen de apertuur aan, met name voor de hogere hoeken. De resultaten laten verder zien dat de extrapolatie operatoren de amplitudes dusdanig goed meenemen dat, ondanks bovengenoemde artefacten, voor elke laterale positie in het reservoir nauwkeurige hoekafhankelijke reflectie curves geconstrueerd kunnen worden.

Curriculum Vitae

Name:	Haimé, Gregory Carlo
Born:	November 21, 1960; Paramaribo, Surinam
Nationality:	Dutch

1978-1980	secondary school (Atheneum)
1980-1988	Delft University of technology (Applied Physics)
1988-1992	employed as research assistant first with the Triton consortium later on with the Delphi consortium
1992-present	currently employed as research geophysicist at GECO-PRAKLA, Delft.

